



**The Production of ^{13}N from Inertial
Electrostatic Confinement Fusion**

John W. Weidner

June 2003

UWFDM-1210

***FUSION TECHNOLOGY INSTITUTE
UNIVERSITY OF WISCONSIN
MADISON WISCONSIN***

**THE PRODUCTION OF ^{13}N FROM INERTIAL
ELECTROSTATIC CONFINEMENT FUSION**

by

John W. Weidner

**A thesis submitted in partial fulfillment of the
requirements for the degree of**

**Master of Science
(Nuclear Engineering)**

at the

UNIVERSITY OF WISCONSIN-MADISON

2003

Abstract

Accelerators and cyclotrons produce all of the medical radioisotopes with half-lives less than 30 minutes that are used in positron emission tomography (PET). One of these radioisotopes, ^{13}N , is used to label ammonia (NH_3) in order to detect coronary artery disease. Because of its 10-minute half-life, ^{13}N must be produced at or very near the location of the PET scan. This limits the availability of this procedure to those locations with accelerators or cyclotrons. This thesis describes an alternate method to produce short-lived PET isotopes. An inertial electrostatic confinement (IEC) fusion chamber using the $\text{D}-^3\text{He}$ fuel cycle generates 14.7 MeV protons, which are capable of producing ^{13}N and other short-lived radioisotopes for PET procedures. Moreover, an IEC device can be portably configured and used to produce radioisotopes at any location.

This thesis describes a proof of principle experiment in which IEC fusion reaction products are used to produce ^{13}N . Two separate experiments were conducted in which an estimated 0.20 and 0.12 nCi of $^{13}\text{NH}_3$ were produced in a 1.6 L water target containing 10 millimolar ethyl alcohol. This quantity of water was continually circulated through a stainless steel containment apparatus inside the IEC vacuum chamber, where it was irradiated with protons from the $\text{D}-^3\text{He}$ reactions. The $^{13}\text{NH}_3$ was separated from the water using a DOWEX 50WX8 (100-200) cation exchange resin column. The $^{13}\text{NH}_3$ activity in the resin column was then counted with a NaI detector. Other than the potential production of electricity from large, multi-megawatt systems, these initial experiments are believed to be the first practical use of fusion power ever demonstrated.

Acknowledgements

I could not have completed this experiment without the support and assistance of many people. First, I wish to thank Professor Gerald L. Kulcinski for allowing me to join the IEC research team and pursue this work. I hope to emulate his unwavering support and consummate professionalism in all of my future assignments. Many thanks also go to my fellow IEC students, including Greg Piefer, Ben Cipiti, Ross Radel, S. Krupakar Murali, Ben Wolter, Kunihiko “Tommi” Tomiyasu, and Brent Purviance. They spent many evenings and weekends helping me construct, install and operate my experiment. My sincere thanks also go to Robert Ashley and Dr. John F. Santarius for their invaluable assistance and advice.

Additionally, I wish to thank Professor Robert J. Nickles for focusing my efforts and sharing his insights and experience regarding radioisotope production. Acknowledgements are also due to Dr. Wilson Greatbatch and the David Grainger foundation for their financial support of IEC research. I’m also grateful to the Department of Physics at the United States Military Academy at West Point, New York for giving me the opportunity to attend the University of Wisconsin-Madison and pursue this work. Thanks also to Dr. Harrison Schmitt for his encouragement and enthusiasm for this experiment.

I deeply appreciate the assistance of the University of Wisconsin Nuclear Reactor staff, including Robert Agasie, Steve Matusewick and Todd Johnson. They generously made their detection equipment available whenever requested. I also wish to thank the Pegasus research team at the University of Wisconsin, especially Greg Winz and Ben Ford, for providing the machining assistance necessary to fabricate the water containment apparatus used in this experiment. They also graciously allowed me to use several key

pieces of equipment for my research. Thanks also to Dennis Bruggink for his help with several computer-related issues. Finally, I wish to thank my wife Michelle for her support and understanding as I completed this effort. She patiently assumed many additional responsibilities at home, which enabled me to focus my efforts on conducting this work. As always, I don't know how I would have succeeded without her.

Table of Contents

Abstract	i	
Acknowledgements	ii	
Table of Contents	iv	
List of Figures	vi	
List of Tables	ix	
Chapter 1	Experimental Objective and Overview of Positron Emission Tomography	1
Section 1.1	Objective of this Work	1
Section 1.2	Introduction to Positron Emission Tomography	2
Section 1.3	The Use of ^{13}N in PET Scans	5
Chapter 2	The University of Wisconsin Inertial Electrostatic Confinement Fusion Device	9
Section 2.1	Overview of Inertial Electrostatic Confinement Fusion	9
Section 2.2	IEC Fuel Cycles	10
Section 2.3	The University of Wisconsin IEC Device	12
Chapter 3	Design of Isotope Production System	17
Section 3.1	Separation of Radioisotope from Water Target	17
Section 3.2	Development of Experimental Apparatus	18
Section 3.3	The Model ALM1 Water Containment Apparatus	23
Section 3.4	The Model ALM2 Water Containment Apparatus	31
Section 3.5	Stainless Steel Water Containment Apparatus	32

Chapter 4	Theory of ^{13}N Activation in UW IEC	53
	Section 4.1 Theory of Isotope Production in a Pure Thick Target	53
	Section 4.2 Modification of Production Yield for Homogeneous Mixtures	57
	Section 4.3 Calculation of ^{13}N Yield in Water Target	58
	Section 4.4 Determination of Systematic Efficiencies	59
Chapter 5	Experimental Technique and Equipment	71
	Section 5.1 Water Target and Ion Exchange Resin Preparation	71
	Section 5.2 Production Run Procedure	74
Chapter 6	Experimental Results	86
	Section 6.1 February 19 th , 2003 Production Run	86
	Section 6.2 Predicted ^{13}N Yield for February 19 th , 2003 Production Run	89
	Section 6.3 February 21 st , 2003 Production Run	90
Chapter 7	Discussion of Results	108
	Section 7.1 Certainty of Experimental Results	108
	Section 7.2 Calibration Factors	110
	Section 7.3 Potential Sources of Uncertainty	111
Chapter 8	Conclusions	113
Chapter 9	Suggestions for Future Work	114
References	116
Appendix A	Counting Data from February 19th Isotope Production Run	119
Appendix B	Counting Data from February 21st Isotope Production Run	124

List of Figures

Figure 1.1	Cross section for $^{16}\text{O}(p,\alpha)^{13}\text{N}$ reactions.....	7
Figure 1.2	Diagram of coincidence detection system.....	8
Figure 1.3	PET image of damaged and healthy heart.....	8
Figure 2.1	Fusion fuel cycles used in the UW IEC device.....	14
Figure 2.2	Schematic diagram of UW IEC fusion chamber.....	15
Figure 2.3	Photo of UW IEC device in high-pressure operation.....	16
Figure 3.1	Schematic diagram of isotope production system.....	38
Figure 3.2	Graph of CSDA range vs. proton energy in water, aluminum and stainless steel.....	39
Figure 3.3	Schematic diagram of spiraling coil design for water containment apparatus.....	40
Figure 3.4	Schematic diagram of coiled water containment apparatus.....	41
Figure 3.5	Schematic diagram of “radiator” design.....	42
Figure 3.6	Schematic diagram of bar used to flatten aluminum tubes.....	43
Figure 3.7	Photograph of Model ALM1 apparatus under construction.....	44
Figure 3.8	Photograph of fully constructed Model ALM1 apparatus.....	45
Figure 3.9	Photograph of copper plumbing passing through chamber.....	46
Figure 3.10	Photograph of copper plumbing exiting the chamber.....	47
Figure 3.11	Photograph of Model ALM1 apparatus mounted inside the UW IEC chamber.....	48
Figure 3.12	Photograph of electron jet damage to Model ALM1 apparatus.....	49
Figure 3.13	Photograph of Model ALM2 apparatus.....	50

Figure 3.14	Photograph of inductive heating circuit used to solder the Model SSM1 and Model SSM2 apparatus together.....	51
Figure 3.15	Photograph of fully constructed Model SSM2 apparatus.....	52
Figure 4.1	Schematic diagram illustrating the variation in wall thickness caused by the round geometry of the tubes.....	69
Figure 4.2	Schematic diagram illustrating the fraction of the projected width of a tube that a proton can impinge upon and still enter the water target with an energy above 6 MeV.....	69
Figure 4.3	Schematic diagram showing the change in tube wall thickness in the vertical axis.....	70
Figure 5.1	Exploded view of ion exchange resin column.....	80
Figure 5.2	Photograph of ion exchange resin inside column.....	81
Figure 5.3	Photograph of ion exchange resin column mounted on the IEC chamber.....	82
Figure 5.4	Photograph of valves used to control water flow through isotope production system.....	83
Figure 5.5	Photograph of resin column on 3 x 3 NaI detector.....	84
Figure 5.6	Schematic diagram of 3 x 3 NaI detection circuit.....	85
Figure 6.1	Glowing tip of the stalk during isotope production run.....	92
Figure 6.2	Photographs contrasting the cathode heating pattern before and after the stalk began to glow.....	93
Figure 6.3	Graph of total proton current inside IEC during the February 19 th , 2003 isotope production run.....	94
Figure 6.4	Decay curve from February 19 th , 2003 isotope production run.....	97
Figure 6.5	Graph of total proton current inside the IEC during the February 19 th , 2003 run using a calibration factor of 2475.....	100
Figure 6.6	Decay curve for the February 21 st , 2003 production run.....	103

Figure 6.7	Relevant total proton current inside the IEC for the February 21 st , 2003 production run.....	104
Figure 6.8	Graph of total proton current inside the IEC during the February 21 st , 2003 run using a calibration factor of 3605.....	107

List of Tables

Table 1.1	Radioisotopes commonly used in PET scans.....	6
Table 3.1	Stopping powers of aluminum, copper and stainless steel.....	21
Table 4.1	Calculation used to approximate the integral in equation (4.9).....	66
Table 6.1	Operating conditions for February 19 th , 2003 production run.....	95
Table 6.2	511 keV count data from February 19 th , 2003 production run.....	96
Table 6.3	Total Proton current required inside the IEC to produce the activity of ¹³ N from the February 19 th , 2003 production run.....	98
Table 6.4	Calculation of calibration factor for the February 19 th , 2003 production run.....	99
Table 6.5	Operating conditions for February 21 st , 2003 production run.....	101
Table 6.6	511 keV count data from February 21 st , 2003 production run.....	102
Table 6.7	Total Proton current required inside the IEC to produce the activity of ¹³ N from the February 21 st , 2003 production run.....	105
Table 6.8	Calculation of calibration factor for the February 21 st , 2003 production run.....	106
Table 7.1	Summary of net counting data from February 19 th , 2003 run	109
Table 7.2	Summary of net counting data from February 21 st , 2003 run.....	109

Chapter 1 Experimental Objective and Overview of Positron Emission Tomography

Section 1.1 Objective of This Work

Since the discovery of fission and the invention of particle accelerators near the middle of the last century, the science of nuclear medicine has blossomed into a multi-branched field. Today, the use of radioisotopes has become commonplace across America and throughout the world. Over the past 20 years, new imaging procedures have enabled physicians to view the human body in ways unimaginable only a few decades ago. The large, expensive machines used to produce the radioisotopes for these procedures, however, have remained essentially unchanged since their invention nearly 60 years ago. This work seeks to develop a new method of creating a specialized class of radioisotopes for use in highly advanced imaging procedures.

The purpose of this proof-of-principle experiment is to produce a short-lived radioisotope utilizing a flux of protons created from fusion reactions. Specifically, the objective of this experiment is to create ^{13}N , a positron-emitting radionuclide, which has a 10-minute half-life and is used in specialized medical imaging routines known as positron emission tomography (PET) scans. Early on in this experiment, ^{13}N was chosen as the radioisotope for production for several reasons.

First, ^{13}N can be created from $^{16}\text{O}(p,\alpha)^{13}\text{N}$ reactions in a water target. This is very attractive due to water's invariant chemical makeup, common availability, and near-zero cost even for reverse osmosis, de-ionized (ultra-pure) water.

Second, the energy dependent cross sections for $^{16}\text{O}(p,\alpha)^{13}\text{N}$ reactions [1] are well suited to the 14.7 MeV protons from D- ^3He fusion as shown in figure 1.1.

Third, the 10-minute half-life of ^{13}N makes it an attractive product for portable isotope production devices. Cyclotrons and linear accelerators produce essentially all medical PET isotopes with half-lives under a few hours [2]. These machines can cost millions of dollars and are relatively immobile. Consequently, the isotope delivery range for these facilities is limited by the half-lives of the radioisotopes they produce; the shorter the half-life, the shorter the distance it can be delivered and still arrive with the desired activity. An IEC and all associated equipment, however, could be engineered to fit on a vehicle or trailer. Such a vehicle could be driven to any remote location to produce short-lived isotopes on site, greatly expanding the short-lived PET isotope market.

Fourth, the Center for Medicare and Medicaid Services (a branch of the Department of Health and Human Services) announced on April 16th, 2003 that ^{13}N -ammonia PET scans for myocardial perfusion will be reimbursed in the future [3]. According to the announcement, the “national coverage determination will be published in the Medicare Coverage Issues manual.” The policy change will become effective as of the date listed in that publication. Considering this decision, the demand for ^{13}N should significantly increase, which should also increase the demand for portable and inexpensive radioisotope production facilities. IEC devices may one day be able to fill at least part of that anticipated demand, and it’s believed that this work marks the first known attempt to purposefully use fusion reactions for a specific, commercial purpose. The rest of this chapter elaborates on the medical use of ^{13}N in order to provide the reader with a general introduction to how and why ^{13}N is used in PET.

Section 1.2 Introduction to Positron Emission Tomography

Radioactive materials were put to medical use almost immediately after W. C. Roentgen's discovery of the x-ray in 1895. It's not surprising that many of these early applications focused on using x-rays to image internal structures of the body such as bones and teeth; Roentgen discovered x-rays by noting how they were able to develop photographic film, and later used the level of film exposure to determine the attenuation of x-rays by various thicknesses of material [4]. By placing a naturally radioactive source over a patient's hand that was on top of a photographic plate, crude but effective images of the bone structure were made. This was a significant leap forward in the ability to locate broken bones, remove foreign objects and treat a host of other ailments.

During the first half of the twentieth century, great improvements were made to x-ray imaging film systems and x-ray tubes. Despite these improvements, the fundamental shortcoming of x-ray images would never be overcome; X-ray images are two-dimensional projections of a three-dimensional distribution of objects. For example, when a chest x-ray is taken of a patient to view the lungs, the resulting image also contains images of the ribs, heart, spine and other structures overlaid on the image of the lungs. Consequently, a large portion of the lungs are masked by these structures. During the second half of the century, however, technological advances in radiation detectors and the creation of new radioisotopes using particle accelerators and fission reactors led to the development of a new class of imaging procedures called tomography. Tomographic images are two-dimensional representations of a thin plane or "slice" in a three-dimensional object. Hence, images can be made of structures in one plane of a patient without overlap from structures in other planes. The family of modern tomographic imaging techniques includes single-photon

emission computed tomography (SPECT), x-ray computed tomography (x-ray CT), magnetic resonance imaging (MRI), and positron emission tomography (PET).

Of the tomographic imaging techniques listed above, PET is unique in two respects. First, unlike CT or MRI that show only body structure, PET provides a real-time visual image of physiologic processes [5]. This is achieved by incorporating a positron-emitting radionuclide into a compound that is normally associated with the physiologic processes of the tissue to be imaged. A PET scan monitors the perfusion and concentration of the tracer as it is absorbed and diffused throughout the intended tissue. The rate at which the tracer is absorbed or diffused is visually monitored and indicates if the tissue is healthy, unhealthy or cancerous. Standard x-ray procedures and other tomographic imaging techniques do not provide these physiological insights.

The second unique aspect of PET is that it relies on a very special radiation event to create images. As the name implies, positron emission tomography employs positron-emitting radionuclides in order to create tomographic images. Positrons are the antiparticle of electrons; they have the same rest mass (511 keV) but are positively charged. When a radionuclide emits a positron, the positron will travel through the surrounding media and continuously lose energy via Coulomb force interactions. In general, the positron will annihilate with an electron after it has lost essentially all of its linear and angular momentum [6]. This annihilation event transforms the rest mass of the particles into two oppositely directed 511 keV photons.

The fact that positron annihilations generate two equal photons emitted in exactly opposite directions can be utilized to create a specialized photon detection system. These systems are called coincidence detection systems because they will only register an event if

two separate detectors both detect a photon within a very narrow time window [7]; if these two events occur within the time window, they are said to be in coincidence. It is very unlikely that two independent radiation events will trigger both detectors within the coincidence window, which is usually on the order of a few nanoseconds. Therefore, the coincidence circuit excludes nearly all background radiation events. Moreover, the origin of a positron annihilation event is confined to the small volume between the two detectors as shown in figure 1.2. When a ring of coincidence detection circuits is placed around the patient, the location of the positron-emitting isotope as a function of time can be pinpointed with great accuracy. In fact, modern PET scanners have a resolution on the order of a few millimeters. The uptake or diffusion of the tracer over time as seen in the PET image is then compared with a physiological model to determine the condition of the organ or tissue.

Section 1.3 The Use of ^{13}N in PET Scans

As shown in table 1.1, ^{13}N is one of several radioisotopes used in PET. Cyclotrons are often used to produce this radioactive isotope of nitrogen from $^{16}\text{O}(p,\alpha)^{13}\text{N}$ reactions in a water target. The individually created ^{13}N atoms bond with hydrogen to form $^{13}\text{NH}_3$ ammonia molecules. The ammonia is separated from the water and injected into the bloodstream of a patient. The typical activity of ^{13}N -ammonia used for a PET scan is approximately 20 mCi [8], and the high proton currents available in cyclotrons ($\sim 100 \mu\text{A}$) enable them to easily generate this ^{13}N activity in water targets [2]. Although this is a rather large initial activity, the 10-minute half-life results in a total dose to the patient that is similar to that received from standard x-ray procedures.

Radioisotope	^{11}C	^{13}N	^{15}O	^{18}F
Half-life (min)	20.4	10.0	2.0	109.8
Daughter Product	^{11}B	^{13}C	^{15}N	^{18}O
Formation Reaction	$^{14}\text{N}(\text{p},\alpha)$	$^{16}\text{O}(\text{p},\alpha)$	$^{15}\text{N}(\text{p},\text{n})$	$^{18}\text{O}(\text{p},\text{n})$

Table 1.1 – The most common radioisotopes used in PET imaging procedures. Note that deuterons could also be used as the bombarding particle to create ^{15}O and ^{18}F from ^{14}N and ^{20}Ne , respectively.

The overwhelming majority of ^{13}N -ammonia PET scans are conducted to determine if there is cardiac artery disease in the heart [8,9,10]. Cardiac artery disease clogs the blood vessels of the heart muscle (myocardium), which can cause the portions of the muscle fed by these vessels to die. In a PET scan, these dead areas are not perfused with the ^{13}N ammonia as shown in figure 1.3. Since no radionuclide reaches these areas, they appear as dark regions in the visual PET image of the heart. These ^{13}N -ammonia PET scans are an attractive option to test for coronary artery disease for several reasons: they enable a non-invasive evaluation of myocardial blood flow; they possess high temporal resolution that enables in vivo measurements of regional blood flow; and quantitative assessment of blood flow is possible using validated radiopharmaceutical kinetic models [11]. Moreover, PET has the ability to correct for photon attenuation within large patients. For this reason, PET may be an attractive option for larger patients whose body attenuation may obscure the results from SPECT procedures using low-energy photons from $^{99\text{m}}\text{Tc}$.

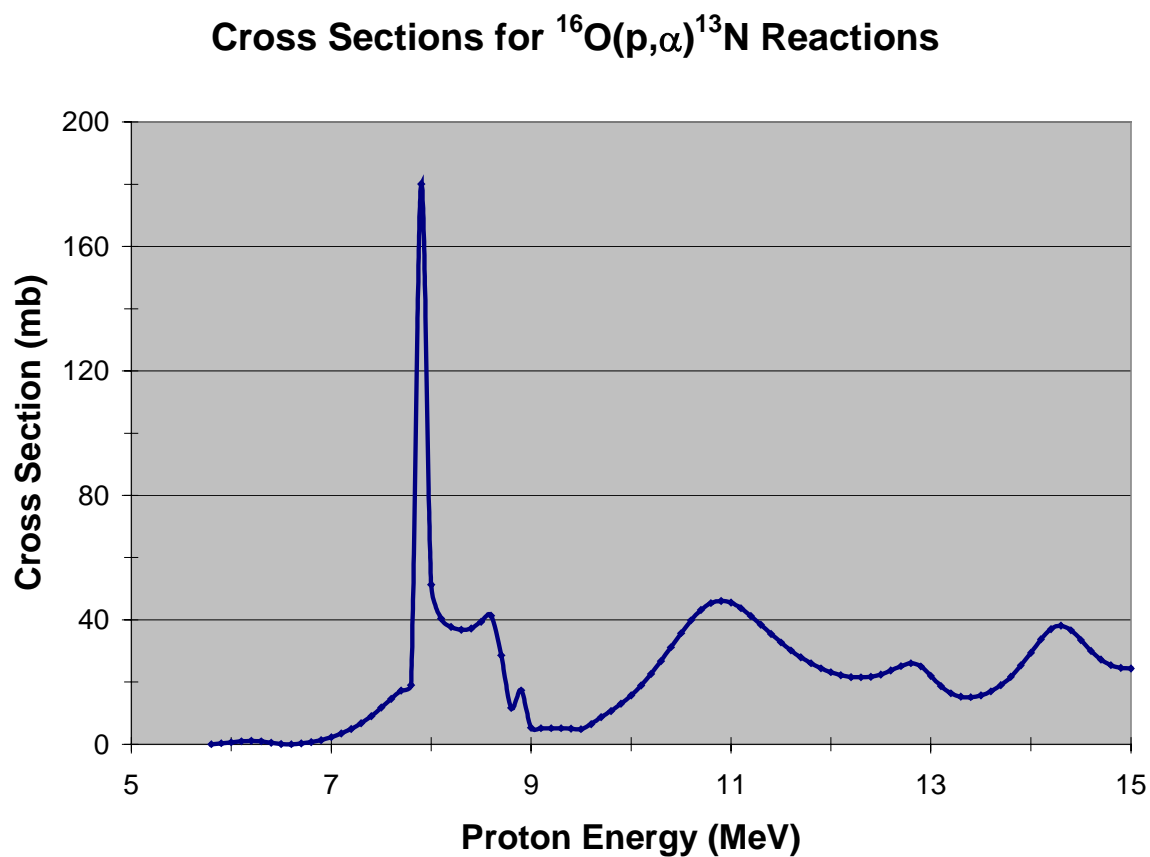


Figure 1.1 – Cross section for $^{16}\text{O}(p,\alpha)^{13}\text{N}$ reactions. The 14.7 MeV protons generated from D- ^3He fusion are well suited to this reaction. This data was taken from IAEA's charged particle cross section database for medical radioisotope production [1] at <http://www-nds.iaea.or.at/medical/index.html>.

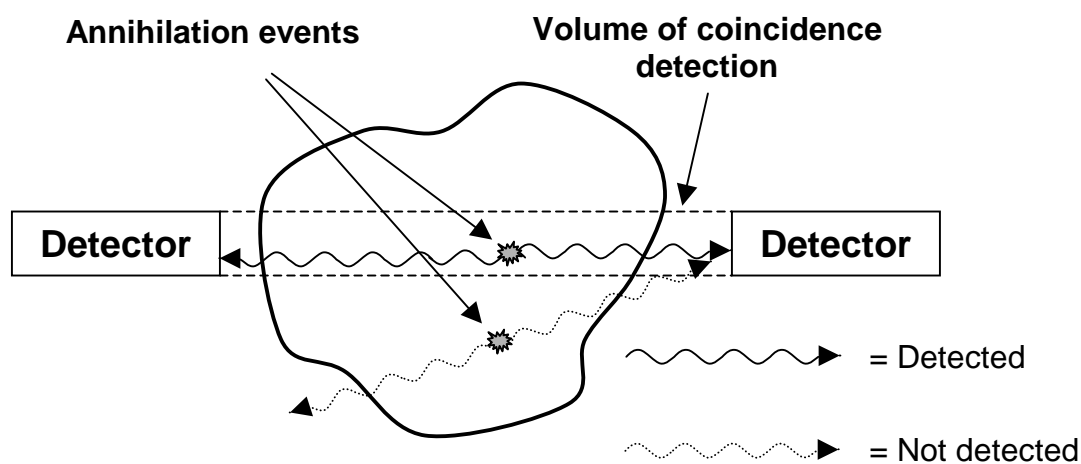


Figure 1.2 – Diagram illustrating the principles of coincidence detection. In order to be recorded as a coincidence event by the circuit, each detector must essentially detect an event simultaneously. Consequently, only annihilation events that occur within the volume of coincidence detection will be recorded.

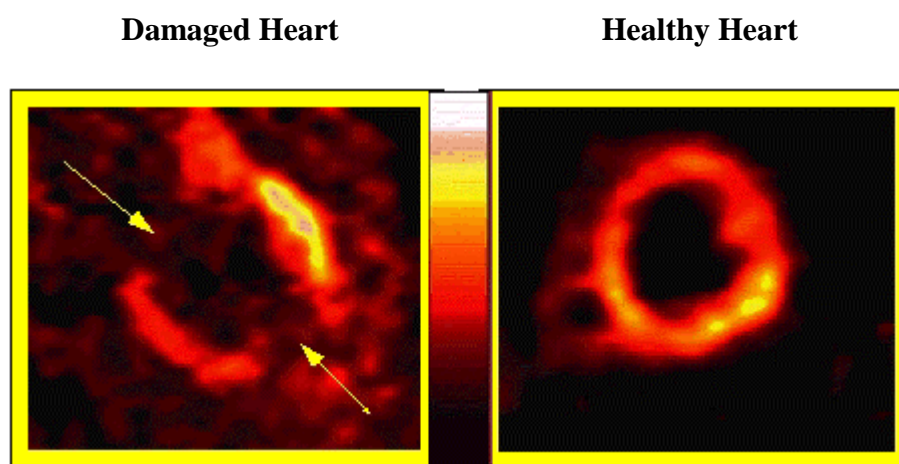


Figure 1.3 - PET image of a heart taken from Web site of the Biomedical Research Foundation of Northwest Louisiana, <http://www.biomed.org/pet.html>. The left image shows a PET image of a patient that has suffered a heart attack. The dark areas pointed out by the arrows are not perfused with $^{13}\text{NH}_3$, indicating “dead” myocardial tissue. The image on the right is a PET image of a healthy heart.

Chapter 2 The University of Wisconsin Inertial Electrostatic Confinement Fusion Device

Section 2.1 Overview of Inertial Electrostatic Confinement Fusion

In the simplest terms, an inertial electrostatic confinement (IEC) fusion device is a machine that uses large electrostatic potential differences to accelerate positive isotopic ions, such as hydrogen or helium, into a central dense core region within a vacuum chamber. If these ions have enough energy when they reach the dense core, there is a probability that two ions will fuse together into a single atom, releasing particles and excess energy in the process. Often designed for spherical symmetry, the ions that don't fuse during their first pass through the core may continue to oscillate within the electrostatic potential well and fuse during later passes through the core. A portion of the ion population is continually removed during operation by several loss mechanisms, including charge exchange reactions with the background gas and collisions with the wires of the anode and cathode. However, the practical simplicity, relatively small size and inexpensive cost make this type of fusion attractive for many potential applications including isotope production, clandestine material detection through neutron activation, and possibly even small power production devices.

Although a few IEC research programs, such as at the University of Illinois [12], have been in place for several decades, few IEC fusion programs existed prior to the 1990s [13-16]. At that time, IEC fusion seemed to have a very limited future. A discovery in 1987, however, re-ignited interest in IEC fusion and provided an opportunity for this little talked about form of fusion to make its mark. In that year, researchers at the University of

Wisconsin-Madison realized that the upper three meters of lunar regolith contained approximately one million tons of ^3He [17,18]. This resource could be harvested from the moon and used as a fusion fuel for future large-scale electrical generation; moreover, IEC fusion might very well be the most appropriate method to utilize this advanced fuel cycle. This realization generated renewed interest in IEC fusion and spurred the development of IEC research programs at the University of Wisconsin, Marshall Space Flight Center, Los Alamos National Laboratory, as well as programs at several locations in Japan and the ongoing studies at the University of Illinois [16].

Section 2.2 IEC Fuel Cycles

Two types of fusion fuels are currently used in the UW IEC device – deuterium (D) and ^3He . These fuels can be used individually or combined to produce the reactions listed below. These reactions are also depicted in figure 2.1.

- $\text{D} + \text{D} = 50\% \Rightarrow \text{T} (1.01 \text{ MeV}) + \text{p} (3.02 \text{ MeV})$
 $ \phantom{\text{D} + \text{D}} = 50\% \Rightarrow \text{}^3\text{He} (0.82 \text{ MeV}) + \text{n} (2.45 \text{ MeV})$
- $\text{}^3\text{He} + \text{}^3\text{He} \Rightarrow \text{}^4\text{He} + 2\text{p} (12.86 \text{ MeV total})$
- $\text{D} + \text{}^3\text{He} \Rightarrow \text{}^4\text{He} (3.67 \text{ MeV}) + \text{p} (14.68 \text{ MeV})$

Each reaction above has advantages and disadvantages. The D-D reactions are easiest to produce since the fusion cross section becomes nonzero at the lowest energy. When creating D-D reactions, there is an equal probability of producing either a tritium atom (T) and a proton (p), or a ^3He atom and a neutron (n). Each of these outcomes can be disadvantageous. Although the overall production of tritium within the UW IEC in its current operating regime is minute, the production of this radioactive and highly regulated byproduct will become an issue in any large-scale D-D fusion program. Moreover, the

production of tritium may indirectly cause some D-T reactions, which also produce neutrons. The second reaction branch results in the direct production of fast neutrons, which can damage the lattice structure of the containing vacuum chamber and cause it to become radioactive. These neutrons will also interact with nearby equipment, potentially causing further operational complications. These same neutrons could be put to useful purposes, however; an IEC machine could be used to purposefully activate materials, such as those within cargo containers or luggage, in an effort to detect clandestine items [19].

The ${}^3\text{He}$ - ${}^3\text{He}$ fusion reaction is very advantageous since it does not produce any radioactive products or neutrons. If this form of fusion can be achieved on a large scale ($> 10^{15}$ reactions/sec), then a truly pollution-free source of energy may be attainable [20,21]. Unfortunately, the fusion cross section for ${}^3\text{He}$ ions only becomes significant at very large center-of-mass energies (applied potentials in excess of ~ 200 kV). This has prevented the demonstration of ${}^3\text{He}$ fusion in any device to date. Significant research into this reaction is ongoing at the University of Wisconsin, and a new chamber has been obtained solely for this purpose.

The third fusion reaction, D- ${}^3\text{He}$, has the very useful result of producing high-energy protons. Burning deuterium and ${}^3\text{He}$ in the IEC chamber does lead to D-D side reactions and their associated neutrons; however, the reaction rate of each D-D reaction branch is small enough at current operating regimes that the damage to and activation of materials is negligible. This enables the high-energy protons from D- ${}^3\text{He}$ fusion reactions to be beneficially exploited [22,23,24].

As stated, the goal of this proof-of-principle experiment is to produce ${}^{13}\text{N}$ from the oxygen atoms in a water target. However, the 14.7 MeV protons from D- ${}^3\text{He}$ fusion are

energetic enough to produce all of the PET isotopes listed in table 1.1. In fact, the cross sections for the other reactions are even more favorable than those for ^{13}N . Therefore, isotope production may serve as an early application for IEC fusion devices en route to a long-term goal of power production [22].

Section 2.3 The University of Wisconsin IEC Device

The UW IEC device is a two-grid, spherically symmetric IEC system contained within an aluminum vacuum chamber that has the shape of a right circular cylinder. Figure 2.2 shows a schematic diagram of the device, and figure 2.3 shows a photograph of the chamber while in operation at high pressures (~ 8 mtorr). The inside of the vacuum chamber is 65 cm tall and 91 cm in diameter. The two grids of the IEC reside within this volume. The outer grid, or anode, is made of stainless steel wires that are approximately 2 mm in diameter. During operation, the anode is either maintained at zero potential via a grounding connection or biased with a few hundred volts of negative potential. A large negative potential is then applied to the inner grid, or cathode, which is fabricated from 0.8 mm diameter tungsten-rhenium wire. For most UW applications, this negative potential ranges from 40,000 to 160,000 volts, although operations to date have reached 180 kV.

This large negative voltage is generated by a HipotronicsTM DC power supply. The supply is capable of producing up to 200,000 volts DC, either positive or negative, with up to 75 mA of current. This electrostatic potential is transferred to the IEC chamber inside an oil-filled feedthrough container, where it is carried to the cathode along a solid 0.32 cm molybdenum rod. This rod is seated inside a 1.9 cm diameter boron-nitride stalk to prevent the large voltage from shorting to the chamber walls and feedthrough. The cathode is

mounted directly to the molybdenum rod at the end of the stalk. When properly assembled, the cathode is centered on the vertical and horizontal axis of the vacuum chamber.

A proton detector is mounted on the horizontal axis of the chamber to monitor the D-³He reaction rate. This detector was a 1200 mm², ion-implanted, surface barrier detector from Ametek Industries, mounted 81 cm from the center of the cathode. The proton detector only sees a small fraction of the total number of protons produced inside the IEC because it is located at the end of a tube. This detection volume is approximated in figure 2.2

To ionize the gaseous fuel, three filaments from standard 200-watt light bulbs are mounted equidistant from each other on the same plane of the vertical chamber walls. As current is applied to the filaments, they become very hot and emit electrons via thermionic emission. These electrons ionize a small fraction of the gaseous fuel within the chamber, causing the now positive ions to be accelerated towards the cathode. The typical operating pressure inside the chamber is approximately 2 mtorr, and the ratio of D to ³He is maintained at 1:1 as measured by the residual gas analyzer (RGA).

The projected area of the solid cathode wires comprise only 8% of the surface area of the cathode, so the cathode is 92% transparent to the ions. Theoretically, the spherical geometry of the cathode causes the ions to converge at its center, creating a dense core of ions. In reality, as much as 2/3's of the D-³He fusion reactions are thought to occur as embedded reactions approximately one micron deep in the cathode wires [25]. In either event, the 14.7 MeV protons are isotropically emitted. Hence, the first challenge of this experiment was to design a water containment system to intercept a portion of these protons for ¹³N production.

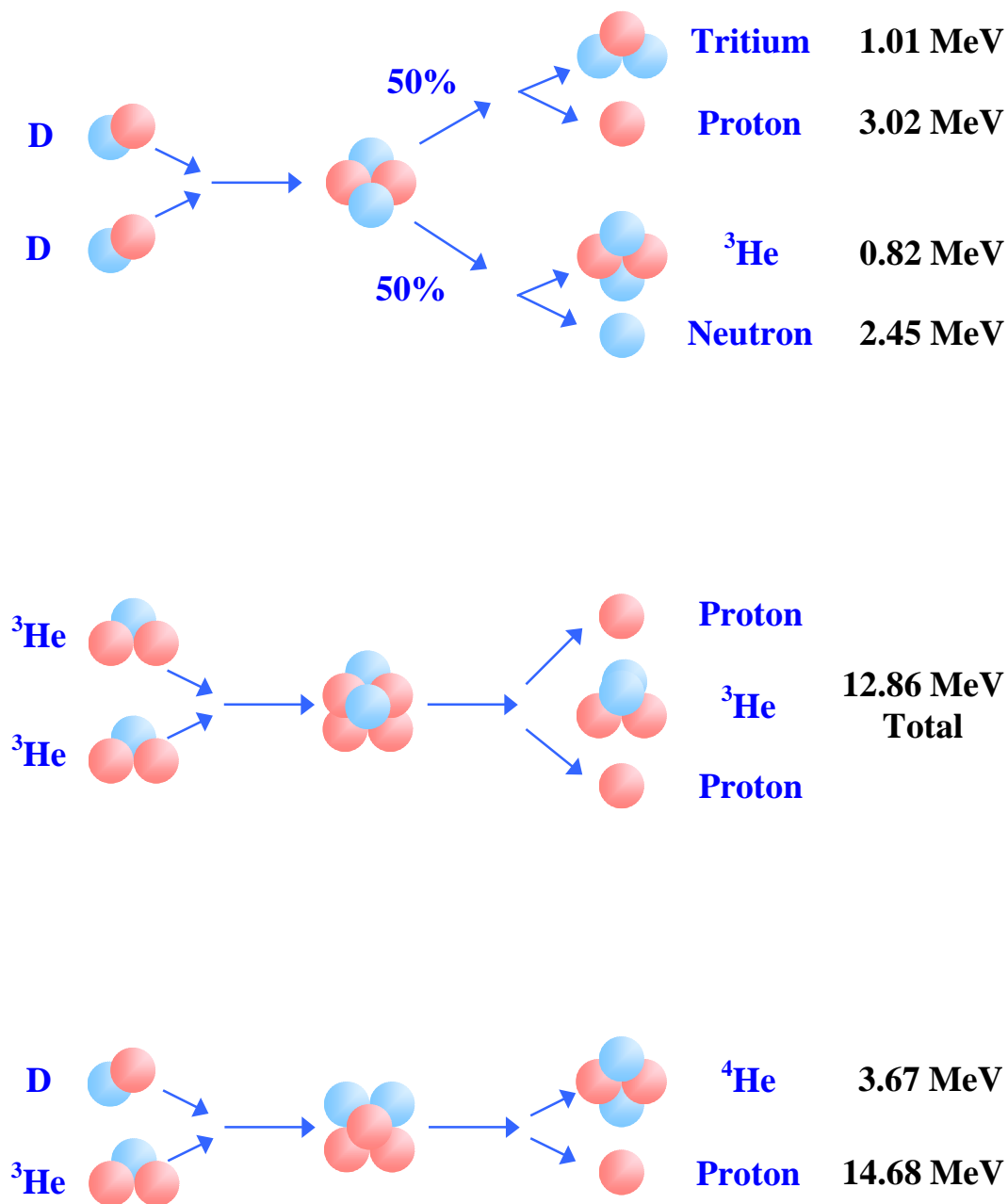


Figure 2.1 – Fusion cycles used in the UW IEC chamber. No fusion device has yet been able to demonstrate ^3He - ^3He fusion due to the very large electrostatic potentials (> 200 keV) required.

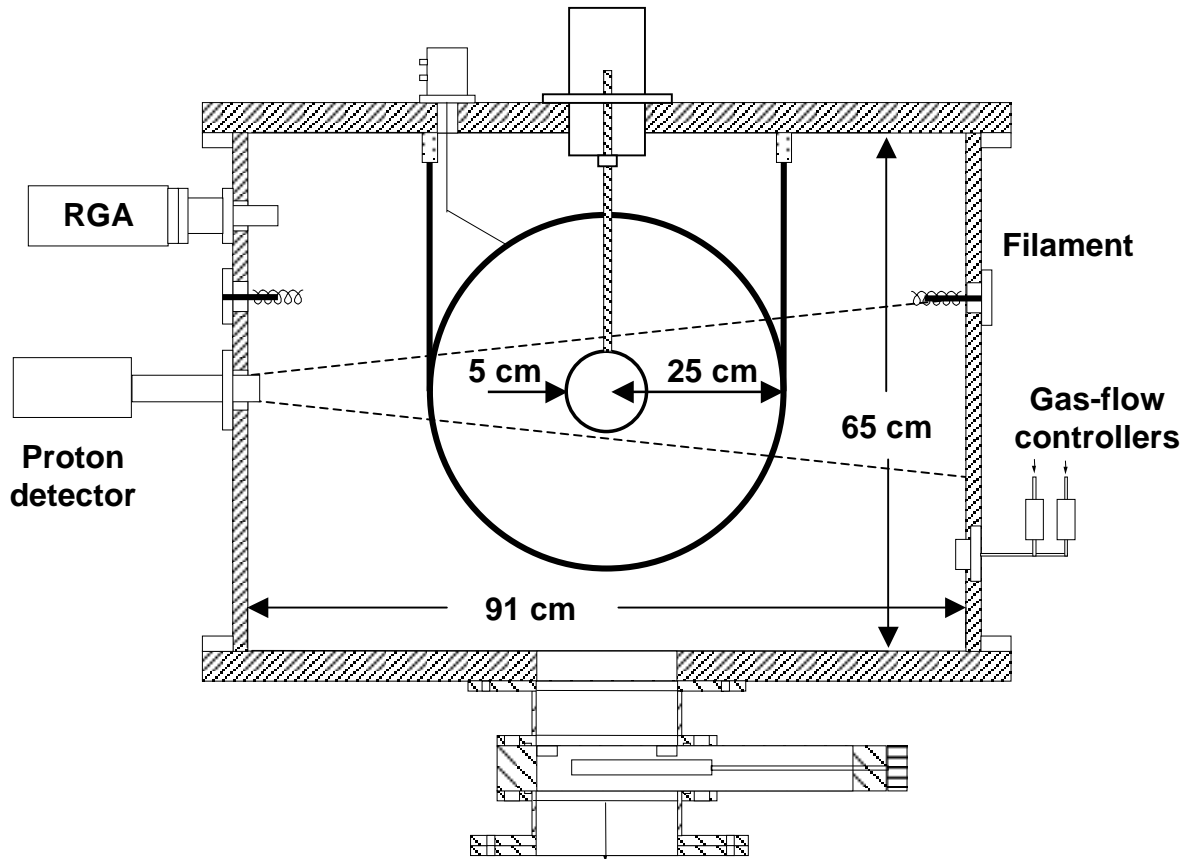


Figure 2.2 – Schematic diagram of the UW IEC fusion chamber. The vacuum chamber is a right circular cylinder made of aluminum. It is air-cooled and fans are used to maintain it below its maximum operating temperature. The 1200 mm^2 proton detector is mounted in a water-cooled housing to minimize the dark current caused by thermal noise. The residual gas analyzer (RGA) monitors the composition of the gases inside the chamber. Typical D- ^3He operating pressure is approximately 2 mtorr, and the D to ^3He ratio is maintained at 1:1 as measured by the RGA. The base pressure between operational runs is on the order of 1 μtorr .

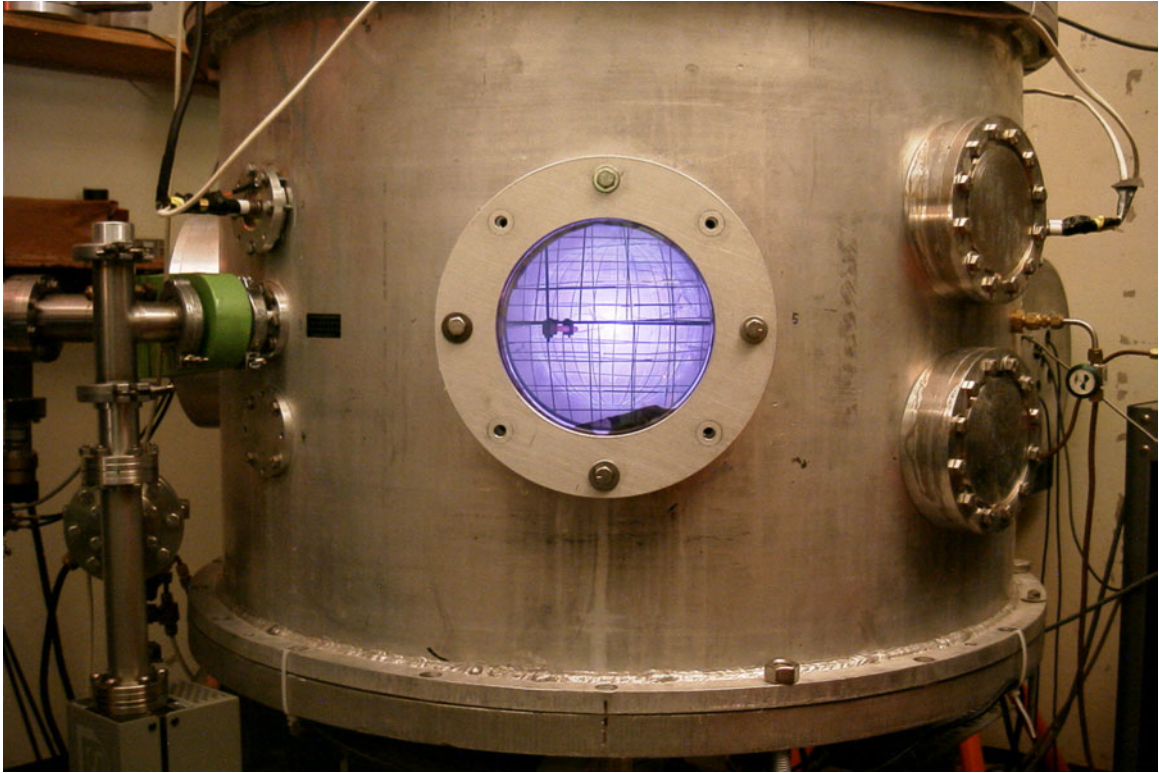


Figure 2.3 – The UW IEC chamber in operation using deuterium fuel at a pressure of approximately 8 mtorr.

Chapter 3 Design of Isotope Production System

Section 3.1 Separation of Radioisotope from Water Target

Shortly after deciding to create ^{13}N using protons from D- ^3He fusion, a process was devised that would allow the radioisotope to be separated from the water target in order to efficiently measure its activity. Fortunately, separating ^{13}N from its water environment is a rather easy process. In this experiment, the ^{13}N is created monotonically. If one can manipulate the water environment such that the ^{13}N atoms form a specific compound, these compounds can easily be separated from the water through basic chemical processes. In fact, the University of Wisconsin's Medical Physics department uses this exact methodology when they produce ^{13}N for PET scans using a cyclotron. By preparing a water target that contains approximately 10 millimolar of ethyl alcohol, the ^{13}N atoms are driven to form $^{13}\text{NH}_3^+$ ammonia ions. These positive ions are then removed from the water target by flowing the water through a column of ion exchange resin. Ion exchange resins are polymer compounds possessing numerous ionic sites. Each site can reversibly exchange either cations or anions (depending upon the resin) with similarly charged ions in the surrounding solution. Thus, these resins trap compounds without altering their chemical properties [26].

For this experiment, DOWEX 50WX8 (100-200) cation exchange resin is used. The DOWEX resin employs SO_3^- ions (covalently bound to the resin polymer) as ionic sites, and H^+ ions (ionically bound to the SO_3^-) as the vehicles for ion exchange. For this experiment, the H^+ atoms are replaced with Na^+ ions by rinsing the resin in a solution of 0.1 molar NaOH (see Chapter 5, Section 5.1). When the water containing the $^{13}\text{NH}_3^+$ ions is passed

through a column of DOWEX 50WX8 (100-200) resin, the resin exchanges its Na^+ ions for $^{13}\text{NH}_3^+$ ions, thereby trapping the ^{13}N in a volume small enough to measure its activity.

A second advantage of promoting the creation of $^{13}\text{NH}_3^+$ ammonia atoms is that this is the form in which ^{13}N is delivered to patients during a PET scan [8,9,10]. Before being administered, the final solution of ^{13}N ammonia must be sterilized, checked for chemical and radionuclide purity, and so on. Since the chemical form of the ^{13}N ammonia solution is the same chemical form in which it will be administered to the patient, it eliminates the need for intermediate chemical processes.

Section 3.2 Development of Experimental Apparatus

Once the water target was selected and the radioisotope separation method determined, designing a comprehensive production system was straightforward. The system includes the following items:

- 1) A container placed inside the IEC to hold the water target.
- 2) A pump to circulate water through the closed system.
- 3) A heat exchanger to remove heat from the water. The IEC needs to operate in excess of 140 kV and 30 mA during isotope production runs. These conditions generate more than 4 kW of power inside the chamber, some of which will be transferred to the water as heat. This heat must be removed to prevent the formation of steam that could rupture the tubes and severely damage the vacuum pumps.
- 4) A water expansion reservoir which allows the volume of water to increase with temperature. This reservoir also offers an escape for air trapped within the water circuit.
- 5) An ion exchange column to separate the $^{13}\text{NH}_3^+$ from the water.

The above components are arranged in a closed loop isotope production system as shown in figure 3.1. This circuit continually circulates the same volume of water through the water containment apparatus within the IEC, where it is irradiated with protons.

The first and obvious challenge in developing a method for producing ^{13}N from a water target in an IEC chamber is how to contain the water. To efficiently produce isotopes, the containment material must be thin enough to enable the protons to pass through with as little energy loss as possible. Moreover, it has to be robust enough to withstand the internal water pressure, the plasma environment, electron jets and the heat generated inside the IEC chamber. Since it is used in a vacuum environment, the material can not significantly outgas, nor can the products used to create joints and connections in the material.

With these characteristics in mind, thin-walled metallic tubing quickly becomes the only viable alternative. Plastics were judged to be too sensitive to the plasma and electron jets emanating from the plasma. It was also feared that the poor thermal conductivity of plastic would not enable the water inside to cool a plastic container well enough to prevent the development of leaks. Additionally, creating joints with plastic materials requires the use of glues containing hydrocarbons, which may significantly outgas or react with the plasma. Hence, plastic was eliminated as a possible water containment material. Glass was also considered as a possibility, but the expense of creating a thin-walled glass structure, and the inherent fragility of such a structure, lead to its rejection. Finally, some initial research concluded that ceramics, carbon fiber objects and other exotic materials would be either too expensive, too difficult to work with or both. As a result, thin-walled metallic tubing became the design material for a water containment apparatus.

The more energy the protons enter the water target with, the larger the yield of ^{13}N will be. In order to enable a proton to pass through it and retain a significant fraction of its original energy, the wall of a metallic tube would need to be very thin indeed. Hence, initial planning and design efforts focused on finding metallic tubing of a thickness such that the incident protons only lost approximately 2 MeV in traveling through the tube wall. This results in the proton entering the water target with approximately 12.5 MeV of energy.

To determine the wall thickness that would enable the protons to retain 12.5 MeV of energy (assuming they are incident normal to the tube wall), the range and stopping powers of several materials were investigated. Figure 3.2 plots the continual slowing down approximation (CSDA) range of protons in aluminum, stainless steel and water [27]. The range of protons in copper was also examined and found to be so similar to stainless steel that the two could not be differentiated when plotted together in figure 3.2. Consequently, it was not included in the graph. Figure 3.2 clearly demonstrates that a 15 MeV proton has more than twice the range in aluminum than in stainless steel (or copper).

Comparing the stopping powers of these materials for a 14.7 MeV proton also demonstrates the advantage of aluminum. Table 3.1 lists the stopping power for 14.7 MeV protons in the three materials, and the thickness of material that would attenuate a 14.7 MeV proton to 12.5 MeV. This table demonstrates that aluminum tubes could have a wall thickness more than twice that of copper or stainless steel tubes for the same proton energy degradation. This fact proved to be an advantage since tubes with a wall thickness as small as 0.012 cm are difficult to procure.

	Al	Cu	SS
Stopping Power (MeV /cm)	67.66	181.97	172.23
Wall thickness to slow a proton to 12.5 MeV (cm)	0.0325	0.0121	0.0127

Table 3.1 – Stopping power of various metallic tubing materials and the wall thickness required to slow a 14.7 MeV proton to 12.5 MeV [27].

In an attempt to create a simple and adaptable water containment apparatus, initial designs focused on using coils of thin-walled tubing. One design called for a spiral target that expanded out from a central water inlet much like an old fashioned children’s lollipop (figure 3.3). This target could be placed at the bottom of the chamber under the anode and would intercept a significant portion of the protons produced. A second design (figure 3.4) specified a coil of tubing that would wind around the inner wall of the IEC chamber. If the coil covered the height of the IEC chamber wall from top to bottom, this target would intercept an even larger fraction of the protons produced. Both designs had the benefit of having only two connections – one on each end of the coil of tube. Fewer connections obviously reduces the opportunity for leaks to develop at such junctions. Unfortunately, no commercially manufactured coiled tubing could be found with walls thin enough for this experiment. Several manufacturers contacted in regard to this coiled tubing stated that such thin walled tubing was too susceptible to kinking during handling to be a practical commodity. Therefore, these designs were rejected. If a manufacturer could be found that would make a coil of thin walled tubing, it’s believed these would be very successful designs.

After further deliberation, a design was selected that incorporated numerous tubes closely aligned alongside each other and connected by manifolds at either end. As shown in

figure 3.5, this design was very similar to a car radiator; hence, “the radiator” became its unofficial nickname. Water would flow in one end of a manifold, be distributed among the approximately 65 tubes, and then flow out the opposite end of the second manifold. The flow was directed in and out of the “radiator” at opposite corners in order to encourage an even flow of water through each tube. If sized appropriately (about 60 cm x 60 cm), this design can either be placed vertically in the IEC chamber between the anode and the chamber wall, or horizontally between the anode and chamber floor. Assuming an isotropic distribution of protons from a point source in the center of the cathode, neither location provides an advantage in terms of the proton flux. There was some concern that a horizontal orientation might inhibit the outflow of gas through the turbo-pump at the bottom of the chamber, but later experiments with this orientation did not demonstrate any pumping restrictions.

Although feasible, this design does have some apparent drawbacks. One concern is that the flow will not be equally distributed, causing the flow in some tubes to be very slow relative to the others. The water in these tubes might then become hot enough to turn to steam and rupture the system. It was felt that this could be overcome by moderating the flow rate to ensure adequate flow through all tubes, though. Later experiments demonstrated that a total flow rate of approximately one liter per minute provided adequate flow through all the tubes. Another concern with this system is the significant number of joints needed to fabricate this design. Incorporating approximately 65 tubes necessitates 130 joints – two for each tube. Not only does this increase the effort required to fabricate the apparatus, but these numerous joints may also be a potential source of leaks. This concern was eventually realized.

Section 3.3 The Model ALM1 Water Containment Apparatus

As previously described, aluminum tubing of wall thickness 0.0325 cm reduces the energy of a 14.7 MeV proton to approximately 12.5 MeV. Moreover, aluminum tubing is readily available and relatively inexpensive. Hence, the first isotope production system was built using aluminum tubes as the foundation of the water containment apparatus. Because it was fabricated from aluminum tubing and was the first model built, this system was designated the Model ALM1.

The first step in constructing the Model ALM1 apparatus was to obtain the appropriate tubes. Since the range of a 12.5 MeV proton in water is less than 0.2 cm, the diameter of the tubes in the Model ALM1 did not need to be very large. For simplicity of handling and adequate flow capability, however, ¼ inch (0.635 cm) nominal diameter aluminum tubes were selected. These tubes were purchased from the McMaster-Carr Supply Company of Chicago, Illinois. Each type 3003 alloy aluminum tube was two-meters in length and 0.64 cm in diameter with a wall thickness of 0.036 cm. These tubes reduce the energy of a 14.7 MeV proton to approximately 12.3 MeV.

The two-meter long sections of aluminum tubing were cut to 58 cm lengths by hand using standard pipe cutters. These cutters severed the tubes cleanly, but care had to be taken to prevent crushing the tubes by applying too much force with the cutting wheel. Once cut, the inside of the tubes were cleaned in a four-step process. First, the tubes were cleaned in hot soapy water using a 223 caliber rifle cleaning kit with copper bore brush. Each tube was cleaned just as if it were the bore of a rifle. After this was done, the tubes were cleaned in a similar manner using hot water only. This was done to rinse away the soap. The tubes were

then blown dry using compressed air and rinsed with acetone to remove any remaining traces of grease. Finally, the tubes were rinsed with alcohol to remove the acetone.

The last step in preparing the tubes was to flatten their middle portions. This was done to provide a flat tube face to the protons incident perpendicularly to the tube's projected area. By having a flat face instead of a round face, the wall thickness across the entire width of the tube would be uniform (see Chapter 4, Section 4.4, Paragraph 5 for further discussion of this effect). The ends of each tube were not flattened in order to ensure their original round geometry would fit tightly into the round holes drilled in the manifolds.

Flattening the middle portion of each tube was accomplished using two large metal bars approximately 10 cm wide, 2.5 cm thick and 45 cm long. Six washers were glued onto the face of one bar to prevent the face of the second bar from getting closer than about 0.4 cm to the face of the first. Additionally, the edges of each end of the bars were rounded to provide a smooth transition from the flattened portion of the tube to the round end (see figure 3.6). A tube was placed on the bar with the washers, and the second bar was placed on top of the tube sandwiching it between the bars. The bars were then placed in a press and the top bar was forced down upon the bottom bar, flattening the tube to a thickness of approximately 0.4 cm in the process.

After flattening several tubes in this manner, it was observed that this process caused the tubes to take on a "figure 8" shape; the tubes were rounded on the edges with a crease down the middle of both sides. To flatten the face of the tubes as intended, each tube was slightly expanded by pressurizing it to approximately 100 psi. This was accomplished by capping one end of a tube with a Swageloc™ fitting, and using a similar fitting on the other end to connect it to the regulator of a high-pressure nitrogen tank. This caused the tubes to

take on a “pointed oval” shape much like a cat eye. Although requiring considerable time and effort, the final tube shape presented a much more consistent wall thickness to incident protons than the original round shape.

Once the tubes were prepared, the manifolds were fabricated. These were machined from two $\frac{3}{4}$ inch (1.91 cm) nominal diameter aluminum rods cut to 60 cm lengths. The first step was to bore a $\frac{1}{4}$ inch (0.635 cm) diameter hole through the center length of the rods using a lathe. This was done by drilling from both sides in several steps and having the two bore holes meet in the middle of the rod. To ensure the two holes met as designed, the holes were initiated with drill bits only 12 cm long. This minimized the sag and wander in the drill bit and ensured each hole was started “true”. The holes were bored approximately 0.5 cm at a time. That is, the drill would be fed approximately 0.5 cm into the rod then backed all the way out of the hole. All debris was then cleared from the hole with compress air, the bit was lubricated with cutting oil, and the process repeated for the length of the drill bit. The bit was then replaced with a 30 cm long bit, and the process continued. Finally, a 45 cm bit was used to extend the bore hole to the middle of the rod. A total of five manifolds were successfully bored in this manner during this experiment.

Once the manifolds were bored out, a series of equally spaced holes were drilled into the manifold to accommodate the aluminum tubes. For the Model ALM1, 62 holes were manually drilled using a jig to equally space the holes. Although successful, this was a very laborious and inaccurate method. For subsequent models, a computerized milling machine was used. The milling machine enabled the holes to be drilled much closer together, which increased the number of tubes used in later models. It also ensured the holes were perpendicular to the long axis of the manifold. Prior to drilling the holes on the mill, a flat

surface approximately 0.5 cm wide was milled into the round tube. This flat surface prevented the drill bit from wandering across the round face of the rod and further improved the precision of the process. The last step in fabricating the manifold was to enlarge the hole through the rod at each end to a depth of 2 cm to accommodate Swageloc™ fittings. The associated plumbing that brought the water into and out of the vacuum chamber was connected to these fittings.

After the manifolds were fabricated, the apparatus was assembled. Creating a leak-tight joint between aluminum components is, in general, a difficult task. It's commonly known that aluminum is very difficult to solder. Soldering the joints together was investigated, though, to determine if it could be done reliably and repetitively. After consulting many local welding, plumbing and metal supply companies, it became clear that soldering aluminum was far too difficult to be relied upon for so many joints. Therefore, the joints between the aluminum tubes and the manifolds were sealed using a special epoxy manufactured by Varian Vacuum Technologies.

Named Torr Seal™, it's a sealant designed specifically for high vacuum applications and is a two-part epoxy comprised of a resin base and hardener. The two components come in separate tubes and are mixed together to form the sealing compound. After preparing this sealant for the Model ALM1 apparatus, the epoxy was heated with a heat gun set to approximately 200° C. The heating served two purposes. First, when warmed the epoxy became much thinner in consistency. This aided in spreading and filling the voids of each joint. This consistency did not last long, however, so several small batches were made during the assembly process. Second, the Torr Seal™ hardens much faster after its been heated, enabling the apparatus to be assembled more quickly.

Before preparing the epoxy, a manifold was secured in a vice with the series of holes in its side facing up. A wooden dowel was then placed in the bore of the manifold to support the tubes as they were inserted into their respective hole. The dowel also assured that the tubes were not placed too far into their holes, thereby restricting the water flow through the manifold. Once the epoxy was mixed and heated, it was spread thinly over one end of a tube. The tube was then inserted into an appropriate hole, then rotated, slightly withdrawn and reinserted until it rested on the wooden dowel. The process served to distribute the epoxy through the joint and was found to create the best possible seal. In this manner, each tube was individually glued into place in one manifold as shown in figure 3.7. The Torr Seal™ was then allowed to fully harden before completing the assembly.

In order to complete the assembly of the second manifold, a wooden frame was used to secure the manifolds at the exact distance they needed to be from one another once assembled. Having been flattened, the ribbon-like tubes were very flexible. Once the remaining free end of an individual tube was coated in Torr Seal™, the tube was easily bowed and its end inserted into the second manifold. Since the opposite end of each tube was already glued into the first manifold, the tubes could not be rotated in order to distribute the epoxy. If needed, a cotton swab was used to distribute the Torr Seal™ around each joint to form a thick meniscus of epoxy. Once all tubes were glued into the two manifolds, the Swageloc™ fittings were sealed in place with Torr Seal™ in a manner similar to that described for the tubes. After the Torr Seal™ had cured for 24 hours, the Model ALM1 apparatus was placed under vacuum to check the integrity of the joints. Not unexpectedly, some joints did have leaks. Pressurizing the system and placing it underwater exposed these immediately; the leaks were easily spotted by the trail of bubbles emanating from them. The

leaks were patched with additional Torr Seal™. Prior to placing the Torr Seal™ on the leaking joint, the ALM1 apparatus was placed under vacuum so that the epoxy would be drawn into the leak and form a better patch. This method worked very well to patch all leaks. The completely assembled Model ALM1 apparatus is shown in figure 3.8.

While the Model ALM1 apparatus was under construction, the associated plumbing to support the apparatus was installed on the chamber. Since this plumbing only served to carry the water to the ALM1 apparatus and did not play a role in isotope production (did not need to allow protons to penetrate), it could be made from any material. Two lengths of copper tubing were used to transport the water in and out of the IEC chamber. This was done by inserting the copper tube through Swageloc™ fittings threaded into holes of a plate on the bottom of the chamber as shown in figure 3.9. The Swageloc™ fittings created an airtight seal around the copper tubes through the use of ferrules. The exterior ends of the two copper tubes were capped with valves as shown in figure 3.10. Swageloc™ fittings were placed on the interior ends of the two copper tubes; these fittings would join with those cemented into the manifolds, thereby connecting the Model ALM1 apparatus inside the chamber to the outside environment. Figure 3.11 shows the Model ALM1 apparatus installed in the UW IEC chamber.

As it turns out, the Model ALM1 apparatus developed numerous leaks and could not be made to work. The best operating conditions achieved were 90 kV and 30 mA. Initially, the leaks developed at the joints that were cemented with Torr Seal™. These leaks developed after only a few conditioning runs in the chamber. The water leak was detected by a significant peak on the residual gas analyzer (RGA) at an atomic weight of 18. The apparatus was immediately removed and its interior dried. It was then pressurized to locate

the leaks (there was no visible evidence of the leaks), then placed under vacuum to patch the leaks with Torr Seal™. This process repeated itself until the radiator could be proven to be leak-tight under vacuum and under pressure. The apparatus was then placed back in the chamber and a series of conditions runs with the IEC were conducted. Invariably, more leaks would develop and the repair process would begin again. During the conditioning runs, the water within the apparatus would approach 60° C as measured with a thermocouple attached to the copper tube carrying water out of the chamber. It was assumed that these leaks developed due to differences in thermal expansion between the aluminum and the epoxy. To prevent this from happening, the joints were thermally stressed by heating the aluminum manifold to 100° C. This did create more leaks, which were then patched. This process was repeated until the heating did not cause additional leaks. The apparatus was then placed into the IEC.

During the conditioning runs following the reinstallation of the Model ALM1 apparatus, there was an occasion to operate at high chamber pressure (> 6 mtorr). Water had not yet been introduced into the isotope production system, but it was filled with air at atmospheric pressure. It's not uncommon for electron jets – concentrated beams of electrons emitted from the cathode – to be observed in the chamber during high-pressure runs. These jets were known to crack the protective glass coverings of the observation ports and even to melt the stainless steel wires of the anode. Their destructive power became all too apparent, though, when a jet was incident upon the ALM1 apparatus during the high pressure run.

After only a few minutes of operation, an enormous air leaked developed within the chamber. After shutting down the experiment, a visual inspection of the ALM1 apparatus

from an observation port indicated a hole had been burned through a tube in the apparatus. The apparatus was removed from the chamber and the full extent of the damage was clear. As shown in figure 3.12, an electron jet burned holes in two tubes adjacent to each other, and heated a third tube to such an extent that it was permanently warped from the heat. These tubes were quickly replaced and the chamber was never again operated at high pressure with the water containment apparatus inside.

Shortly after the ALM1 apparatus was repaired and installed, a series of conditioning runs were conducted to determine if the chamber could successfully operate at high voltages with the ALM1 inside. Unfortunately, the apparatus developed leaks almost immediately. But unlike before, these leaks occurred near the edges of the flattened aluminum tubes and not in the joints. It's thought that these leaks were caused by stress fractures induced during the tube-flattening processes. It's unclear, however, why these leaks did not express themselves immediately during the initial leak checks or the previous operational runs.

The leaks on the aluminum tubes were patched using Torr Seal™ in a manner similar to sealing the joints. When the epoxy was hardened, these areas were wrapped in aluminum to minimize any interaction between the epoxy and the plasma. Once proven leak-tight under vacuum using sensitive vacuum gauges and even a helium leak checker, the ALM1 apparatus was placed back into the chamber for a final round of operational tests. After only a few runs, however, the ALM1 apparatus developed more leaks near the edges of the flattened aluminum tubes. It was concluded that these “stress” leaks would continue to develop and that a new apparatus would need to be constructed to resolve the problem.

Section 3.4 The Model ALM2 Water Containment Apparatus

The second series of leaks in the Model ALM1 apparatus all developed at the edge of the aluminum tubes and not in the joints; therefore, it was believed that another water containment apparatus could be constructed from round (not flattened) aluminum tubes using Torr Seal™ by thermally stressing the joints.

If the Model ALM1 apparatus could be described as a one panel assembly, then the Model ALM2 apparatus was a two panel assembly. As shown in figure 3.13, it consisted of two rows of aluminum tubes mounted perpendicularly to each other in one central manifold, and two other manifolds mounted on each of the two sets of tubes. This L-shaped assembly was designed to be placed inside the IEC chamber with one panel in the horizontal plane below the anode, and the other panel vertically situated between the anode and the chamber wall. The angle between the two panels was actually slightly more than 90 degrees so that water would drain to the outer end of the horizontal panel when the vertical panel was placed at 90 degrees to the chamber floor.

The tubes and manifolds used in the Model ALM2 apparatus were constructed from the same materials and in the same manner as the ALM1. The joints were sealed with heated Torr Seal™ as before, and the round tubes were bowed in order to insert them into the manifolds just as the flattened tubes were. Although the round tubes were not nearly as flexible as the flattened tubes, they did have enough give to enable them to be bowed and inserted between two manifolds that were fixed in place by a wooden frame. The Swageloc™ fittings were placed in one corner of the vertical panel and in the opposite corner of the horizontal panel to promote an equal distribution of water flow through all tubes.

When the ALM2 was fully assembled and the epoxy fully cured, the manifolds were heated to 100° C to thermally stress the epoxy joints. This created numerous leaks in the joints, but these were easily found and patched. The heating and patching process continued until no additional leaks were detected. The apparatus was then mounted inside the IEC chamber, connected to the copper plumbing, and the system filled with water.

After only a few conditioning runs, the ALM2 apparatus developed leaks. After the apparatus was removed from the IEC chamber, it was determined that the epoxy joints were leaking. The ALM2 was placed under vacuum and the joints were patched with heated Torr Seal™. The apparatus was thermally stressed and more leaks were found. This process continued until the ALM2 was proven leak-tight. It was then placed back into the chamber for another operational test. Unfortunately, the system again developed leaks after only a few runs at 80 kV and 30 mA. It seemed as if there were more to the failure of the epoxy joints than just differences in thermal expansion. Although there was no evidence to indicate the specific cause of the leaks, it was assumed that the plasma somehow contributed to the failures and that this problem would not be overcome. Therefore, the Model ALM2 was retired and a new, more robust system was designed.

Section 3.5 Stainless Steel Water Containment Apparatus

The experience with the ALM1 and ALM2 apparatus demonstrate that the joints of any water containment apparatus need to be as rugged as the tubes themselves. This seemed to necessitate soldering the joints between the tubes and the manifolds. Aluminum was determined to be far too difficult to solder successfully, so another tube material would need to be substituted for aluminum. Copper and brass are very easy to solder and, therefore, were the first metals investigated. Due to its innumerable uses, copper tubing is fabricated

by more manufacturers and in a much wider selection of styles than brass tubing. Consequently, all effort was soon concentrated on finding appropriate copper tubing for this task. As previously detailed in table 3.1, copper tubes need to have a wall thickness of approximately 0.012 cm in order to allow a 14.7 MeV proton to retain 12.5 MeV of energy after passing through it. Several suppliers and manufacturers were contacted in an attempt to locate such thin tubing. They each provided the same negative response. Because it is so soft, a 0.012 cm thick walled copper tube would be very fragile and not commercially practical as a tubing product. Hence, copper and brass tubes were rejected as viable alternatives to aluminum.

Because of its strength and high melting point, stainless steel was chosen as the next water containment material. However, the characteristics that make stainless steel corrosion resistant also make it very difficult to solder. Special fluxes and solder must be used to overcome this obstacle. For all stainless steel soldering in this experiment, the flux used was # 71 flux from the Superior Flux and Mfg. Co. This flux contains a combination of zinc chloride, hydrochloric acid and ammonium chloride. The solder used was a “silver” solder, consisting of approximately 96.5% tin and 3.5% silver. Both of these materials were purchased from a local distributor called Acro Sales and Engineering, Inc., located in Menomonee Falls, Wisconsin.

The next step was to find and purchase appropriate stainless steel tubes. The McMaster-Carr Supply Company offered type 304 stainless steel tubes with a 0.64 cm diameter and 0.013 cm thick wall in 71 cm lengths. Although much more expensive than the aluminum tubes, these stainless steel tubes seemed ideally suited for this experiment, so five tubes were purchased for solder testing purposes. If these tubes were successfully

soldered to a stainless steel manifold, then a new water containment apparatus would be constructed from them.

The five stainless steel tubes were each manually cut into four equal lengths using a small tube cutter. This was much more difficult than anticipated, and it quickly became apparent that a more robust mechanical method would be needed to cut the large number of tubes required for a water containment apparatus. A small length of stainless steel tube 1.91 cm in diameter with a wall thickness of 0.32 cm was used to simulate the manifold. Ten 0.64 cm diameter holes were drilled into this tube approximately 0.5 cm apart. Flux was liberally applied to each hole and to one end of several tubes. Each tube was then inserted into a hole, and a small oxy-acetylene torch was used to heat the manifold. The thin-walled tubing heated very quickly and great care had to be taken not to burn a hole through them. The torch flame was directed at the manifold approximately one centimeter from the joint. When hot enough, solder was applied to the joints. Because of the poor conductivity of the stainless steel, the area around each joint had to be heated independently. Moreover, both sides of the manifold tube had to be heated. All the while, flux was constantly applied to the joint to ensure the solder bonded to the stainless steel. This process became a juggling act and it was very difficult to solder the ten tubes, although it was done successfully.

To simplify the soldering process and better control the manifold temperature, an electrical circuit was employed to heat a second test manifold much like the burner of an electric stove. A large, 220 volt variable step-down transformer was used to induce a current in a heavy copper wire attached to each end of the manifold as shown in figure 3.14. This 4/0 gauge wire was looped through the transformer five times. Solid copper clamps located at the ends of the wire attached to the manifold much like the terminals of a car

battery. When powered, the transformer could be adjusted to control the current through, and therefore the temperature of, the stainless steel manifold. The resistance of the stainless steel caused the manifold to quickly heat to temperatures in excess of 230° C, the melting point of the solder. This technique worked very well and was quite simple. The only drawback was the enormous cloud of corrosive steam created as the liberally applied flux began to boil. A tremendous amount of ventilation was needed to control this. Moreover, a mask, rubber gloves and goggles (not just protective glasses) were needed to prevent the steam from irritating the nose, throat, hands and eyes.

Once a method was developed and successfully tested to solder together a stainless steel apparatus, the materials necessary to build the Model SSM1 were obtained. Located in the glass shop of the UW physics department, a table saw with corundum blade was used to cut the 70 tubes necessary for the SSM1 design. This was a very fast and efficient process. A jig ensured each tube was cut to the specified length with millimeter accuracy. Once cut, the tubes were cleaned in the same four-step manner as the aluminum tubes. The two stainless steel manifolds did not need to be bored out like the aluminum manifolds, since they were fabricated from tubing and not bar stock. The computerized milling machine was used to drill the 70 holes along the length of the tube as previously discussed. These were drilled using a ¼ inch titanium nitride-tipped drill bit. The ¼ inch nominal diameter tubes fit snugly into these holes – so snugly, in fact, that when dry-assembled it was rather difficult to take it apart.

Immediately prior to assembly, each hole in the manifolds and each end of the tubes were coated with flux. The Model SSM1 apparatus was then pieced together entirely and the inductive heating circuit was connected to one manifold. The joints were brushed with

flux one last time as the transformer began heating the manifold. The ends of the manifold heated the fastest and reached the highest temperature. When the temperature at the center of the manifold was hot enough to melt the solder, the transformer was shut off and the solder wire was run along the manifold across the joints at a quick and steady pace. Only two passes were made with the solder; it was run up one side of the joints and down the other. The manifold was visually examined to locate any joints that did not have a meniscus of solder around the base of its tube. The solder was quickly touched to those areas, and then the manifold was misted with water to cool it below 230° C and lock the tubes in place. The copper electrodes were then removed from one manifold and connected to the other. The same soldering process was employed, and in a matter of minutes all 140 joints were soldered.

The boiling flux left a thick, tar-like residue on both the inside and outside of the tubes. This had to be removed in order to minimize the ions released into the water that would eventually circulate through the apparatus. Before the Swageloc™ fittings were soldered to the manifolds, the inside and outside of the Model SSM1 was thoroughly rinsed with an industrial toilet bowl cleaner called Solvit™, which contains 24% hydrochloric acid. This cleaner quickly removed the residue from the outside of the apparatus, and it appeared to remove it from the inside as well. Immediately after flushing the bowl cleaner from the apparatus, it was rinsed repeatedly with hot soapy water. It was then rinsed with hot water, then acetone and finally alcohol.

After this thorough cleaning, the Swageloc™ fittings were soldered into both ends of each manifold. This was a slight difference from the Model ALM1 and ALM2 apparatus. It was done to provide more flexibility for the associated plumbing, and to allow the SSM1 to

be connected in series at a later date with similar, additional apparatus if need be. With the fittings in place, the SSM1 was put under vacuum to test the integrity of the soldered joints. Surprisingly, this test indicated that many of the tubes themselves each contained numerous pinholes. After speaking with both the manufacturer and the supplier, it was learned that this batch of tubes had been improperly manufactured. The manufacturer agreed to immediately fabricate a new batch of tubes for the experiment.

When the new batch of tubes arrived, they were checked for leaks using a helium leak checker. No tube from this batch contained a leak. Hence, the Model SSM2 apparatus was immediately constructed. The cutting, cleaning, soldering and leak checking methods used for the SSM2 were identical to those described for the SSM1. When the SSM2 was fully assembled and checked for leaks, a few leaks were found in the soldered joints. These joints were heated with two heat guns from opposing angles and soaked with flux. After a few minutes of heating by the guns, the area around the joint was hot enough to melt the solder. The liquid solder was then teased around the joint with a length of stainless steel wire. This helped ensure a complete meniscus around the tube joint. Unlike patching leaks in the Models ALM1 and ALM2 apparatus, the SSM2 was not placed under vacuum when patching its leaks with solder. This is because the molten solder is much more viscous than the Torr Seal™, and would be drawn completely through the hole without patching it. Figures 3.15 contain a picture of the fully assembled SSM2 apparatus.

The SSM2 water containment apparatus proved to be a very rugged and successful design. The IEC was operated at potentials reaching 155 kV, and at lower voltages with currents of 60 mA, with the apparatus inside. It developed only one minor leak during its operational lifetime, and that was easily repaired.

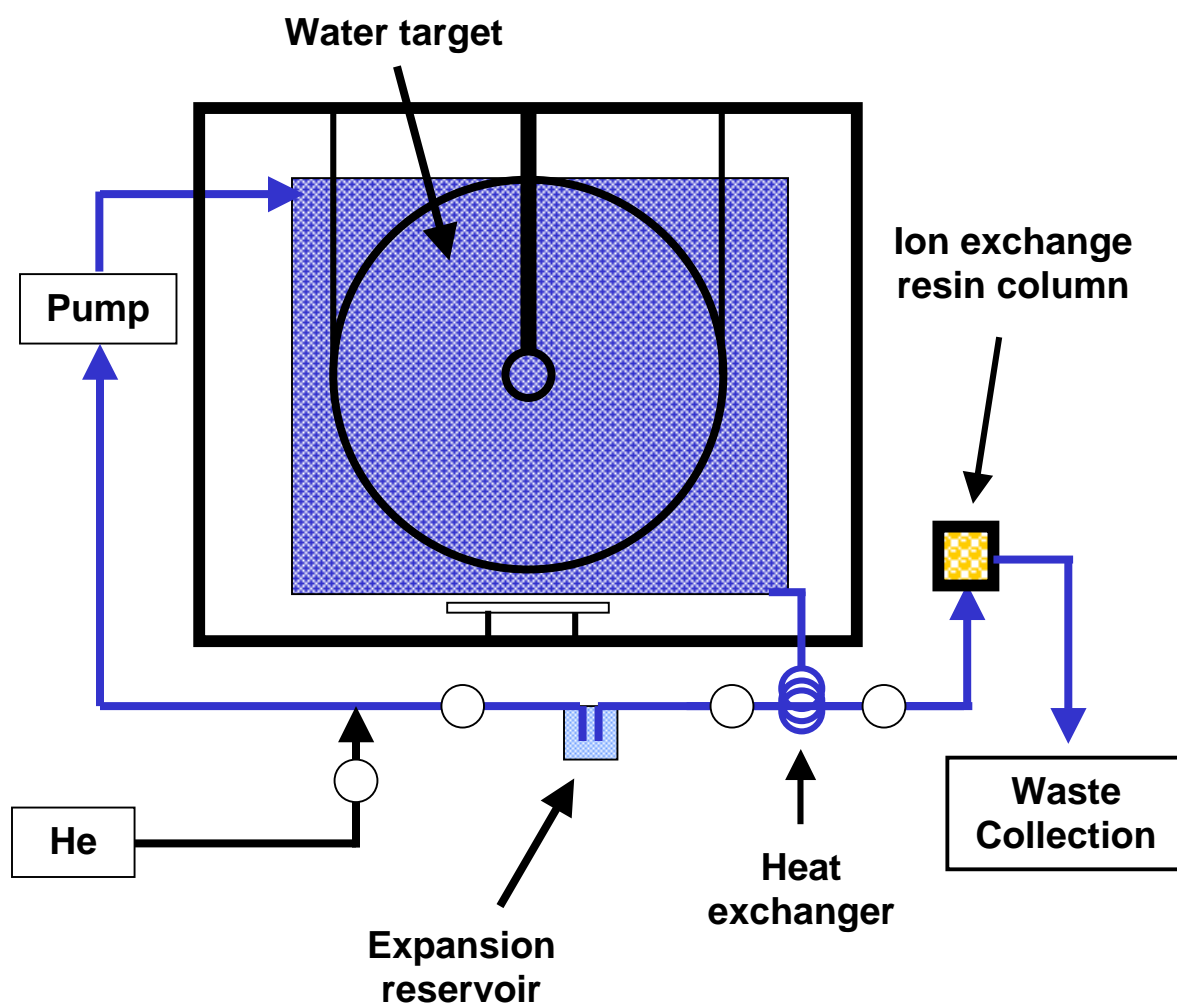


Figure 3.1 – Schematic diagram of isotope production system. A volume of water is continually circulated through a containment apparatus inside the IEC chamber. Because the chamber generates more than 4 kW of power during a radioisotope production run, a heat exchanger is needed to remove the heat from the water to prevent steam production. The water then flows into a water expansion reservoir, enabling it to increase in volume as its temperature increases. To empty the system, it is pressurized with 50 psi of helium. A series of valves is opened and closed, allowing the helium to pressurize the system and directing the water into the ion exchange resin column that captures the ^{13}N .

Proton Energy vs. Range in Aluminum, Stainless Steel & Water

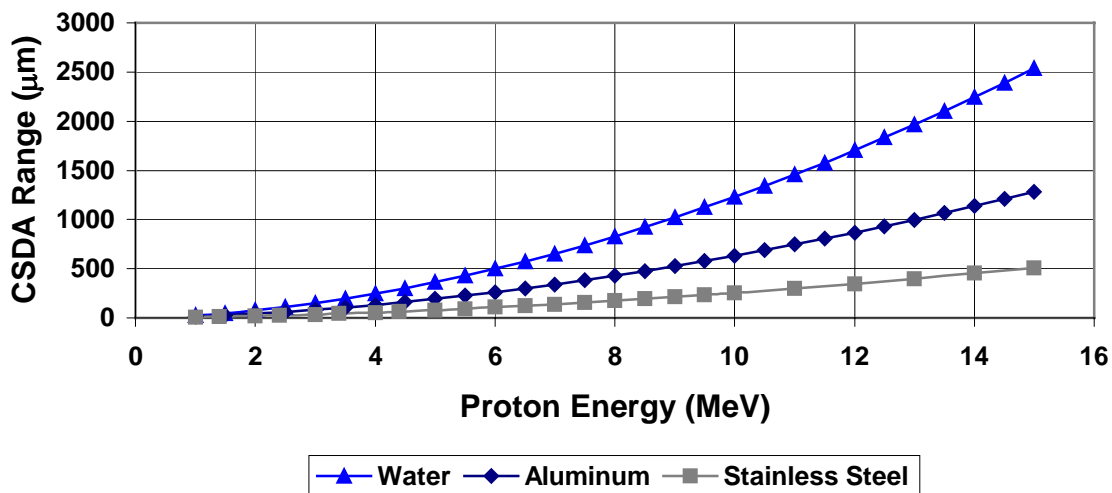


Figure 3.2 – Graph of CSDA range vs. proton energy in three materials. The range of protons in copper is very similar to their range in stainless steel. As this graph shows, protons have more than twice the range in aluminum than in stainless steel. This means that an aluminum tube could have more than twice the wall thickness of a stainless steel (or copper) tube for a given proton energy loss in the tube wall.

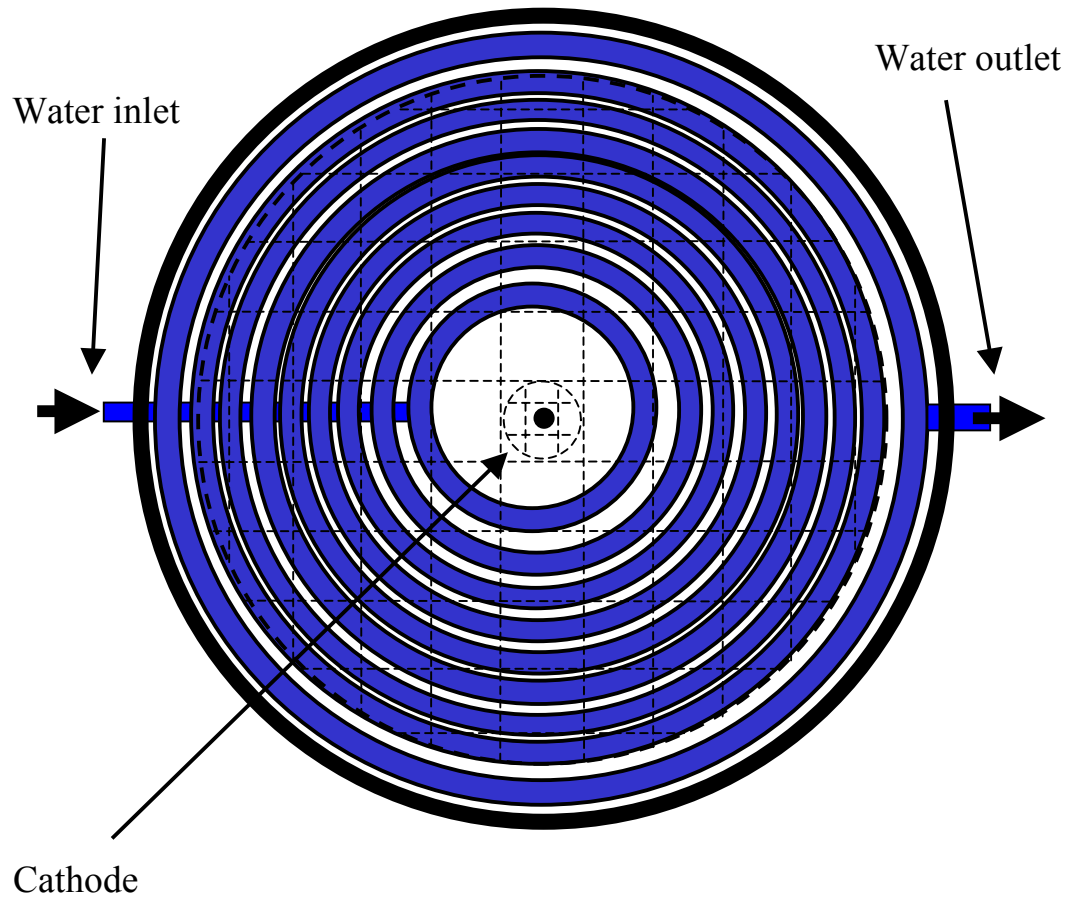


Figure 3.3 – Schematic diagram of spiraling coil design for water containment apparatus. This is a top view of the UW IEC chamber. The spiral target would rest on the bottom of the chamber. Water would flow in one end of the spiral and out the other. This design was rejected, however, since no coiled tubing could be found with walls thin enough to meet our requirements.

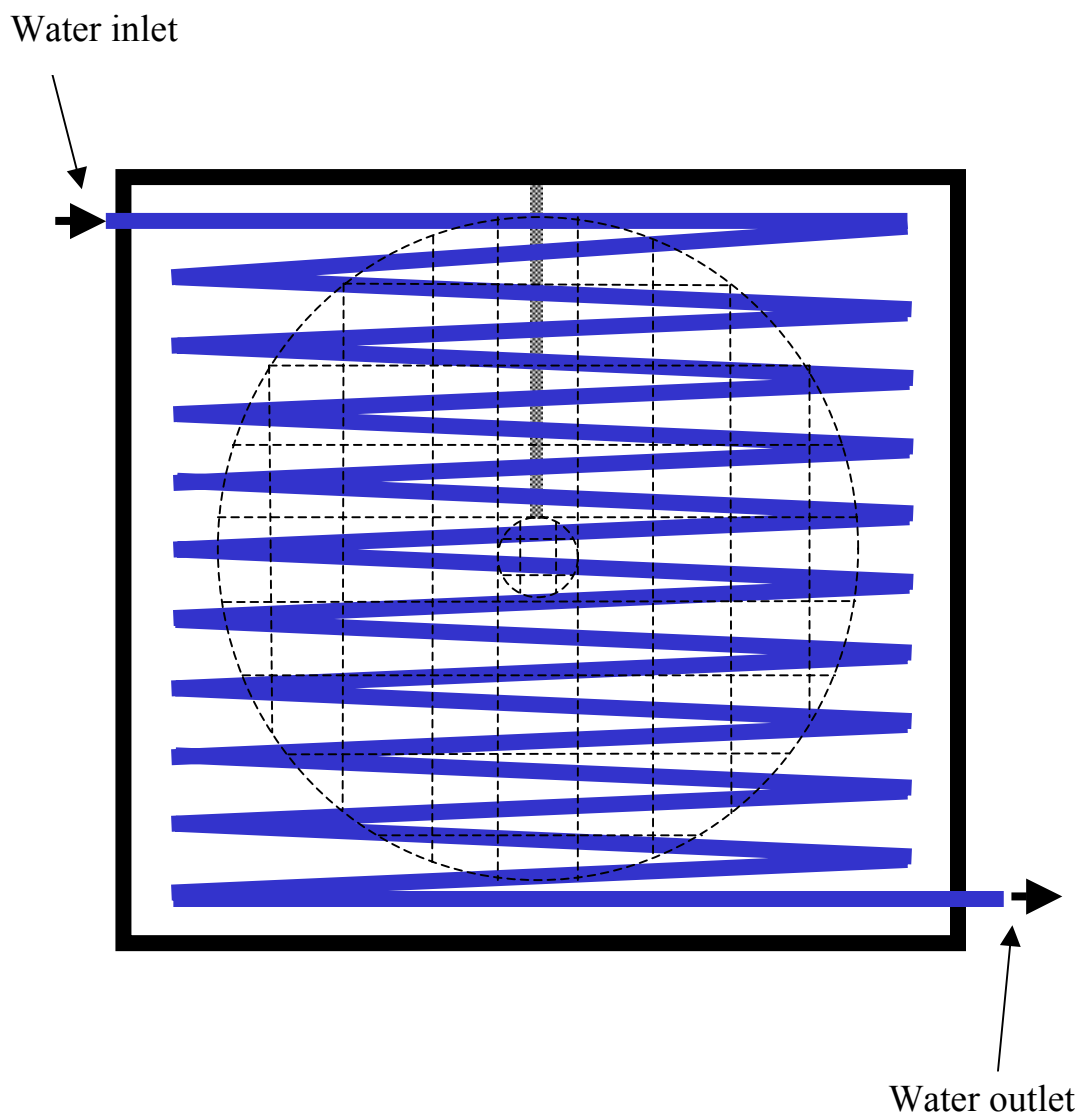


Figure 3.4 – Schematic diagram of coiled water containment apparatus that would line the vertical inner walls of the UW IEC chamber. In reality, the coils would lie tightly together and not spaced apart as in the diagram. It was believed that such a coil could be manipulated to create openings for the proton detector, window, etc. This design was also rejected because no coiled tubing with thin enough walls could be obtained.

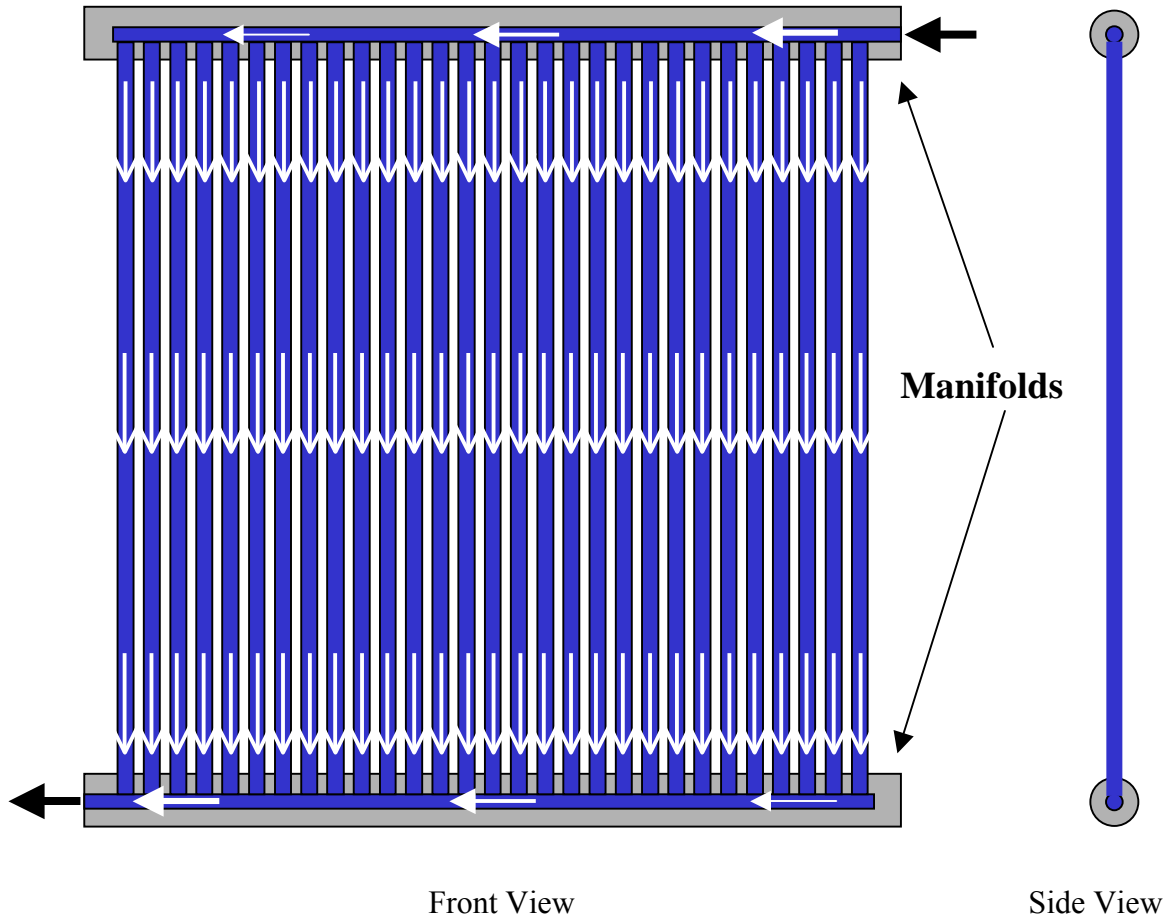


Figure 3.5 – The “radiator” design incorporating approximately 65 vertical tubes closely aligned alongside each other. A manifold at either end enabled water to be distributed through and collected from each tube.

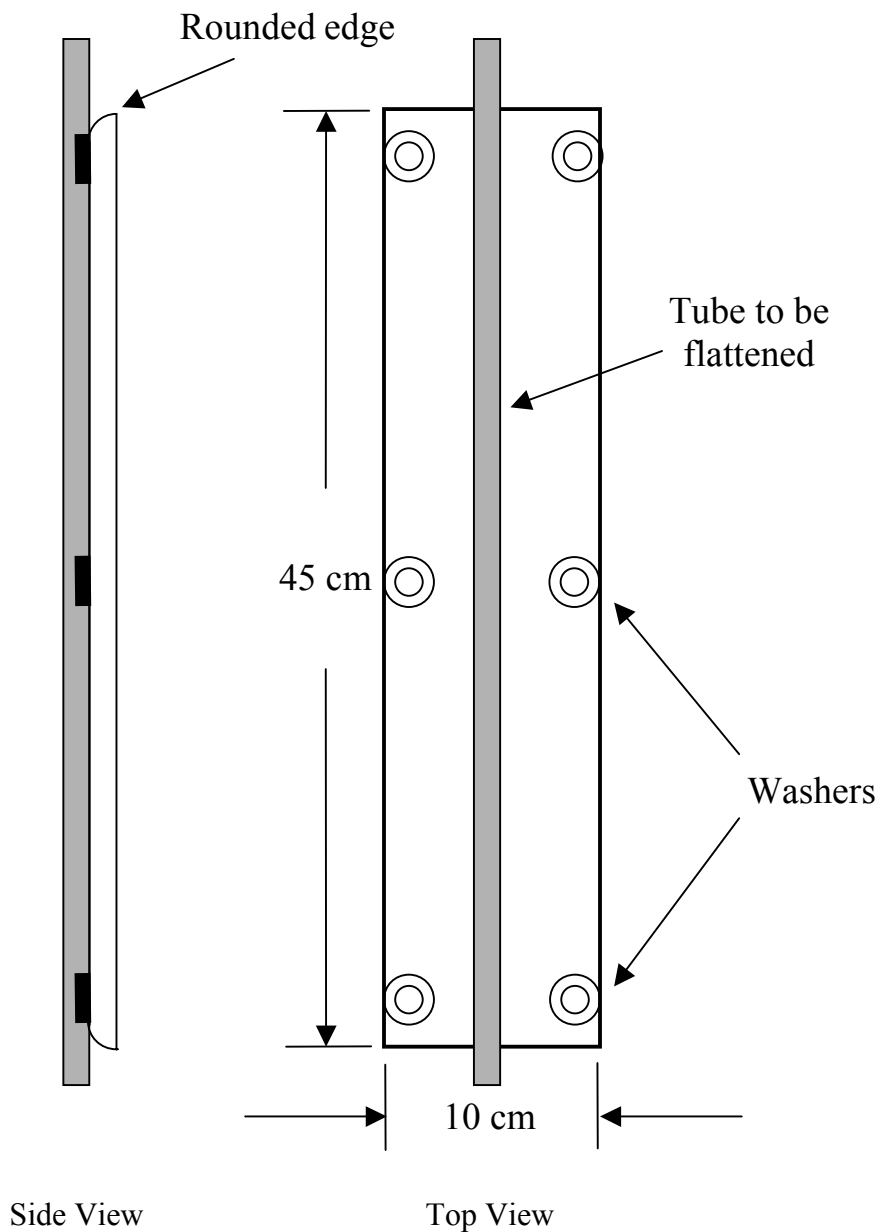


Figure 3.6 – Schematic diagram of one bar used to flatten the central portion of the aluminum tubes in the Model ALM1 apparatus. A tube was placed on this bar, and a press was used to force an identical bar down on top of it. This flattened the aluminum tube between the bars to a thickness of approximately 0.4 cm. The washers glued to one bar prevented the tube from being completely flattened.

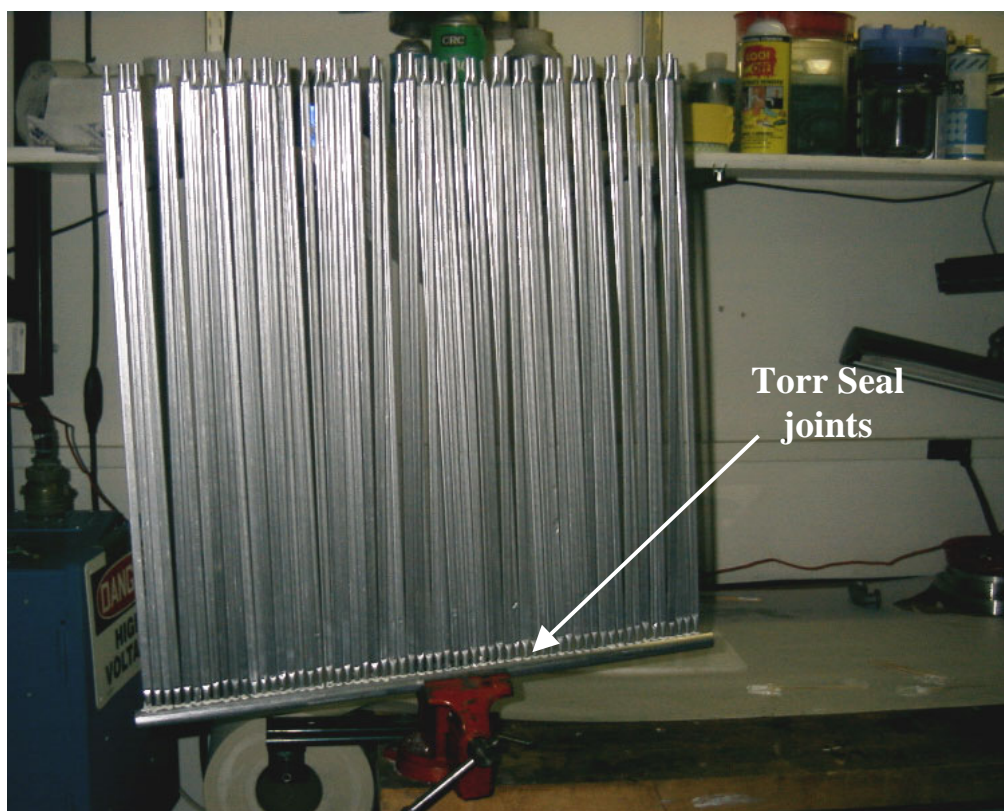


Figure 3.7 – Model ALM1 apparatus under construction. The joints between the flattened tubes and the manifold were sealed using Torr Seal™, an epoxy by Varian Vacuum Technologies designed specifically for high vacuum environments.



Figure 3.8 – Picture of the Model ALM1 water containment apparatus. Note that the vertical tubes have been flattened to present a constant wall thickness to incoming protons.



Figure 3.9 – Photograph of plate through which the copper plumbing of the isotope production system passes. The copper tubes are fed through Swageloc™ fittings, which are screwed into the plate and their threads sealed with Torr Seal™. The fittings fix the copper tubes in place and provide a leak-tight seal.

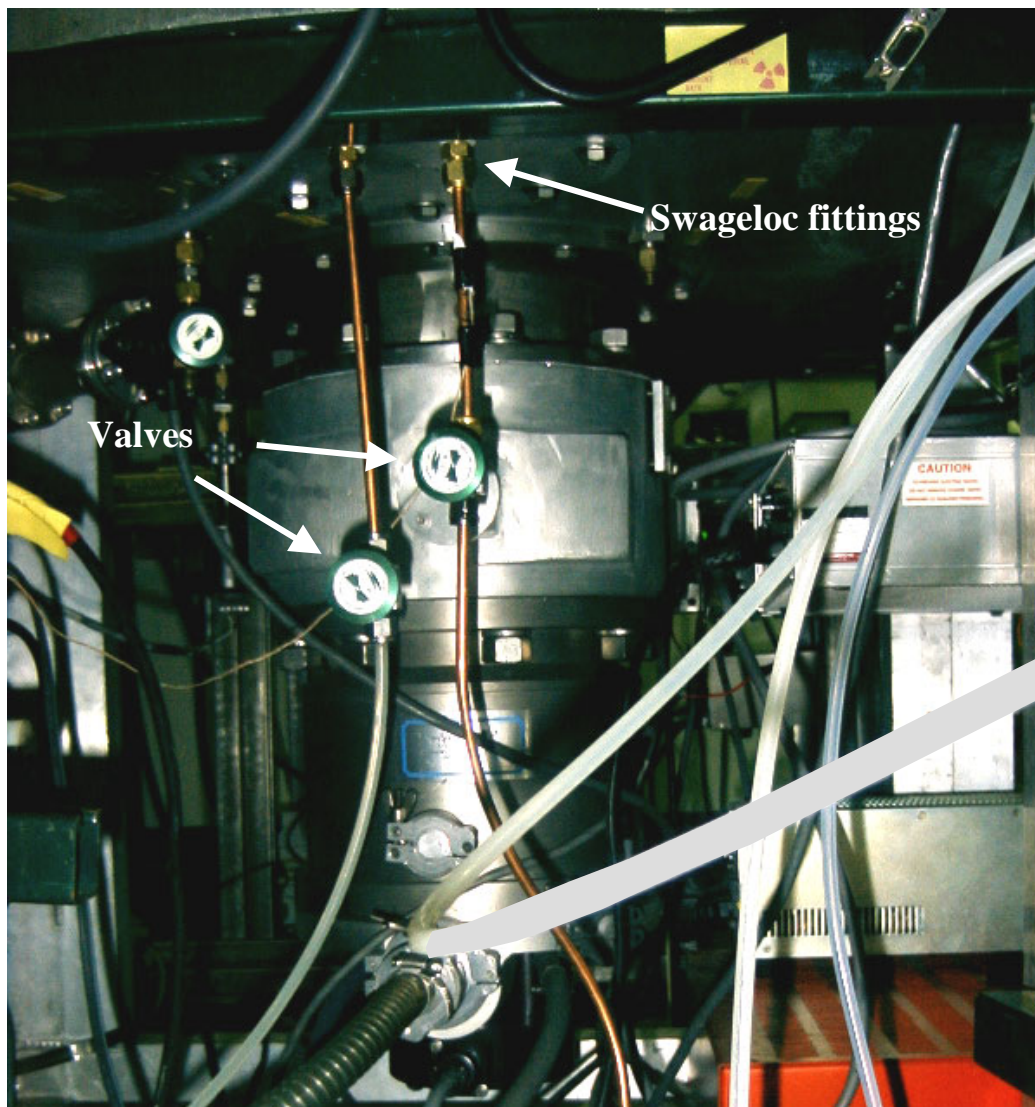


Figure 3.10 – Exterior view of copper plumbing exiting the chamber through Swageloc™ fittings. The ends of the tubes are capped with a valve that controls the flow in and out of the water containment apparatus.

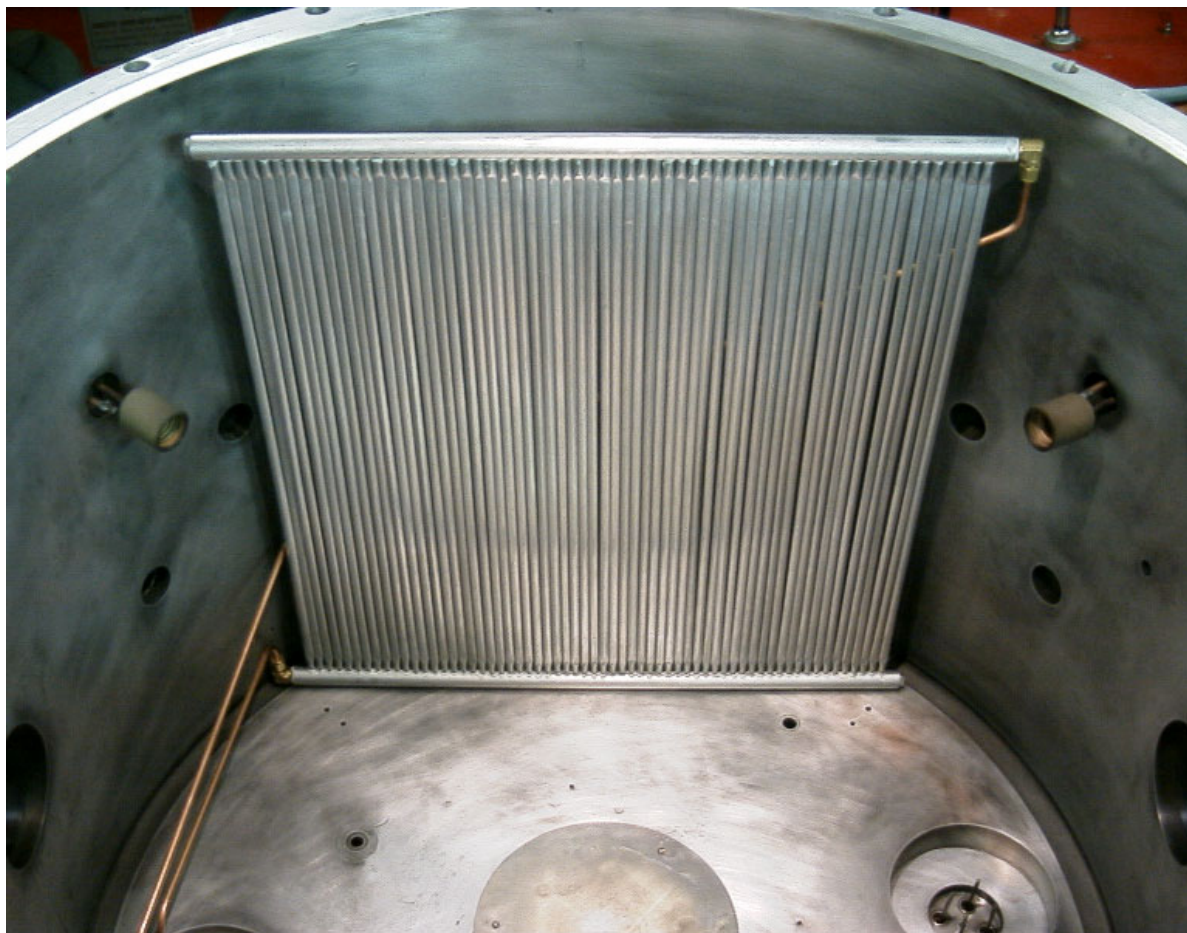


Figure 3.11 – The Model ALM1 apparatus mounted in the UW IEC chamber. In this location, the vertical face of the apparatus was approximately 8 cm outside the anode.

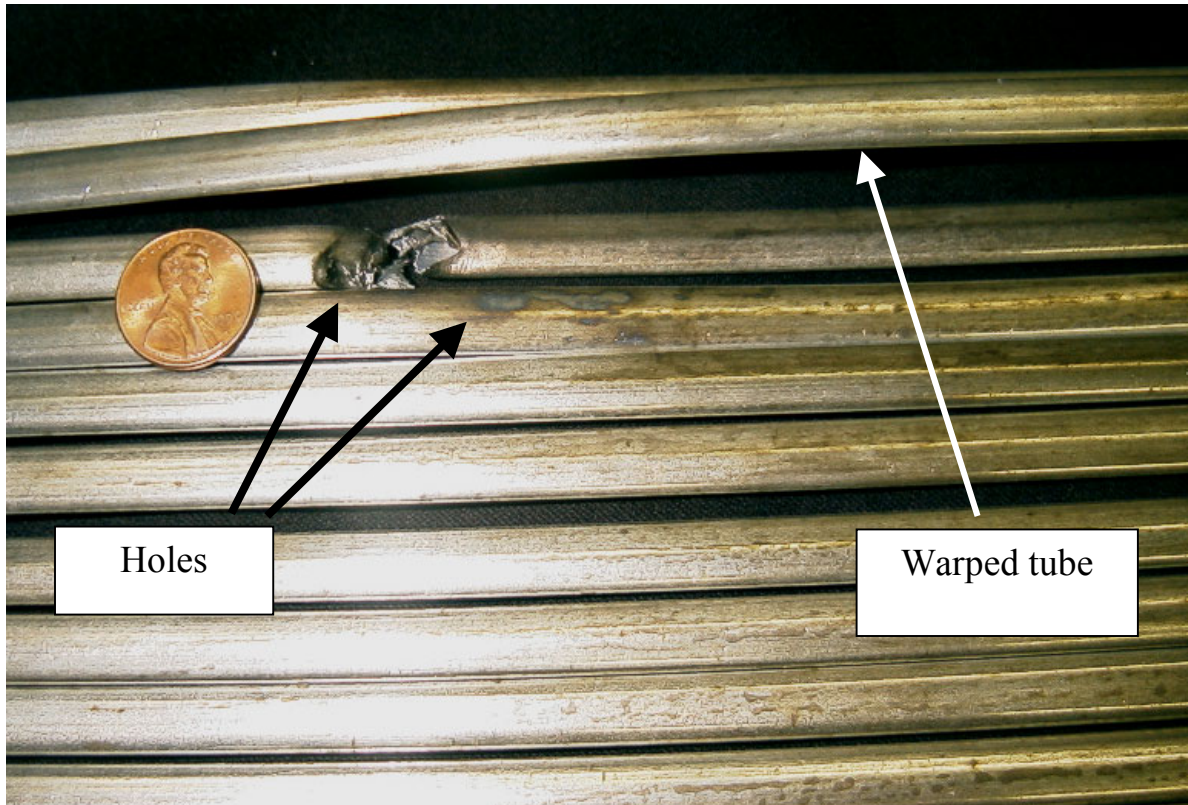


Figure 3.12 – During a high pressure run (> 6 mtorr), electron jets damaged the Model ALM1 apparatus. One tube was nearly severed, and several small holes were created to an adjacent tube. The other adjacent tube became so hot that it was permanently warped. It is not known why this tube became so hot, or why it did not contain any holes. After this event, the IEC was never operated at high pressure with the water containment apparatus inside.



Figure 3.13 – The Model ALM2 apparatus. This L-shaped apparatus was designed to have the horizontal panel fit below the anode, and the vertical panel fit between the anode and the IEC chamber wall. Numerous leaks developed in the joints of this apparatus, however, and it was retired after only a few weeks of testing.

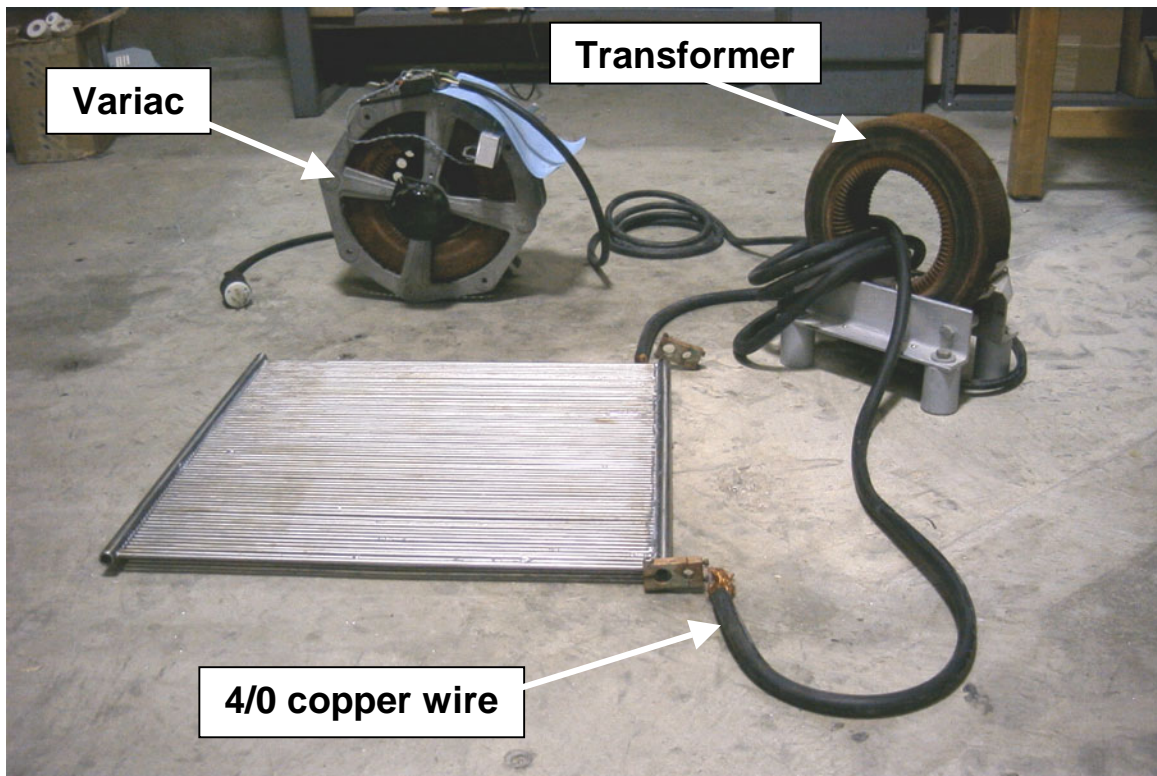


Figure 3.14 – The inductive heating circuit used to solder the Models SSM1 and SSM2 apparatus together. The variac controlled the voltage to the transformer, which induced a current in the coils of 4/0 copper wire looped through it. This current traveled through the highly resistive stainless steel manifold, causing it to quickly reach temperatures above the 230° C melting point of the solder.



Figure 3.15 – The Model SSM2 water containment apparatus. This model was constructed entirely from stainless steel and used tubes with 0.013 cm thick walls. The tubes were soldered to the manifold creating a rugged, high temperature joint.

Chapter 4 Theory of ^{13}N Activation in UW IEC

Section 4.1 Theory of Radioisotope Production in a Pure Thick Target

This chapter develops the equations required to predict the quantity of radioisotopes produced by a proton flux impinging upon a target. The derived expressions are then compared to experimental values and used to estimate the quantity of ^{13}N that could be produced by the IEC for specific operating conditions. This development follows that described by Dr. Hesham Khater in his doctoral thesis completed in 1990 [28]. Several assumptions are made in developing this theory.

- 1) The radioisotope is only produced by nuclear interactions between protons and the parent atoms.
- 2) The number of parent atoms is not affected by the production of the daughter radioisotope (i.e., there is no burn up of the parent atoms).
- 3) The only removal mechanism for the radioactive daughter atoms is radioactive decay (i.e., the radioactive daughter atoms are not transmuted by the protons)

For a thin target of thickness Δx containing only parent atoms, the creation of radioisotopes and their decay during production is described by a simple balance equation. For this equation, a thin target is defined to be a target of such thickness that the energy a proton would lose in passing through it is negligible:

$$\frac{dN}{dt} = \sigma n \phi \Delta x - \lambda N \quad (4.1)$$

where

N = the number of radioactive daughter atoms produced

σ (cm^2) = the parent atom's nuclear cross section for proton absorption

n (atoms/g) = the number of parent atoms per gram of target material; the unit of atoms per gram, rather than atoms per cubic centimeter, is used because the density (atoms/cm^3) of materials has the drawback of being temperature dependent.

ϕ (protons/s) = the number of protons impinging upon the target per second

Δx (g/cm^2) = the thickness of the thin target

λ (s^{-1}) = the decay constant of the radioisotope produced ($= \frac{\ln 2}{T_{1/2}}$)

Integrating the above equation yields the following expression, which predicts the number of radioactive atoms produced during an irradiation of time t in seconds:

$$N = \sigma n \phi \Delta x \left(\frac{1 - e^{-\lambda t}}{\lambda} \right) \quad (4.2)$$

Since the activity of N radioactive atoms is defined as the product of N and λ , the activity of the thin target can be rewritten as:

$$A = N\lambda = \sigma n \phi \Delta x (1 - e^{-\lambda t}) \quad (\text{dps}) \quad (4.3)$$

The activity of a thick target, defined as a target in which the proton expends all of its kinetic energy, can be found by integrating equation (4.3) over the range R_p (g/cm^2) of the proton. This leads to the following relation:

$$A = (1 - e^{-\lambda t}) n \int_0^{R_p} \sigma(x) \phi(x) dx \quad (\text{dps}) \quad (4.4)$$

where the zero in the integral represents the target's surface.

As described in Chapter 3, this experiment uses 14.7 MeV protons created from D-³He fusion reactions to irradiate a target. It is assumed these protons are emitted from a point source located in the center of the cathode. Since nuclear cross sections for protons are generally very small at energies below 40 MeV, it's assumed that the number of protons lost due to nuclear reactions within the target is negligibly small [29]. In the case of a point source of protons, it's also assumed that the source is far enough away from the target that the $1/r^2$ decrease in the flux is negligible over the range of the proton. Hence, the proton flux is constant for all depths within the target and is redefined as ϕ_o . It can then be moved outside the integral, and equation (4.4) can be rewritten as:

$$A = (1 - e^{-\lambda t}) \phi_o n \int_0^{R_p} \sigma(x) dx \quad (\text{dps}) \quad (4.5)$$

Since cross sections are published as functions of energy rather than depth, the integral in equation (4.5) is converted to an energy-dependent function by dividing the cross section by the stopping power of the parent atom, $S(E)$, in units of MeV•g/cm². The resulting integral is then evaluated over the energy range of the incident protons, where E_p (MeV) is the proton's initial energy:

$$A = (1 - e^{-\lambda t}) \phi_o n \int_0^{E_p} \frac{\sigma(E)}{S(E)} dE \quad (\text{dps}) \quad (4.6)$$

Since accelerators and cyclotrons produce essentially all of the short-lived medical radioisotopes, it's convenient to further modify equation (4.6) such that its units reflect those common to the commercial radioisotope production community. The proton beam in accelerators and cyclotrons is measured as a current I (μA). If the proton flux in the IEC is

measured as a current, and recognizing that 1 μA of proton current is equivalent to 6.25×10^{12} p/s, equation (4.6) becomes

$$A = 6.25 \times 10^{12} (1 - e^{-\lambda t}) I(\mu\text{A}) n \int_0^{E_p} \frac{\sigma(E)}{S(E)} dE \quad (\text{dps}) \quad (4.7)$$

The medical isotope community still often measures the activity of radionuclides in units of Ci or some fraction thereof, rather than the SI standard of Bq. Hence, the units of equation (4.7) are converted from Bq to mCi:

$$A = 1.689 \times 10^5 (1 - e^{-\lambda t}) I(\mu\text{A}) n \int_0^{E_p} \frac{\sigma(E)}{S(E)} dE \quad (\text{mCi}) \quad (4.8)$$

When evaluated, the integral in equation (4.8) is a constant value for a monoenergetic proton flux. Hence, the only variables affecting the activity of a target irradiated with protons of initial energy E_p is the irradiation time t and the proton current I . If the expressions containing these two variables are removed from the relation, the remaining value represents the maximum achievable activity for an infinite irradiation time per unit of incident proton current of energy E_p . This value is known as the saturated yield, Y , of the target and is given by:

$$Y = 1.689 \times 10^5 n \int_0^{E_p} \frac{\sigma(E)}{S(E)} dE \quad (\text{mCi}/\mu\text{A}) \quad (4.9)$$

Therefore, by substituting the above expression for the yield into equation (4.8), the target activity can be cleanly written as:

$$A = Y I (1 - e^{-\lambda t}) \quad (\text{mCi}) \quad (4.10)$$

Section 4.2 Modification of Production Yield for Homogeneous Mixtures

As previously stated, the above derivations apply to a target containing only parent atoms of interest. In this experiment, however, the target oxygen atoms are contained within water. Consequently, equation (4.10) must be modified to reflect the concentration of the oxygen atoms within the water target and the difference in stopping power between oxygen atoms and water molecules. This is accomplished using the equation [29]:

$$Y_w = Y_o \eta_w F \quad (4.11)$$

where

Y_w = saturated yield of water target

Y_o = saturated yield of oxygen target

η_w = weight concentration of the oxygen atoms in water

F = factor that accounts for the difference in stopping power between oxygen atoms and water molecules

For water, $\eta_w = 16/18 = 0.889$.

The factor F can be found in at least three ways [30-33]. For this experiment, it is calculated using the expression:

$$F = \frac{R_w}{R_o} \quad (4.12)$$

where

R_w (g/cm²) = range of a proton of energy E_p in water = 0.2444 g/cm² [27]

R_o (g/cm²) = range of a proton of energy E_p in oxygen = 0.2844 g/cm² [27]

Using the values of R_w and R_o listed above, F is calculated to be 0.859.

From these values of η_w and F , the saturated yield of a water target is calculated to be:

$$Y_w = (0.889) (0.859) Y_o = 0.764 Y_o \quad (\text{mCi}/\mu\text{A}) \quad (4.13)$$

The activity of a water target can then be found from this saturated yield as:

$$A = 0.764 Y_o I (1 - e^{-\lambda t}) \quad (\text{mCi}) \quad (4.14)$$

Section 4.3 Calculation of ^{13}N Yield in Water Target

In order to apply equation (4.14), the yield Y_o must be determined. Solving equation (4.9) for protons of a specific initial energy accomplishes this. As mentioned in Chapter 3, the energy of the 14.7 MeV protons from $\text{D}-^3\text{He}$ reactions is reduced by approximately 2.2 MeV as they pass through the 0.013 cm wall of the stainless steel tubing en-route to the water inside. Hence, their initial energy upon entering the water is considered to be 12.5 MeV. For this initial proton energy, the cross sections [1] and stopping powers [27] are obtained at 0.1 MeV intervals over the energy range in which the cross section has a non-zero value (5.8 MeV – 12.5 MeV). These values are listed in table 4.1 at the end of this chapter. The value of the integral in equation (4.9) is then approximated using the Midpoint Rule [34]:

$$\int_a^b f(E) dE \approx \sum_1^n f(\bar{E}_i) \Delta E \quad (4.15)$$

where

$$\Delta E = \frac{b-a}{n}$$

$$E_i = \frac{1}{2} (E_{i-1} + E_i) = \text{midpoint of } [E_{i-1}, E_i]$$

For this calculation,

$$a = 5.8 \text{ MeV}$$

$$b = 12.5 \text{ MeV}$$

$$n = 67$$

$$\Delta E = 0.1 \text{ MeV}$$

$$\sum_1^n f(\bar{E}_i) = \sum_{5.8\text{MeV}}^{12.5\text{MeV}} \frac{\sigma(E)}{S(E)}$$

Using equation (4.15), and the cross section and stopping power values in Table 4.1, the integral in equation (4.9) is approximated to be:

$$\int_{5.8\text{MeV}}^{12.5\text{MeV}} \frac{\sigma(E)}{S(E)} dE \approx 3.696 \times 10^{-27} \quad (\text{g}) \quad (4.16)$$

Additionally, the concentration of oxygen atoms is calculated to be 3.7625×10^{22} atoms/g.

Using these two values in equation (4.9), Y_o is determined to be:

$$Y_o = 23.5 \quad (\text{mCi}/\mu\text{A}) \quad (4.17)$$

This value is within 0.4% of the 23.6 mCi/ μ A listed for 12.5 MeV protons on the IAEA's online charged particle cross section database for medical radioisotope production [1].

Hence, the derived method will be used as the basis for all yield calculations.

Using the saturated yield shown in equation (4.17), Y_w is then found to be:

$$Y_w = (0.764) Y_o = 18.0 \quad (\text{mCi}/\mu\text{A}) \quad (4.18)$$

This value is inserted into equation (4.10) to determine the activity of ^{13}N produced in a water target during an irradiation time t by a proton current I .

Section 4.4 Determination of Systematic Efficiencies

As described in Chapter 3, the isotope production system is a closed loop of water that passes in and out of the IEC chamber. The water is irradiated as it flows through

numerous round, stainless steel tubes vertically aligned within the chamber. When irradiation is complete, the water is removed from this system and passed through an ion exchange resin that traps the $^{13}\text{NH}_3^+$ ions.

The physical design of the water containment apparatus degrades the energy of the protons entering the water target. Moreover, the IEC fusion chamber, the mechanical methods used to extract the water and the chemical process used to trap the $^{13}\text{NH}_3^+$ ions have an inherent efficiency. Consequently, some ^{13}N atoms will be lost during the production, removal and capture processes. The energy of the protons entering the water target, as well as all possible process efficiencies, must be known in order to accurately compare the measured activity to the predicted activity. Eight isotope production characteristics that either degrade the protons' energy or affect the ^{13}N collection efficiency have been identified and are listed below. The calculated or estimated efficiency for each factor is listed in parenthesis after it is identified.

1) Solid angle of target (0.10): This efficiency represents the fraction of D- ^3He protons created that actually strike the Model SSM2 target. The ratio of the number of protons impinging upon the water target to the number of D- ^3He fusion protons created is determined by the target size. If the target intercepted every proton created within the IEC chamber, this target would be 100% efficient at intercepting the protons. The model SSM2 target contained 70 tubes; the width of this target, measured from the outer edges of the end tubes, is 60 cm. The height of the tubes is also 60 cm. Assuming that this area represents a solid target surface (i.e. no space between the tubes), then the target would have a projected surface area of 3600 cm^2 . The model SSM2 target is located approximately 33 cm from the center of the chamber, and its geometric center is in the same vertical and horizontal plane

as the approximated point source of protons. At that location, a solid target of 3600cm^2 represents a solid angle of 0.138 (the solid target would intercept 13.8% of the protons produced at a point source located in the center of the chamber). But the SSM2 target is not solid – there are small spaces between each pair of vertical tubes. Each tube has a projected width of 0.64 cm, and a projected height of 60 cm, resulting in a combined cross sectional surface area of only 2667 cm^2 for all 70 tubes. In other words, the actual SSM2 target surface area is only 74% of the surface area of the solid square target previously assumed. This leads to an actual solid angle of 0.10. Thus, only about 10% of the protons produced from a point source in the center of the cathode would actually impinge upon the tubes of the SSM2 target.

2) Shadow effect of cathode wires (0.5): Current theories regarding $\text{D-}^3\text{He}$ fusion within the IEC estimate that most $\text{D-}^3\text{He}$ fusion reactions occur within the wires of the cathode [25]. These embedded reactions occur at sites where ^3He ions have been implanted. Assuming all reactions are embedded, half of the $\text{D-}^3\text{He}$ protons created will travel into the cathode wire due to their isotropic distribution. These grid wires are much thicker than the range of a 14.7 MeV proton. Hence, half of the protons produced as a result of embedded reactions are lost within the cathode.

3) Proton energy loss due to embedded reactions (0.998): This is an extension of the shadow effect of the cathode grid wires discussed above. The depth of the embedded reactions is thought to be approximately one micron deep. Depending upon the direction they are ejected, the protons exiting the cathode wires will travel through varying thicknesses of material. The resulting proton current will no longer be monoenergetic; the protons will have a spectrum of energies below 14.7 MeV, which will have the net affect of

decreasing the ^{13}N yield. The stopping power of tungsten is 271 MeV/cm [27]. Assuming pure tungsten cathode wires, an average embedded reaction depth of one micron, and that the average proton is ejected at an angle of 45° with respect to the normal direction, the average thickness of material the proton will pass through is about 1.4 microns. A 14.7 MeV proton traveling through 1.4 microns of tungsten will only lose approximately 0.03 MeV, or 0.2 % of its energy. Assuming the yield is affected by this same amount, this factor is deemed to be 0.998.

4) Cathode transparency (0.96): Based on the projected area of its wires, the cathode transparency has been calculated to be 0.92 for ions accelerated towards it. During isotope production, this factor represents the fraction of protons that are not intercepted by the cathode wires as the protons travel out of the region bounded by the cathode (from embedded reactions). Only half of the protons directed towards the target will have to exit the region bounded by the cathode, and thus be attenuated by the cathode wires; those protons created on the cathode wire surfaces facing outward are already outside the cathode. Therefore, this efficiency is calculated as $(p/2 + 0.92p/2) = 0.96p$, where p is the fraction of protons exiting the region bounded by the cathode.

5) Anode transparency (0.95): Like the cathode, the anode will also intercept a small percentage of the protons that are traveling towards the water target. The fraction of protons that are not intercepted by the anode has been calculated to be 0.95 based on the projected area the wires.

6) Tube geometry (0.60): Because of the round geometry of the tubes in the model SSM2 target, the wall thickness that a proton would see, if it were incident perpendicularly to the projected area of the tube, changes as one moves from the center to the lateral edges

of the tube. This is illustrated in Figure 4.1 and Figure 4.2. If a proton strikes at a location 75° ($5\pi/12$ rad) or greater from the center of the tube with respect to the normal direction, the wall thickness is so great that the proton's energy is reduced below the nuclear cross section threshold (5.8 MeV). Those protons will not create ^{13}N even if they pass through to the water. Moreover, a proton also experiences different wall thickness depending upon what angle it strikes the tube with respect to the horizontal plane of the chamber (see Figure 4.3). A proton incident on the vertical center of the tube, which is in the same horizontal plane as the theoretical point source of protons, would impinge at an angle of zero relative to the horizontal plane. A proton impinging at either the top or bottom of a tube would be incident at an angle of approximately 42.3° (0.738 rad) to the horizontal plane for the SSM2 target located 33 cm from the point source with tubes 60 cm tall. The average wall thickness a proton experiences can be approximated by integrating in both planes as shown below:

$$\bar{T} = 0.0127 \text{ cm} \frac{12}{5\pi} \int_0^{5\pi/12} \frac{1}{0.738} \int_0^{0.738} \frac{d\theta}{\cos\theta} \frac{d\omega}{\cos\omega} = 0.0218 \text{ cm} \quad (4.19)$$

In stainless steel, a 14.7 MeV proton experiences a stopping power of 172.2 MeV/cm [27]. Thus, the average wall thickness of 0.0218 cm results in protons with an average energy of approximately 10.9 MeV – much less than the 12.5 MeV previously assumed. The yield of a 10.9 MeV proton is calculated using Table 4.1 in the same manner as described in Section 4.3 for 12.5 MeV protons. The resulting yield is 11.2 mCi/ μA , which is only 0.62 of the yield for 12.5 MeV protons. Recall, however, that only those protons striking the tube from 0 to $5\pi/12$ rad have been accounted for. The projected width of the tubes from $-5\pi/12$ rad to

$+5\pi/12$ rad represents 0.966 of the total projected tube width $\left(\frac{\sin \frac{5\pi}{12}}{\sin \frac{\pi}{2}} \right)$. These two

fractions are multiplied to yield the total efficiency due to tube geometry of 0.60.

7) Water recovery (0.91): The entire closed loop of the isotope production system holds approximately 1650 mL of water. When the system is pressurized with helium, only 1500 mL of water is expelled from the system and into the ion exchange resin. Much of the water remaining in the system (about 100 mL) is contained in the water expansion reservoir that is in-line with the system but not pressurized when the system is emptied. The other 50 mL of water is assumed to be trapped in the pump and SSM2 target. The 1500 mL of expelled water represents a 0.91 water recovery efficiency.

8) Resin capture (0.95): The true efficiency of the resin's ability to capture the ^{13}N atoms can only be estimated. In order to measure the efficiency, one could measure the activity of the ^{13}N that passed through the resin and compare that to the activity of the ^{13}N captured within the resin. The minute quantity of ^{13}N produced in this experiment made it impossible to accurately measure any ^{13}N activity that may have remained in the approximately 1.5 liters of water that passed through the resin. The ^{13}N concentration in this water is simply too low to measure with the equipment available. Moreover, it's likely that a small fraction of ^{13}N atoms form $^{13}\text{NH}_2^-$, $^{13}\text{NO}_3^-$, and $^{13}\text{NO}_2^-$ ions, which will not be trapped by the DOWEX cation exchange resin. To ensure the resin efficiency was maximized, the amount of ion exchange resin used was larger than that believed necessary. Additionally, the water contained 10 millimolar ethyl alcohol to promote the production of $^{13}\text{NH}_3^+$ ions. Therefore, the resin efficiency is estimated to be 95%.

The product of all eight efficiencies listed above is 0.0236. This equates to 2.36% of all D-³He protons produced in the IEC chamber entering the water target with an energy above the 5.8 MeV cross section threshold for ¹³N production; in that case, all other system efficiencies would be considered 100% efficient. Therefore, if the total number of protons resulting from the reaction of D-³He in the chamber is converted to a current I , then the activity of the ¹³N produced within the model SSM2 apparatus can be estimated by modifying equation (4.14) as:

$$A = (0.764)(0.0236) Y_o I (1 - e^{-\lambda t}) = (0.425 \text{ mCi}/\mu\text{A}) I (1 - e^{-\lambda t}) \quad (\text{mCi}) \quad (4.20)$$

Another way of looking at the above analysis is that under perfect conditions (i.e. a true point source, a perfect ¹⁶O target with no container or obstructions), the maximum saturated production of ¹³N from 14.7 MeV protons in the UW IEC device would be 35.19 mCi/uA. This is 83 times the amount expected from the SSM2 apparatus in the UW device. Although not an attainable yield, this values serves as the upper limit of ¹³N production achievable from the UW IEC.

Table 4.1 - This table is used to solve the integral in equation (4.9) using the midpoint rule. Note that the column on the far right provides the solution to the interval for energy $E + 0.5$ MeV. The pertinent values in this column are in bold.

E (MeV)	σ (mb)	[1] σ (cm ²)	[27] S (MeV-cm ² /g)	σ / S (g/MeV)	σ/S at energy $E + 0.05$ MeV	$\Sigma \sigma/S$ from 5.8 MeV to energy $E + 0.5$ MeV
5.8	0.0	5.74E-30	60.31	9.52E-32	2.459E-30	2.459E-30
5.9	0.3	2.87E-28	59.52	4.82E-30	7.688E-30	1.015E-29
6.0	0.6	6.20E-28	58.75	1.06E-29	1.347E-29	2.361E-29
6.1	1.0	9.50E-28	58.00	1.64E-29	1.788E-29	4.149E-29
6.2	1.1	1.11E-27	57.28	1.94E-29	1.772E-29	5.921E-29
6.3	0.9	9.09E-28	56.57	1.61E-29	1.197E-29	7.119E-29
6.4	0.4	4.40E-28	55.88	7.87E-30	4.652E-30	7.584E-29
6.5	0.1	7.90E-29	55.21	1.43E-30	8.557E-31	7.669E-29
6.6	0.0	1.53E-29	54.56	2.80E-31	2.282E-30	7.898E-29
6.7	0.2	2.31E-28	53.92	4.28E-30	8.493E-30	8.747E-29
6.8	0.7	6.77E-28	53.30	1.27E-29	1.906E-29	1.065E-28
6.9	1.3	1.34E-27	52.70	2.54E-29	3.411E-29	1.406E-28
7.0	2.2	2.23E-27	52.11	4.28E-29	5.439E-29	1.950E-28
7.1	3.4	3.40E-27	51.53	6.60E-29	8.106E-29	2.761E-28
7.2	4.9	4.90E-27	50.97	9.61E-29	1.153E-28	3.914E-28
7.3	6.8	6.78E-27	50.42	1.34E-28	1.582E-28	5.496E-28
7.4	9.1	9.08E-27	49.89	1.82E-28	2.105E-28	7.602E-28
7.5	11.8	1.18E-26	49.36	2.39E-28	2.690E-28	1.029E-27
7.6	14.6	1.46E-26	48.85	2.99E-28	3.273E-28	1.356E-27
7.7	17.2	1.72E-26	48.36	3.56E-28	3.763E-28	1.733E-27
7.8	19.0	1.90E-26	47.87	3.97E-28	2.099E-27	3.832E-27
7.9	180.1	1.80E-25	47.39	3.80E-27	2.447E-27	6.279E-27
8.0	51.3	5.13E-26	46.93	1.09E-27	9.812E-28	7.260E-27
8.1	40.4	4.04E-26	46.47	8.69E-28	8.443E-28	8.104E-27
8.2	37.7	3.77E-26	46.02	8.19E-28	8.132E-28	8.918E-27
8.3	36.8	3.68E-26	45.59	8.07E-28	8.155E-28	9.733E-27
8.4	37.2	3.72E-26	45.16	8.24E-28	8.515E-28	1.058E-26
8.5	39.3	3.93E-26	44.74	8.79E-28	9.055E-28	1.149E-26
8.6	41.3	4.13E-26	44.33	9.32E-28	7.911E-28	1.228E-26
8.7	28.6	2.86E-26	43.93	6.51E-28	4.592E-28	1.274E-26
8.8	11.7	1.17E-26	43.53	2.68E-28	3.344E-28	1.307E-26
8.9	17.3	1.73E-26	43.14	4.01E-28	2.625E-28	1.334E-26
9.0	5.3	5.30E-27	42.76	1.24E-28	1.231E-28	1.346E-26

Table 4.1 continued

E (MeV)	σ (mb)	[1] σ (cm ²)	[27] S (MeV-cm ² /g)	σ / S (g/MeV)	σ/S at energy E + 0.05 MeV	$\Sigma \sigma/S$ from 5.8 MeV to energy E + 0.5 MeV
9.1	5.2	5.18E-27	42.39	1.22E-28	1.227E-28	1.358E-26
9.2	5.2	5.18E-27	42.03	1.23E-28	1.231E-28	1.371E-26
9.3	5.1	5.12E-27	41.67	1.23E-28	1.219E-28	1.383E-26
9.4	5.0	5.00E-27	41.32	1.21E-28	1.196E-28	1.395E-26
9.5	4.8	4.84E-27	40.97	1.18E-28	1.391E-28	1.409E-26
9.6	6.5	6.50E-27	40.63	1.60E-28	1.886E-28	1.428E-26
9.7	8.8	8.75E-27	40.30	2.17E-28	2.424E-28	1.452E-26
9.8	10.7	1.07E-26	39.98	2.68E-28	2.978E-28	1.482E-26
9.9	13.0	1.30E-26	39.65	3.28E-28	3.635E-28	1.518E-26
10.0	15.7	1.57E-26	39.34	3.99E-28	4.413E-28	1.562E-26
10.1	18.9	1.89E-26	39.03	4.84E-28	5.332E-28	1.615E-26
10.2	22.6	2.26E-26	38.73	5.83E-28	6.388E-28	1.679E-26
10.3	26.7	2.67E-26	38.43	6.95E-28	7.565E-28	1.755E-26
10.4	31.2	3.12E-26	38.13	8.18E-28	8.808E-28	1.843E-26
10.5	35.7	3.57E-26	37.84	9.43E-28	1.002E-27	1.943E-26
10.6	39.9	3.99E-26	37.56	1.06E-27	1.110E-27	2.054E-26
10.7	43.2	4.32E-26	37.28	1.16E-27	1.192E-27	2.173E-26
10.8	45.4	4.54E-26	37.01	1.23E-27	1.240E-27	2.297E-26
10.9	46.1	4.61E-26	36.74	1.25E-27	1.251E-27	2.423E-26
11.0	45.5	4.55E-26	36.47	1.25E-27	1.227E-27	2.545E-26
11.1	43.7	4.37E-26	36.21	1.21E-27	1.177E-27	2.663E-26
11.2	41.3	4.13E-26	35.95	1.15E-27	1.112E-27	2.774E-26
11.3	38.4	3.84E-26	35.70	1.08E-27	1.039E-27	2.878E-26
11.4	35.5	3.55E-26	35.45	1.00E-27	9.652E-28	2.975E-26
11.5	32.7	3.27E-26	35.20	9.29E-28	8.964E-28	3.064E-26
11.6	30.2	3.02E-26	34.96	8.64E-28	8.337E-28	3.148E-26
11.7	27.9	2.79E-26	34.72	8.04E-28	7.787E-28	3.225E-26
11.8	26.0	2.60E-26	34.49	7.54E-28	7.334E-28	3.299E-26
11.9	24.4	2.44E-26	34.25	7.13E-28	6.967E-28	3.368E-26
12.0	23.2	2.32E-26	34.03	6.80E-28	6.690E-28	3.435E-26
12.1	22.2	2.22E-26	33.80	6.58E-28	6.504E-28	3.500E-26
12.2	21.6	2.16E-26	33.58	6.43E-28	6.439E-28	3.565E-26
12.3	21.5	2.15E-26	33.36	6.44E-28	6.495E-28	3.630E-26
12.4	21.7	2.17E-26	33.15	6.55E-28	6.674E-28	3.696E-26
12.5	22.4	2.24E-26	32.93	6.80E-28	7.022E-28	3.767E-26

Table 4.1 continued

E (MeV)	σ (mb)	[1] σ (cm ²)	[27] S (MeV-cm ² /g)	σ / S (g/MeV)	σ/S at energy E + 0.05 MeV	$\Sigma \sigma/S$ from 5.8 MeV to energy E + 0.5 MeV
12.6	23.7	2.37E-26	32.73	7.24E-28	7.480E-28	3.842E-26
12.7	25.1	2.51E-26	32.52	7.72E-28	7.881E-28	3.920E-26
12.8	26.0	2.60E-26	32.32	8.04E-28	7.914E-28	3.999E-26
12.9	25.0	2.50E-26	32.12	7.78E-28	7.338E-28	4.073E-26
13.0	22.0	2.20E-26	31.92	6.89E-28	6.394E-28	4.137E-26
13.1	18.7	1.87E-26	31.72	5.90E-28	5.548E-28	4.192E-26
13.2	16.4	1.64E-26	31.53	5.20E-28	5.042E-28	4.243E-26
13.3	15.3	1.53E-26	31.34	4.88E-28	4.865E-28	4.291E-26
13.4	15.1	1.51E-26	31.15	4.85E-28	4.958E-28	4.341E-26
13.5	15.7	1.57E-26	30.97	5.07E-28	5.295E-28	4.394E-26
13.6	17.0	1.70E-26	30.78	5.52E-28	5.865E-28	4.453E-26
13.7	19.0	1.90E-26	30.60	6.21E-28	6.670E-28	4.519E-26
13.8	21.7	2.17E-26	30.43	7.13E-28	7.747E-28	4.597E-26
13.9	25.3	2.53E-26	30.25	8.36E-28	9.069E-28	4.687E-26
14.0	29.4	2.94E-26	30.08	9.77E-28	1.052E-27	4.793E-26
14.1	33.7	3.37E-26	29.91	1.13E-27	1.185E-27	4.911E-26
14.2	37.0	3.70E-26	29.74	1.24E-27	1.266E-27	5.038E-26
14.3	38.1	3.81E-26	29.57	1.29E-27	1.266E-27	5.164E-26
14.4	36.6	3.66E-26	29.41	1.24E-27	1.195E-27	5.284E-26
14.5	33.5	3.35E-26	29.24	1.15E-27	1.088E-27	5.393E-26
14.6	30.0	3.00E-26	29.08	1.03E-27	9.866E-28	5.491E-26
14.7	27.2	2.72E-26	28.92	9.42E-28	4.708E-28	5.538E-26

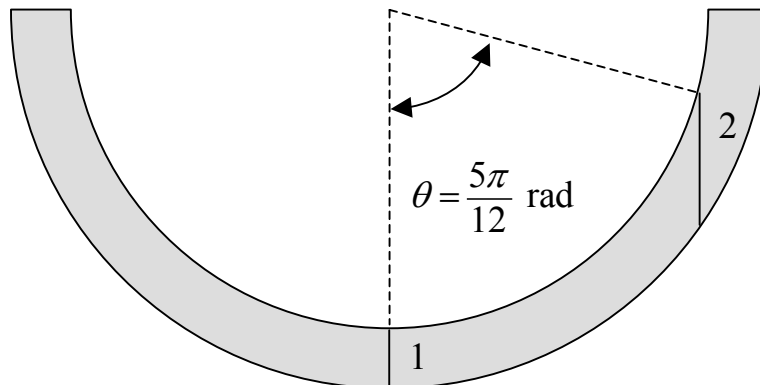


Figure 4.1 – The thickness of the tube wall of the SSM2 target changes for a proton striking perpendicularly to the cross-sectional plane. Hence, a proton striking at point 2 must travel through more stainless steel than a proton striking at point 1.

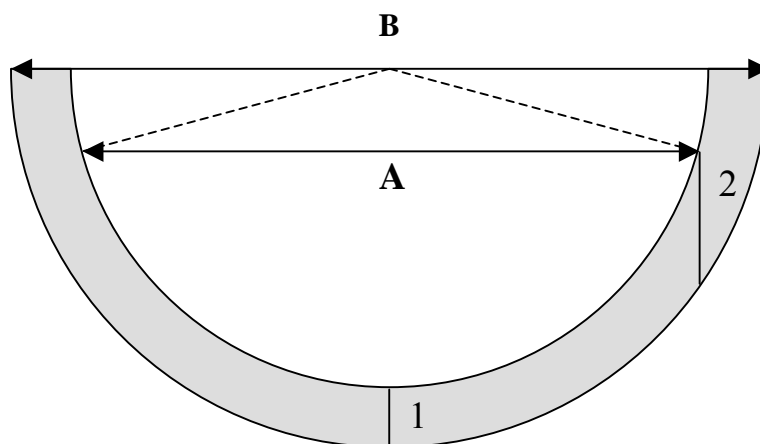


Figure 4.2 – The width of the tube A represents the frontal projected width of a tube in which an incident proton is still capable of undergoing nuclear reactions once it reaches the water. The width B represents the total projected tube width. Width A is 96.6% of the entire tube width B.

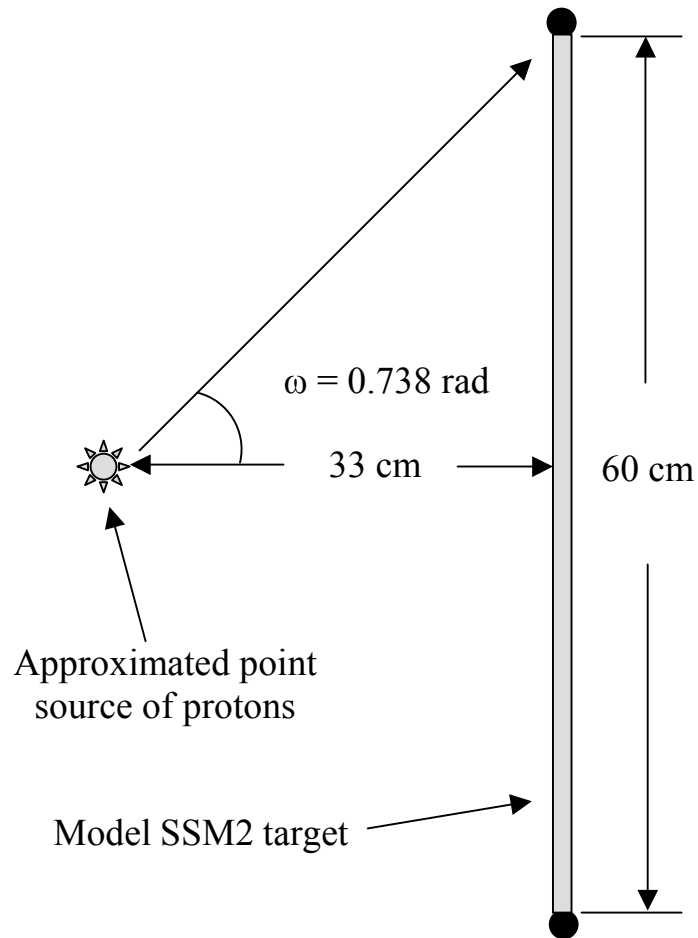


Figure 4.3 – Protons striking the tubes of the model SSM2 target in the same horizontal plane as the approximated point source of protons will travel through the least amount of wall material. Protons impinging upon the tubes near their top or bottom must pass through a greater wall thickness.

Chapter 5 Experimental Technique and Equipment

Section 5.1 Water Target and Ion Exchange Resin Preparation

The two most important items for this experiment are the water target and the ion exchange resin. To optimize the performance of these two critical items, the same preparation and experimental procedure was followed for every attempted production run. As discussed in Chapter 3, the DOWEX 50WX8 (100-200) cation exchange resin will capture a variety of cations. Moreover, the quantity of ions the resin can hold is limited. Once all the ionic exchange sites are expended, no additional ions passing through the resin will be captured. Consequently, the radioisotope production system needed to be as free of contaminant ions as possible to ensure every ^{13}N atom was captured. During the many conditioning runs leading up to a production run, reverse osmosis water was used in the closed-loop production system to keep it as clean as possible. This water was also changed every day. Prior to a production run, the closed-loop water circuit was rinsed three times with 18 M Ω -cm water. For the first rinse, the system was briefly flushed with 18 M Ω -cm water. The system was then filled with pure 18 M Ω -cm water, which was circulated for approximately 1 hour. It was then flushed a second time with 18 M Ω -cm water and then again filled with pure water, which was circulated for approximately 30 minutes. The system was flushed a third time and filled with 18 M Ω -cm water, which was circulated for 15 minutes. Finally, the system was filled with 18 M Ω -cm water containing 10 millimolar ethyl alcohol to promote the formation of $^{13}\text{NH}_3^+$ ions.

A special plastic container was used to transport the 18 M Ω -cm water. Before it was filled, it was first rinsed with reverse osmosis water, then with 18 M Ω -cm water. It was

then filled with argon gas to minimize the formation of carbonic acid caused by the interaction of the pure water with the carbon dioxide in the atmosphere. The 18 M Ω -cm water was then poured into the container.

The ion exchange resin also had to be prepared prior to each production run. The first step was to place approximately 25 grams of DOWEX 50WX8 (100-200) cation exchange resin into a clean glass beaker. This quantity of resin was chosen because it filled the column to a height of nearly three inches, which is the width of the NaI crystal used to count the activity of ^{13}N trapped in the resin. In other words, the column contained the maximum amount of resin that would fit within the boundaries of the detector face. Next, 100 mL of 0.1 molar NaOH was mixed with the resin for several minutes to recharge the ionic sites with the Na^+ ions in this solution. During the production run, these Na^+ ions would exchange with $^{13}\text{NH}_3^+$ ions in the water, capturing the ammonia in the resin in the same manner as a water softener removes minerals from a household water supply.

The resin column, which was just a 60 cc plastic syringe, was thoroughly rinsed with 18 M Ω -cm water. A bundle of glass wool was then placed at the bottom of the syringe. The glass wool served as a filter by allowing the water to easily pass through but retaining the resin in the syringe. The NaOH and resin solution was then poured into the column (syringe). To remove the traces of resin remaining in the beaker, it was rinsed several times with small amounts of 18 M Ω -cm water, which was also poured into the syringe. As necessary, the syringe plunger was used to force this solution through the resin and out of the syringe. Additional 18 M Ω -cm water was then slowly poured into the syringe and forced through the resin. This was done approximately 20 times to rinse the NaOH from the

resin. It was very important to ensure all NaOH was removed. If some NaOH remained trapped in the resin, the Na^+ ions could exchange with sites containing ^{13}N atoms during a production run. These ^{13}N atoms might then be lost. After this rinsing cycle, the pH of the water was measured to ensure that after passing through the resin it was 7. This indicated that all of the NaOH had been removed.

After flushing the resin column thoroughly, it was connected to the isotope extraction system with an airtight clamp. An exploded view of the resin column and clamping mechanism is shown in figure 5.1. Figure 5.2 shows a picture of the column with the ion exchange resin inside, and a picture of the column fully assembled is shown in figure 5.3. The airtight clamp enabled the column to be pressurized, forcing the water through the resin without leaks. The wastewater passing through the column was collected in a plastic container and stored in the control room for several hours after each run. This water was measured for radioactivity after many production runs, but no activity was ever detected. Even so, it was stored prior to disposal to ensure any ^{13}N or other short-lived radioisotopes decayed away.

The last step in preparing the radioisotope production system was connecting a pressurizing helium line. This helium line was maintained at 50 psi and was separated from the system by a valve. When the production run was terminated, the valve was opened, pressurizing the system and quickly forcing the water through the ion exchange resin column. This process took approximately two minutes to complete. The resin column was then disconnected from the water circuit, placed in a plastic bag to prevent radioactive contamination from any water spilled onto its surface, and rushed to the 3 x 3 NaI detector in the UW nuclear reactor (UWNR) lab, usually arriving within three minutes of shut down.

Section 5.2 Production Run Procedure

Once the water and ion exchange column were prepared and the IEC was ready for an isotope production run, the large fan mounted in the IEC operation room was turned on. The aluminum IEC chamber relies on air-cooling to dissipate the many kilowatts of power generated inside. For an isotope production run, the IEC was operated at the highest power possible, so the additional cooling of the fan was required to keep the rubber seals of the chamber from exceeding their temperature limits. A second portable fan was placed facing the side of the IEC opposite the large mounted fan. These two fans kept the surface of the IEC chamber below 70° C during all production runs.

To help keep the chamber cool as long as possible, the filaments were turned off several hours before the production run. This enabled the chamber to cool and reach equilibrium with the surrounding room temperature. Additionally, the voltage and current were brought to production levels as quickly as possible when the production run began. Rather than stepping the voltage up in 10 kV increments as was typically done during conditioning runs, the voltage was steadily increased to 100 kV in approximately one minute. It was then allowed to operate at this voltage for about one minute, and was then brought to production levels (~ 140 kV) over the next minute.

The chamber pressure was initially set to approximately 1.4 mtorr during production runs. Previous pressure scans with D-³He fuel suggested that the reaction rate was optimized at a pressure near 1.4 mtorr. However, the chamber tended to operate more smoothly at pressures near 1.8 mtorr. The pressure often increased during any high power run due to increased outgassing of the chamber as it was heated. The chamber pressure was

allowed to reach 1.8 mtorr before the fuel inflow rates were manually reduced to maintain the pressure below 1.8 mtorr.

The ratio of D to ^3He inside the IEC was maintained at 1:1 according to measurements by the residual gas analyzer (RGA). Equal peaks do not necessarily mean that the amount of each gas, either by weight or by volume, is equal. The method by which the RGA analyzes gases can indicate that the peaks are equal even though the amount of each gas present is not. This is referred to as the cracking pattern of a gas, and the cracking pattern of many gasses are available in the RGA technical literature. This literature does not list the cracking pattern for isotopes such as D and ^3He , however, so the exact ratio of these two gases is not precisely known. It was noted in previous IEC experiments that the D- ^3He reaction rate was optimized (as measured by the proton detector) when these peaks were matched on the RGA.

After the production run is terminated, the water circuit of the isotope production system is pressurized with helium to quickly force it through the ion exchange resin column. This is done by opening and closing a series of valves as shown in figure 5.4. First, the water pump is unplugged. The water is forced out of the system in the opposite direction it was circulated, so the pump must be off to reverse this flow. Next, the two valves controlling water into and out of the expansion reservoir are closed. Following this, a valve is opened that enables water to flow into the resin column. Last, a valve is opened that pressurizes the water circuit with 50 psi helium, forcing the water out of the system and through the resin column. The water is collected in a container as it passes out of the column as shown in figure 5.4. The resin column is then detached, the plunger is inserted into the syringe to compress the resin in as small a volume as possible, and the syringe is

placed in a plastic bag. The plastic bag prevents water from leaking out of the syringe and contaminating the surrounding environment, such as the detector face, with radioactivity.

The activity of the ^{13}N contained in the ion exchange resin was counted using a single 3 x 3 NaI detector. A thin sheet of plastic is permanently mounted on the face of the detector to protect it. As shown in figure 5.5, the column was placed on this plastic sheet with the downstream edge of the resin immediately above the edge of the detector. This was done assuming that the upstream end would have a higher ^{13}N activity. This end would then be closer to the middle of the detector, resulting in a higher counting efficiency.

The electronics associated with the detector system are detailed in the schematic diagram of figure 5.6. The 3 x 3 NaI detector, photomultiplier tube (PMT) and base are housed in a large lead vault to shield it from background radiation. These components were manufactured by Teledyne Isotopes. A Canberra Model 3102 high voltage power supply is used to bias the detector to +600 volts. The detector output is connected directly to the input of an ORTEC Model 440A selectable active filter amplifier. The amplifier course gain is set to 32x, the fine gain set to 2.3, and the shaping time set to 1 μs . The amplifier output signal is fed to a multi-channel analyzer (MCA) installed in a desktop computer.

A region of interest (ROI) was set in the energy spectrum of the MCA. This ROI extended from 470 keV to 570 keV and was established at either end of a 511 keV photopeak using a ^{22}Na source. This ROI would be used as the standard energy range with which to compare the future activity of $^{13}\text{NH}_3$ samples produced in the IEC. The MCA software provided the gross number (sample plus background) of counts within the ROI. By subtracting the background activity from the gross activity of the column, one can calculate the net activity of $^{13}\text{NH}_3$ in the resin.

Using the technique described in Chapter 4, the anticipated activity of ^{13}N produced in the IEC was on the order of 37 Bq (1 nCi). For an activity this small, it was determined that the sample should be counted in two-minute intervals to provide counting statistics with 95% certainty. Since radioactive decay detection follows a Poisson distribution, the error σ in counting a sample activity is the square root of the number of counts [7]. The desired statistical certainty can then be used to determine the total number of counts required from:

$$\sigma = \frac{\sqrt{N}}{N} = \frac{1}{\sqrt{N}} \quad (5.1)$$

where N is the total detected number of counts. Once the total number of counts required for a desired level of accuracy is known, the count time (in seconds) is easily determined by dividing N by the anticipated activity in Bq.

Many two-minute count sequences would be done in order to establish a decay curve for the radionuclide. The MCA was programmed to count for two minutes; the program did not automatically log (save) the count data and restart, however, so this was done manually. In this manner, numerous counts are made. As the activity of the sample decayed, the count time required to obtain 95% should be increased. The count time was not increased for these counts, though, for two reasons. First, it was extremely convenient to have the MCA automatically terminate the count time at some preset length. This count time could not be programmed for sequentially increasing count times; it could only be set for a single, constant count time. Resetting the count time for each count interval would consume some time and also invite errors. Second, it was desired to keep the count time to as small a fraction of the half-life as possible. In doing this, the activity could be approximated as a constant during the count time. Hence, each count of the resin column was done over a two-

minute interval. As described in Chapter 6, however, the count time was eventually extended to three-minute intervals when it was determined that the activity of ^{13}N created was much less than anticipated.

When the counting process for the resin column was completed, a 10-minute background reading was done. This is accomplished by removing the resin column from the lead vault and setting the MCA to automatically count for 10 minutes. After adjusting the background counts measured in 10 minutes to a 2-minute background count, it is subtracted from the gross activity of the resin column to determine the net activity of the ^{13}N trapped in the resin.

In order to determine the true activity of the ^{13}N in the column, the detector's efficiency at detecting 511 keV photons had to be determined. This was accomplished by using a calibrated ^{22}Na radiation source. The ^{22}Na emits a positron during 89.9% of its decays. The positron eventually collides with an electron, emitting two 511 keV gamma rays in the same manner as ^{13}N . For the detector efficiency measurement, the ^{22}Na source was not placed on the center of the detector face. Rather, it was located slightly off-center. This was done to mimic the conditions of counting the resin column. It's believed that the upstream end of the resin column contains the highest concentration of ^{13}N activity. Since this portion of the column is located off center of the detector face as shown in figure 5.5, the ^{22}Na source was placed in the same area relative to the detector face.

The activity of the calibrated source at the time of the efficiency test was calculated to be 82.0 nCi. This value is multiplied by 0.899 to account for only those decays that emit a positron, resulting in an activity of 73.7 nCi or 2,729 Bq. A 300 second count of this source detected 140,717 counts in the photopeak. This equates to a detected activity of 469

Bq. Efficiency is defined as the ratio of photons detected to those emitted. In accordance with that definition, the efficiency of the UWNR NaI detector was found to be 17% for 511 keV gamma rays. This efficiency does not take into account the self-shielding affects of the resin column, which is approximately 2.5 cm in diameter. To determine this effect, the resin column is assumed to have the same energy attenuation coefficient as water. For 511 keV gamma rays, this value is determined to be 0.0955 cm^{-1} [35]. On average, a 511 keV gamma ray travels through 1.25 cm of resin. Using the formula for gamma ray attenuation in matter:

$$\frac{I}{I_0} = e^{-\mu T}$$

where

I = intensity of gamma rays outside medium

I_0 = intensity of source of gamma rays

T = thickness of material traversed by the gamma rays

The attenuation of the resin is approximated to be 10%. In other words, approximately 90% of the gamma rays escape the resin column. Hence, the overall detection efficiency is determined to be $(0.17)(0.90) = 15\%$.

The difference in detector efficiency due to geometry differences between the thin, flat calibrated radionuclide sample and the much larger volume of the resin column is neglected. Assuming that the majority of the ^{13}N is captured near the upstream end of the resin column as discussed, the source of ^{13}N is approximated to be a point source. Therefore, the detection efficiency of the resin column is assumed to be identical to that of the calibrated source.

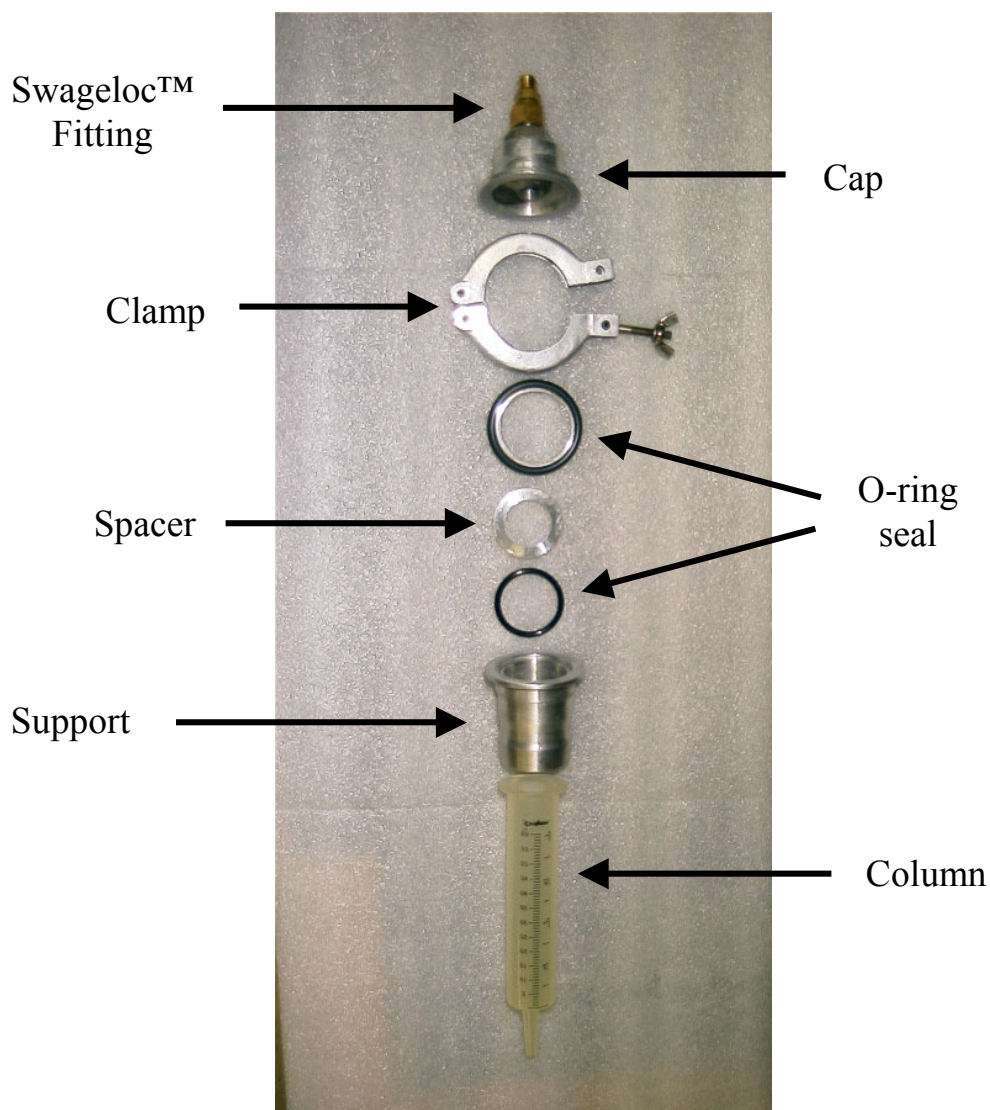


Figure 5.1 – Exploded view of ion exchange column. The column is a 60 cc syringe plastic syringe. The syringe was placed in the support, which was mounted to the frame of the IEC chamber. The o-ring seals were used to create the airtight seal between the support and the cap. The clamp holds the entire assembly together. Water enters the column through the Swageloc™ fitting on the top of the cap.



Figure 5.2 – Photograph of resin column with ion exchange resin inside.

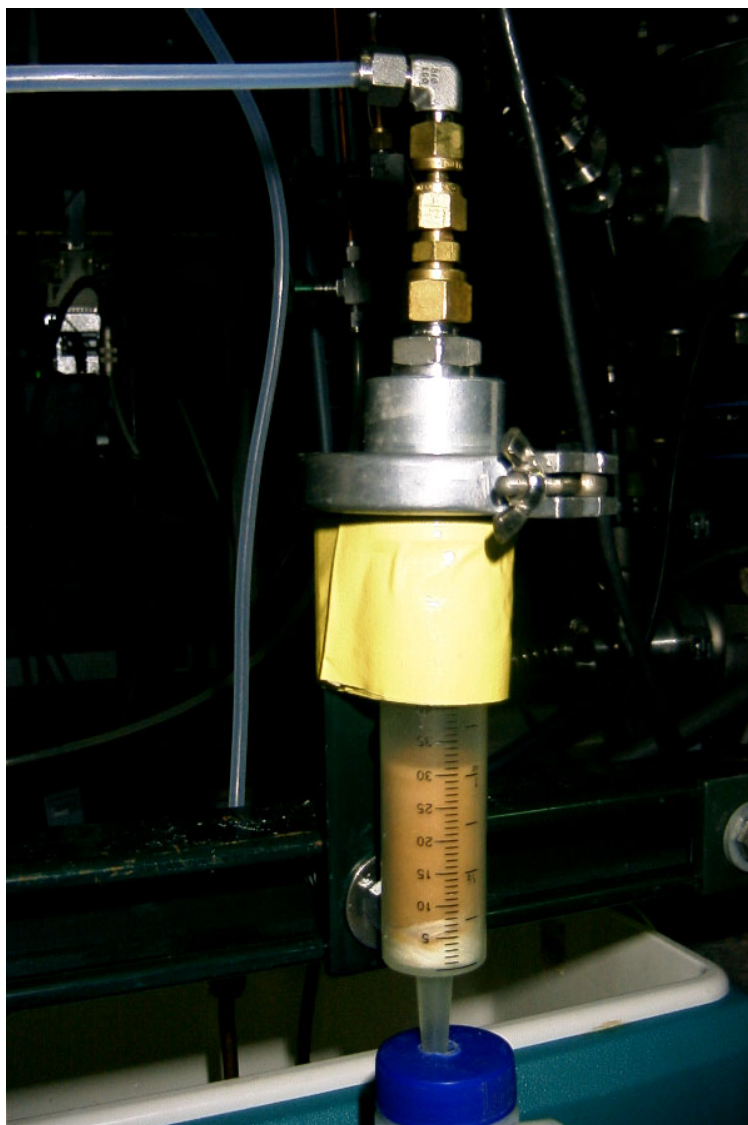


Figure 5.3 – Ion exchange column mounted just below the IEC chamber. The water flows into the column through the plastic tubing at the top of the picture. After the water flows through the resin, it is collected in a waste container.

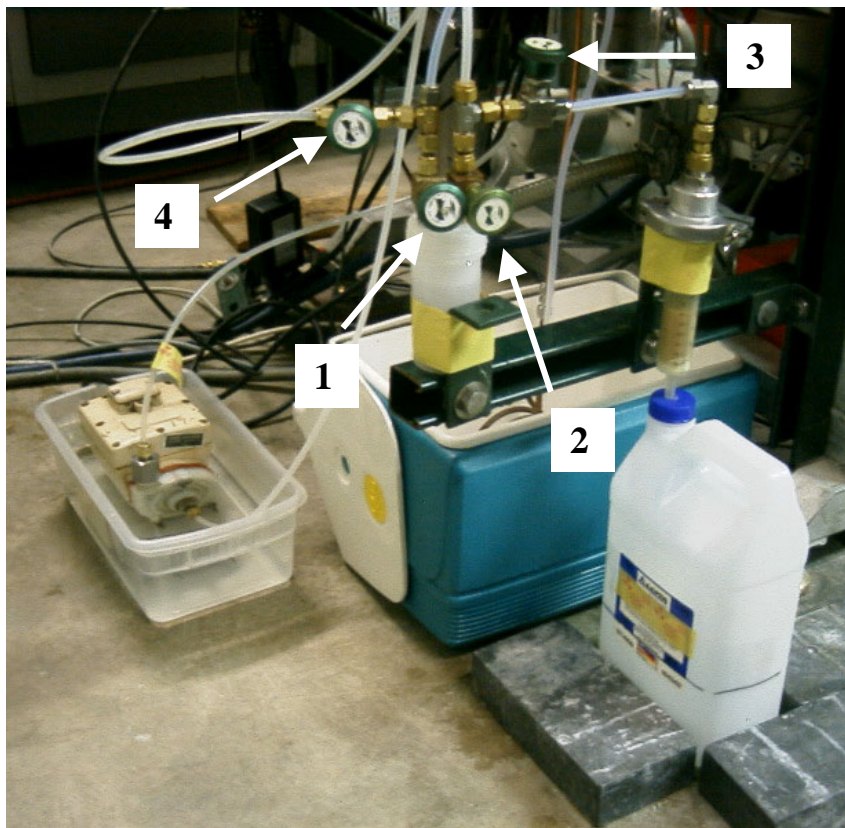


Figure 5.4 – Picture of valves controlling the water flow through the isotope production system. To pressurize the system and force the water out through the resin column, the water pump was first unplugged. Valves 1 and 2 were then closed, stopping the flow of water into and out of the expansion reservoir. Valve 3 was then opened to allow the water to enter the resin column. Finally, valve 4 was opened, which pressurized the system with 50 psi of helium. The water is forced out of the isotope production system in the opposite direction in which it was circulated by the pump. This was done to take advantage of gravity in draining the water containment apparatus inside the chamber.

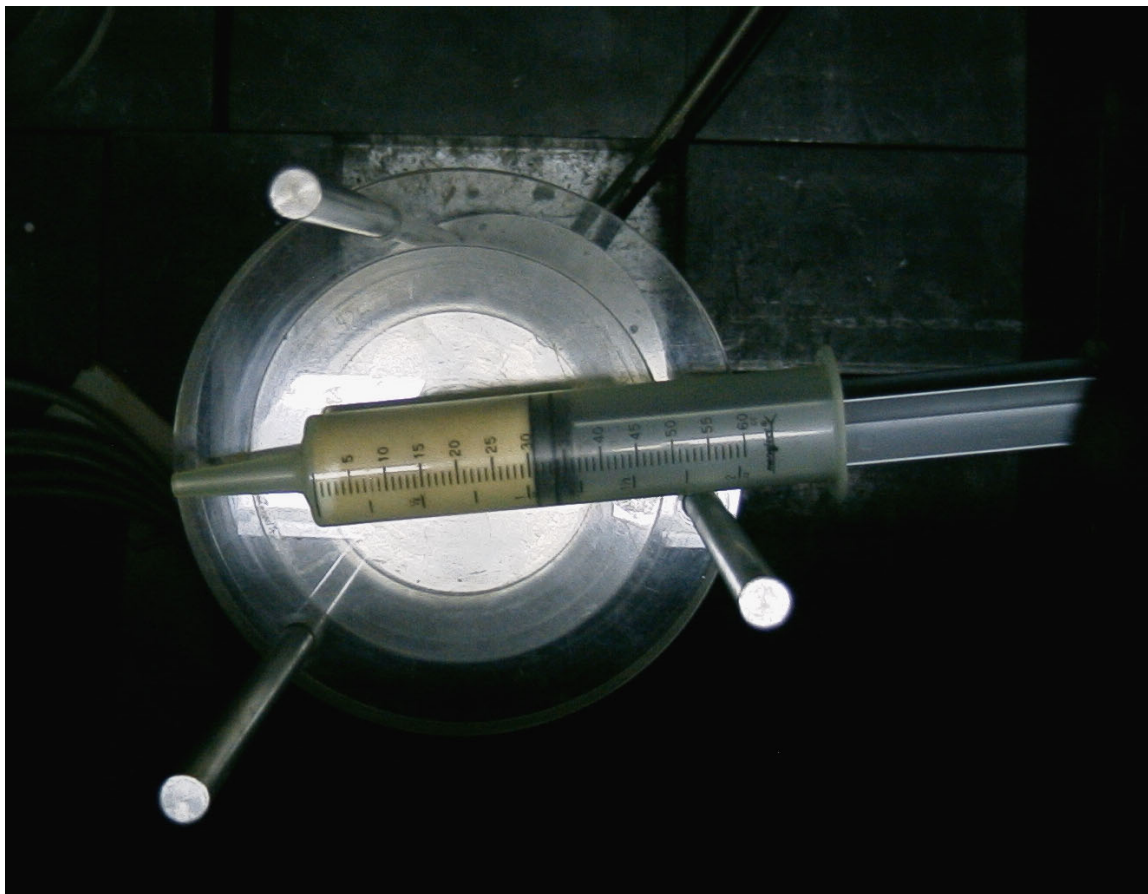


Figure 5.5 – Photograph of the ion exchange resin column located on the 3 x 3 NaI detector for counting. The downstream edge of the column is placed immediately above the edge of the detector, enabling the upstream end (assumed to have the greatest activity) to be closer to the center of the detector. During an actual count, the column was placed in a plastic bag to prevent it from contaminating the detector. The door of the lead vault is closed during counting.

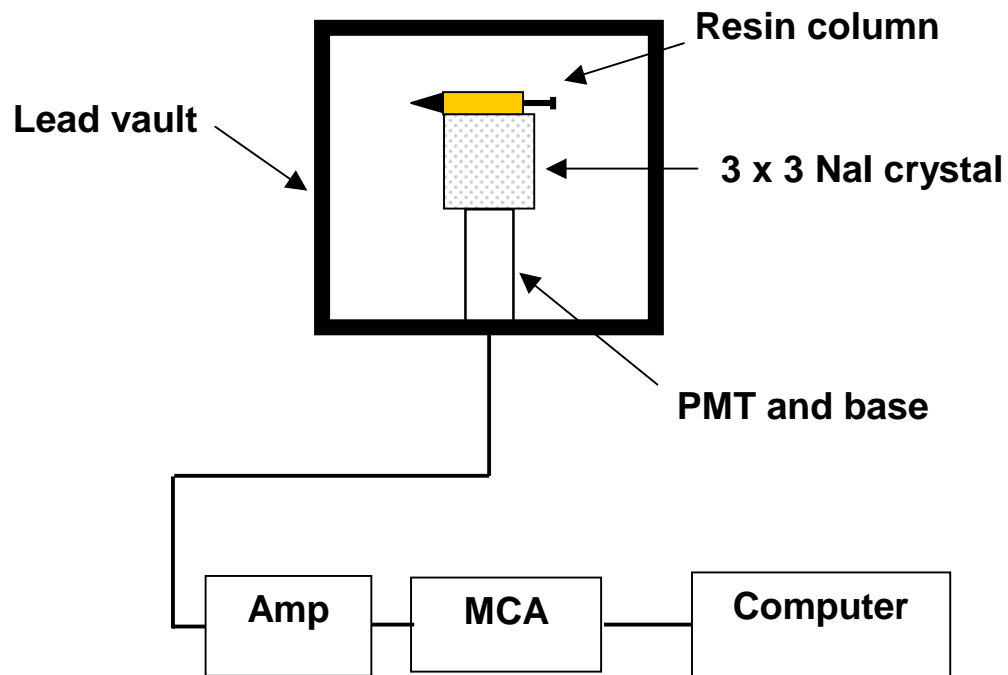


Figure 5.6 – Schematic diagram of 3 x 3 NaI detection circuit located in the University of Wisconsin nuclear reactor lab.

Chapter 6 Experimental Results

Section 6.1 February 19th, 2003 Production Run

During the time window of operation available for this experiment, two successful ^{13}N production runs were conducted. Many partially successful runs were also conducted prior to and after these runs. The first successful run occurred on February 19th, 2003. For approximately two weeks prior to this, numerous conditioning runs were done to push the IEC operating regime to as high a voltage as achievable. During these conditioning runs, the stalk was observed to glow as conditions approached 130 kV and 30 mA. The glowing began at the tip of the stalk near the cathode as shown in figure 6.1, and slowly progressed up the stalk with time. When the glowing began, the $\text{D-}^3\text{He}$ reaction rate, as measured by the proton detector, was observed to significantly decrease in a linear manner with run time. The impurities within the chamber significantly increased too, which was attributed to stalk outgassing. The cathode heating pattern also transitioned from a fairly symmetric glow to a very asymmetric glow as shown in figure 6.2. It was believed that this particular stalk became conductive as its temperature increased. Consequently, it was drawing ion current away from the cathode. These ions deposited their energy into the stalk, further raising the stalk's temperature. This increased the stalk's conductivity, which attracted more ions. The runaway cycle could not be overcome by manipulating the operating pressure or by reducing the time to reach 130 kV. Despite these adverse operating characteristics, ^{13}N production runs were conducted due to the limited time window for experimentation.

The experiment was prepared as described in Chapter 5. The goal of the February 19th run was to operate at 145 kV and 35 mA for 20 minutes (\sim two ^{13}N half-lives). This

would produce a ^{13}N yield approximately 75% of the saturated activity. If the chamber shut down during this time, the experiment would be restarted as quickly as possible and the run extended to reach a total of 20 minutes of proton bombardment. The chamber pressure was initially set to approximately 1.4 mtorr, but it was expected to rise during the experiment due to outgassing by the glowing stalk. The pressure would be maintained below 1.8 mtorr during the experiment by adjusting the flow of D and ^3He into the chamber.

For activity calculation purposes, the time equals zero point is defined as the time when the IEC was turned on. It took approximately three minutes to bring the IEC up to 145 kV and 35 mA. No proton counts were taken during this time so that the software would be ready to begin counting as soon as those conditions were achieved. The voltage and current were allowed to vary slightly during the run. No attempt was made to keep the voltage or current at exactly 145 kV or 30 mA since the reaction rate, not the applied voltage or current, was the important factor. Moreover, it was felt that continually adjusting the operating conditions contributed to arcing and other run difficulties.

The IEC ran very well during the first several minutes of the run as shown by a plot of the raw proton counts in figure 6.3. To prevent the machine from shutting down when significant arcing occurred, the voltage was reduced approximately 15 kV for several seconds. Although temporarily decreasing the voltage also temporarily decreased the reaction rate, this was much preferable to an arc that could shut down the machine for a minute or more.

After approximately six minutes of bombardment (nine minutes into the experiment), the stalk began to glow. As expected, the chamber pressure increased so the flow of D and ^3He into the chamber was reduced. The cathode began to arc regularly, and approximately

10 minutes into the experiment the machine shut down. During the first attempt to start the machine and quickly bring it back up to 145 kV and 35 mA, it shut down again. The machine was restarted and brought to operating conditions as quickly as possible, but this delay lasted approximately three minutes. Furthermore, as soon as the desired operating conditions were achieved, the stalk immediately started glowing again. The next few proton counts clearly showed that the reaction rate was steadily decreasing. It was decided to continue the run until the raw proton counts per minute dropped below 50,000. This occurred 22 minutes into the run. At that point, the run was manually terminated. A summary of the operational characteristics for this run is included in table 6.1. The water target was passed through the ion exchange resin as described in Chapter 5, and the resin column was brought to the NaI detector in the UW nuclear reactor (UWNR) lab. The first count of the resin column began approximately two and a half minutes after shut down.

The resin column was counted for five 180-second intervals. The data for each of these counts is located in Appendix A of this document. Immediately after the five raw counts were concluded, a 10-minute count of the background activity was taken. The raw activity of each count was determined, and then the adjusted background activity was subtracted to yield the net ^{13}N activity. Finally, the net activity was divided by the detection efficiency, measured to be 15%, to yield the true activity for each counting period. These results are shown in table 6.2. A plot of the true activity for each count is shown in figure 6.4. The graph in figure 6.4 contains two curves. The black curve represents an exponential fit of the data done using Microsoft Excel™(tm). As shown on the graph, the data is very well defined by an exponential equation as indicated by the R^2 value of 0.993. The R^2 value

is a regression analysis that uses the least squares method to fit a line or curve to the data using the formula:

$$R^2 = 1 - \frac{\sum_1^j (Y_j - \hat{Y}_j)^2}{\left(\sum_1^j Y_j\right)^2 - \frac{\left(\sum_1^j Y_j\right)^2}{n}} \quad (6.1)$$

An R^2 value of 1 indicates an exact functional fit to the data. The decay constant provided by the fit is 0.0009141, which differs from the true ^{13}N decay constant of 0.0011593 by 21%. The fit value and true value of the decay constant may have had better agreement if the first count could have been taken sooner or if more counts had been made.

The red line in figure 6.4 is the decay curve a theoretical sample of ^{13}N would follow if it possessed an initial activity of 0.230 nCi or 8.5 Bq at the end of bombardment (EOB). This line passes within the error bars of each data point and suggests that the radioisotope being detected is ^{13}N .

Section 6.2 Calculating the Factor That Relates Detected Proton Rate to Total D-³He Reaction Rate Inside IEC Device

Recall that the proton detector mounted on the IEC measures only a very small fraction of the total D-³He proton current inside the chamber. By knowing the activity of ^{13}N produced in this experiment, the total proton current inside the IEC can be found using equation (4.20). The detected D-³He proton current can be related to the total D-³He current inside the IEC chamber by a calibration factor. In effect, this calibration factor represents the number by which the detected D-³He proton rate must be multiplied by in order to provide a total D-³He reaction rate (proton current) inside the chamber that would produce

the quantity of ^{13}N that was measured. This calibration factor is calculated by first determining the time-dependent proton current required in order to have created the quantity of ^{13}N produced at the end of bombardment. This is done in table 6.3 and figure 6.5. Once the time dependent current is determined, the calibration factor relating the detected proton rate to the total proton current required is straightforward as shown in table 6.4. From these calculations, the calibration factor is determined to be 2,804. Thus, the number of protons from $\text{D-}^3\text{He}$ reactions detected by the proton detector must be multiplied by 2,804 to yield the total proton current within the IEC.

Section 6.3 February 21st, 2003 Production Run

The second successful ^{13}N production run was conducted on February 21st, 2003. The glowing stalk problem had grown continually worse, and high-power IEC operation was limited to approximately 10 minutes. Nonetheless, it was believed that a measurable quantity of ^{13}N could be produced.

The goal of this production run was to operate at 145 kV and 35 mA for 10 minutes. As with the first production run, the time equal zero point was defined as the moment the IEC was turned on. The first proton count was started two minutes into the run. Due to significant arcing, the machine shut down only four minutes into the run. After restarting the IEC, the arcing persisted. This significantly reduced the detected proton rate between five and eight minutes into the run as shown in table 6.5. Although the arcing did begin to subside nearly nine minutes into the experiment, the stalk then began to glow. To minimize the decrease in the $\text{D-}^3\text{He}$ reaction rate, the current was increased to 35 mA. This did little to offset the reaction rate falloff, so the voltage was increased to 145 kV, and then to 150 kV

a few minutes later. After 10 minutes of continuous operation, the machine was shut down. The water target was flushed through the resin as before and rushed to the UWNR detector.

The resin column was again counted for five 180-second intervals. The specific data for each of these counts is located in Appendix B. At the conclusion of these five counts, a background count was conducted as previously described. Using this data, the net activity detected for each count was determined. This was then used to calculate the true activity of ^{13}N in the resin by dividing the net activity by the 15% detection efficiency. These calculations are shown in table 6.6. A plot of the resulting decay curve is shown in figure 6.6. As before, two curves are included in this decay curve. The shorter, black curve is an exponential fit of the data points using Microsoft Excel™. As noted on the graph, the R^2 value of the fit is 0.975, indicating the data is well defined by an exponential equation. More importantly, the fit yields a decay constant value of 0.0011440. This differs from the true ^{13}N decay constant of 0.0011593 by only 1.3%. Lastly, the red line is the decay curve a theoretical sample of ^{13}N would follow if it had an initial activity at EOB of 0.135 nCi. The fit curve and theoretical decay curves lie on top of each other, providing strong evidence that ^{13}N was created in this experiment.

As with the February 19th production run, a calibration factor is determined that relates the detected protons current, shown in figure 6.7, to the total proton current inside the chamber. This is done in the same manner as before, and the calculations are shown in table 6.7 and 6.8 as well as figure 6.8. This experiment yields a calibration factor of 4,088.

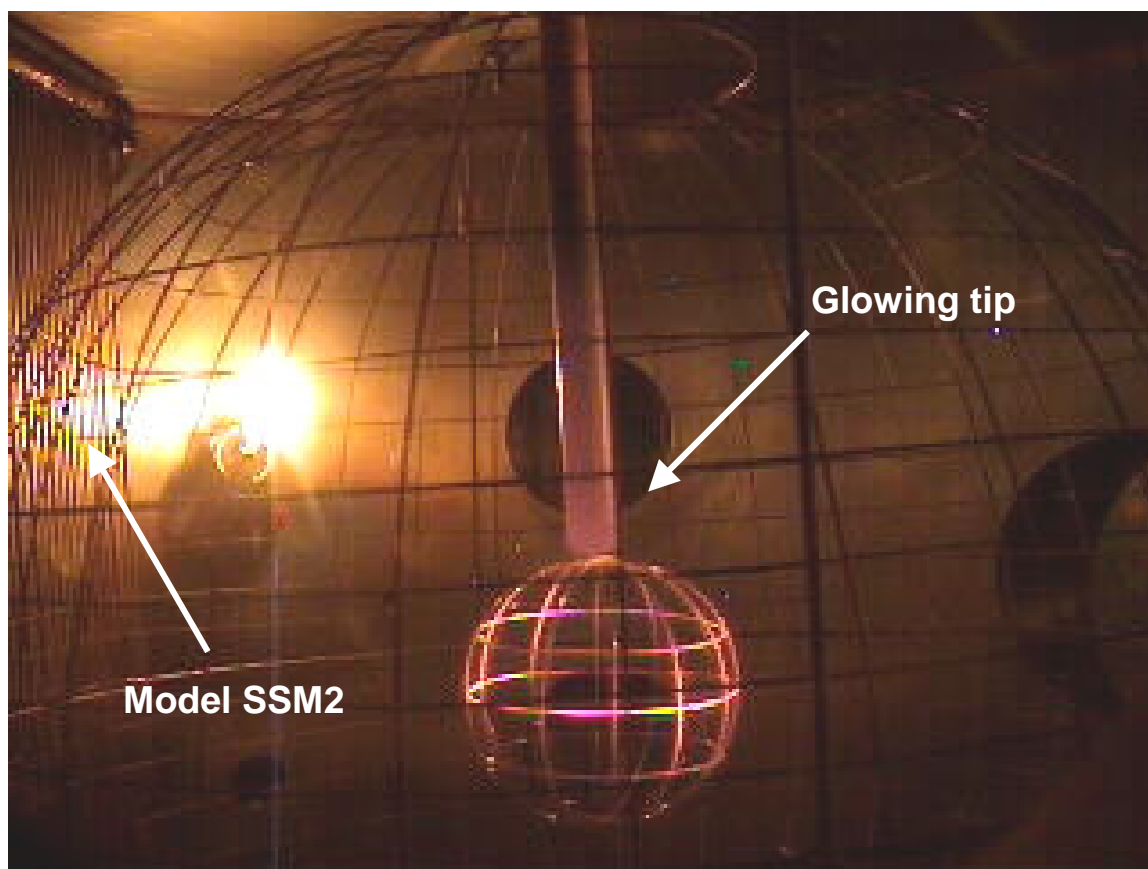


Figure 6.1 – During the conditioning runs leading up to the production runs of late February 2003, the stalk began glowing at its tip. The glowing was thought to occur because this particular stalk was becoming conductive as it was heated. This attracted ions that collided with the stalk, further increasing its temperature and conductivity. The gaseous impurities inside the chamber also significantly increased as the glowing began, likely due to stalk outgassing.

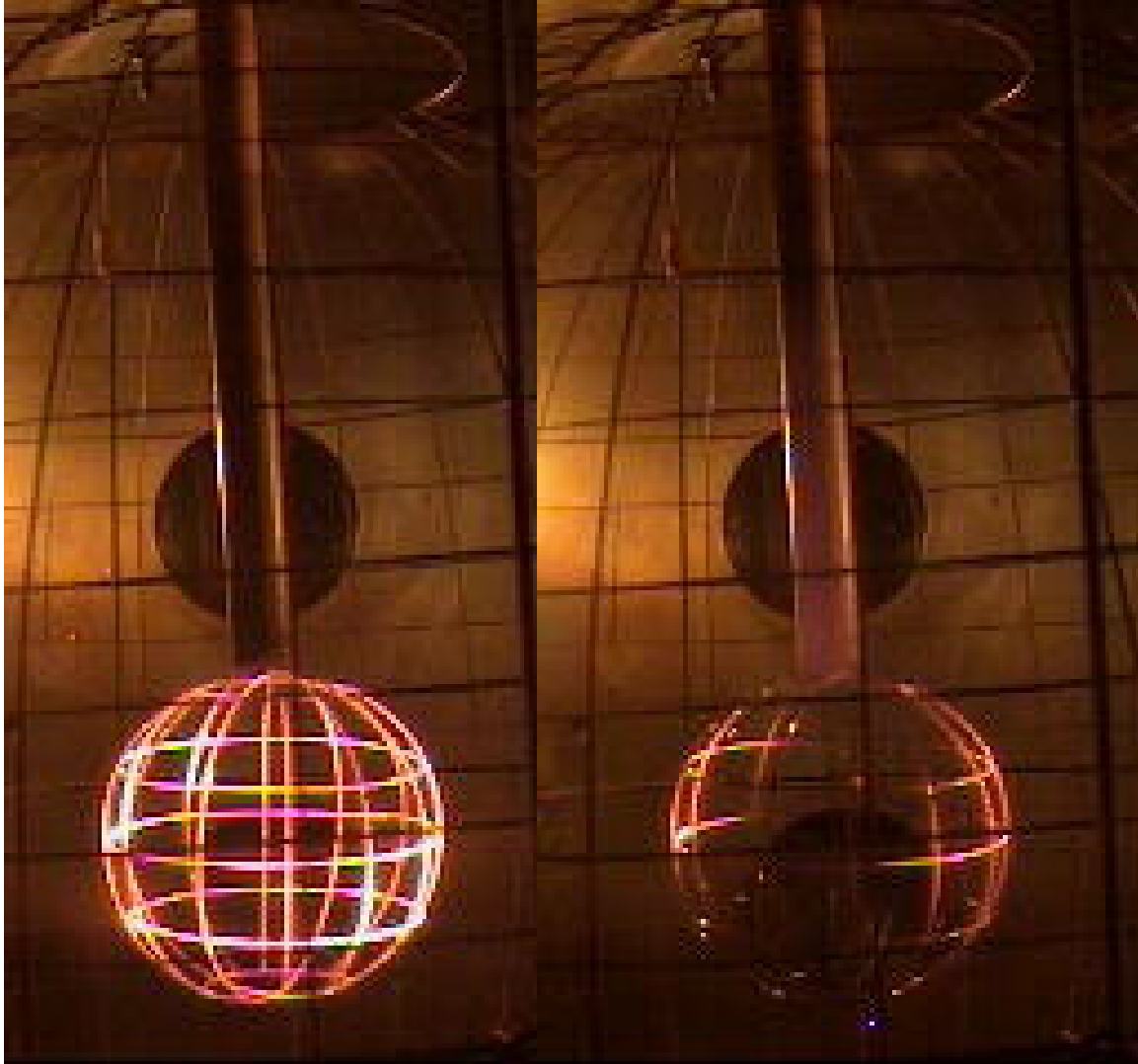


Figure 6.2 – The cathode heating pattern was dramatically altered as the stalk began to glow. The image on the left shows the cathode uniformly heated early in the production run on February 19th, 2003. The image on the right shows asymmetric cathode heating after the stalk began glowing. It's thought this was caused by the stalk becoming conductive and drawing ion current away from the cathode.

Detected Proton Current Inside IEC Chamber as a Function of Run Time During the February 19th, 2003 Production Run

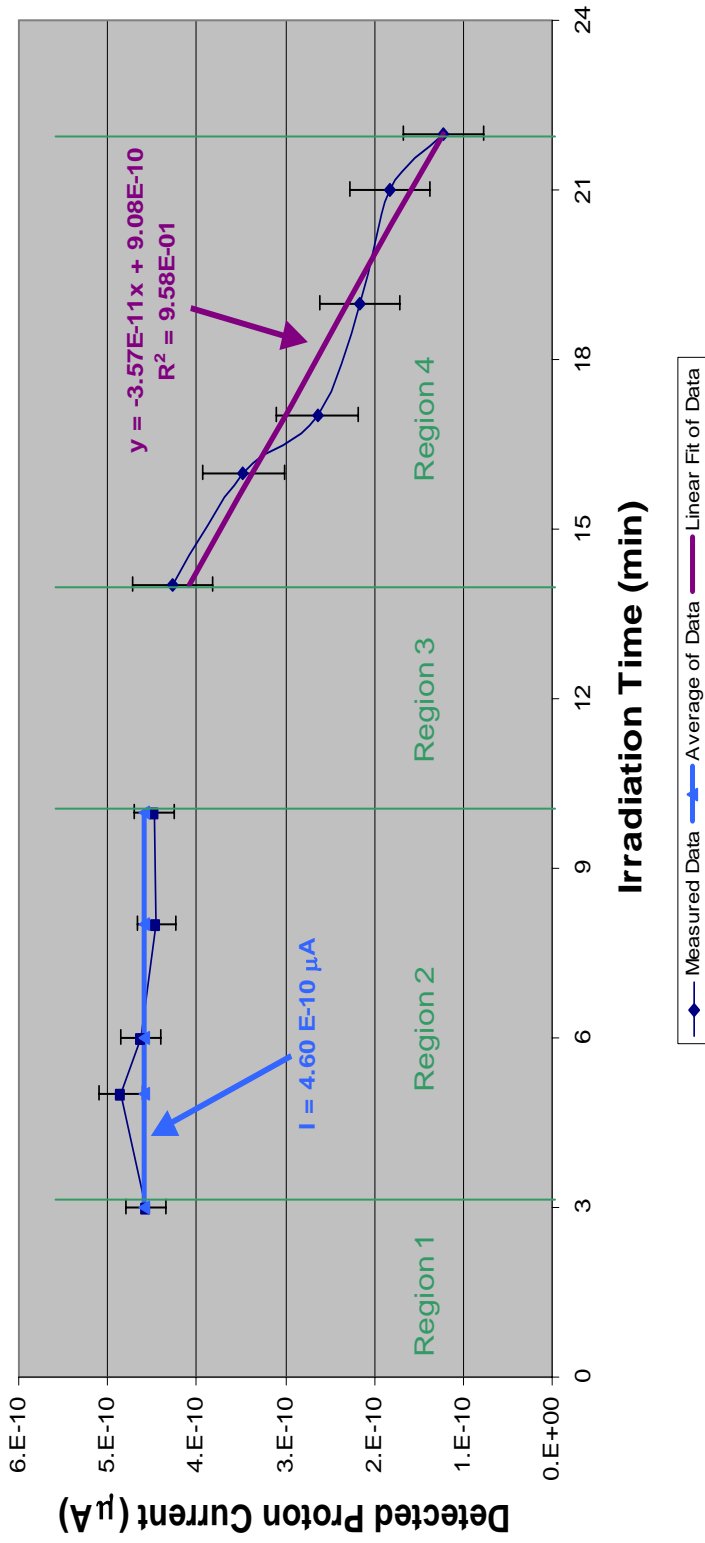


Figure 6.3 – Plot of the detected proton current as a function of run time for production run conducted February 19th, 2003 (IEC run 790). These currents are based on the detected proton rate taken in one-minute intervals. The detected proton current was divided into four regions. The proton current in region 1 and region 3 is assumed to be zero. The proton current in region 2 is defined to be a constant equal to the average of the current reading in the region. The error in the measured proton rate is judged to be 5% in this region. In region 4, a line fit to the data defines the time dependent proton current. The error in the measured proton rate for this region is judged to be a constant 0.5 E-10 μA based on run conditions.

Run Time (min)	Voltage (kV)	Current (mA)	Pressure (mtorr)	Measured D- ³ He Protons/min	Water Temp (°C)
0	40	30	1.50	0	15
1	100	30	1.60		16
3	140	30	1.68	171171	20
5	145	34	1.78	182160	27
6	145	32	1.77	173589	29
8	145	31	1.80	166878	34
10	145	35	1.85	167860	
11	0	0		0	
12	0	0		0	
13	130	30			
14	145	30	1.85	159974	33
16	145	30	1.96	130195	35
17	145	33	1.72	98968	37
19	145	30	1.82	81082	40
21	145	30	1.77	68446	41
22	145	33	1.85	45940	43

Table 6.1 – Operating conditions for February 19th, 2003 isotope production run. Empty positions indicate the data was not measured for that time period. Note that the pressure increased from 1.50 mtorr to nearly 2.0 mtorr. The D and ³He flow rates were then reduced to lower the overall chamber pressure. The IEC shut down approximately 10 minutes into the run due to arcing around the cathode. The tip of the stalk began glowing at 16 minutes. The water temperature was measured using a thermocouple that was thermally cemented to the copper tube carrying the water out of the IEC chamber.

Count #	Count Time (s)	Count Start Time After EOB (sec)	Gross Cts in 180 s	σ (cts)	Bkgd Cts in 180 s	σ (cts)	Net Cts	σ (cts)	Net Activity (dps)	σ (dps)	True Activity (dps)	σ (dps)	True Activity (nCi)	σ (nCi)
1	180	156	264	16.2	85	9.2	179	18.7	0.99	0.104	6.63	0.519	0.179	0.014
2	180	347	234	15.3	85	9.2	149	17.9	0.83	0.099	5.52	0.496	0.149	0.013
3	180	550	216	14.7	85	9.2	131	17.3	0.73	0.096	4.85	0.482	0.131	0.013
4	180	755	190	13.8	85	9.2	105	16.6	0.58	0.092	3.89	0.461	0.105	0.012
5	180	945	171	13.1	85	9.2	86	16.0	0.48	0.089	3.19	0.444	0.086	0.012

Table 6.2 - Raw 511 keV gamma ray count data from February 19th production run. The time that elapsed between end of bombardment (EOB) and the start of the each count is listed in the third column from the left. The net activity is found by subtracting the background activity (obtained from a 10-minute count and interpolated to a 180-second interval) from the gross number of counts for that period. The true activity is then obtained by dividing the net activity by the detection efficiency.

Decay Curve for February 19th, 2003 Production Run

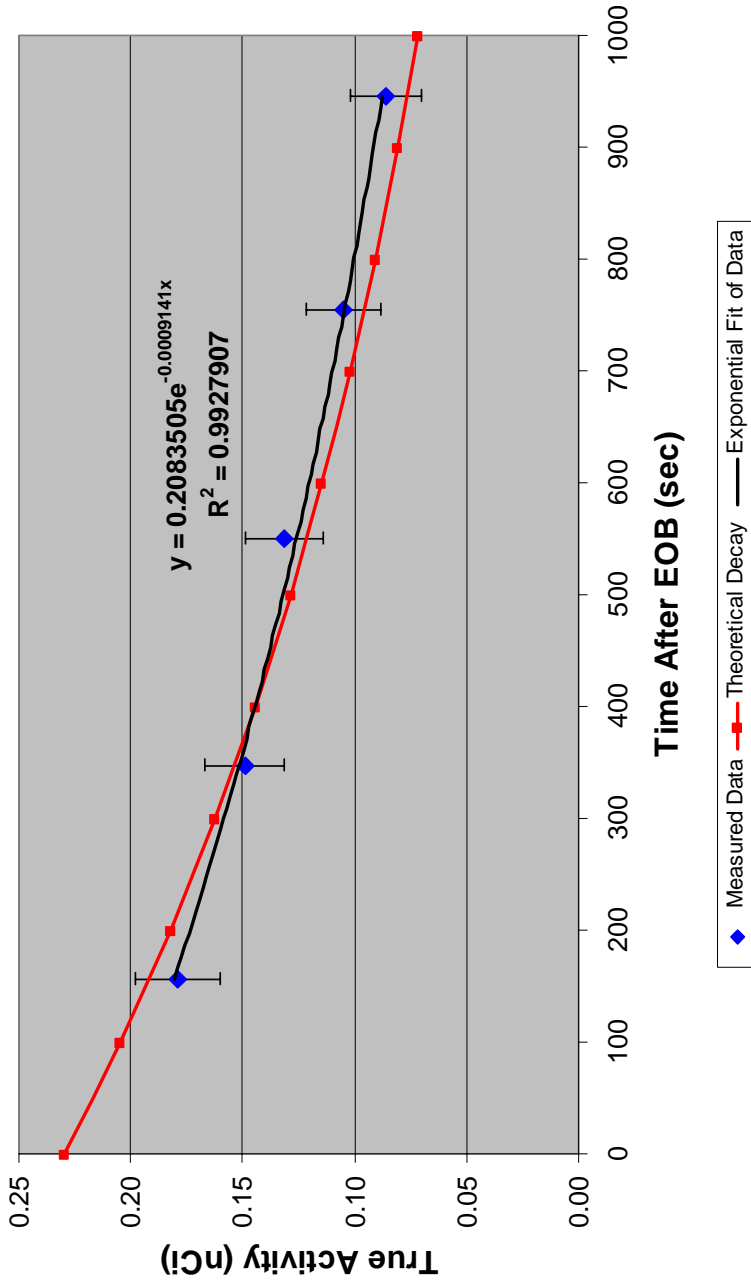


Figure 6.4 – Plot of 511 keV activity in resin column measured during five 180-second counting periods as a function of time after end of bombardment (EOB). The red line is the decay curve a theoretical sample of ^{13}N would follow if it possessed an initial activity of 0.230 nCi at EOB. The black line is a fit of the measured data, which yields a decay constant of 0.0009141 s^{-1} .

T	I (uA)	P (nCi)	EOB A (nCi)
3.0	1.289E-06	0.793	0.211
3.5	1.289E-06	0.793	0.219
4.0	1.289E-06	0.793	0.227
4.5	1.289E-06	0.793	0.235
5.0	1.289E-06	0.793	0.243
5.5	1.289E-06	0.793	0.252
6.0	1.289E-06	0.793	0.261
6.5	1.289E-06	0.793	0.270
7.0	1.289E-06	0.793	0.279
7.5	1.289E-06	0.793	0.289
8.0	1.289E-06	0.793	0.299
8.5	1.289E-06	0.793	0.310
9.0	1.289E-06	0.793	0.321
9.5	1.289E-06	0.793	0.332
10.0	1.289E-06	0.793	0.344
14.0	1.146E-06	0.705	0.404
14.5	1.096E-06	0.674	0.400
15.0	1.046E-06	0.643	0.395
15.5	9.956E-07	0.613	0.390
16.0	9.455E-07	0.582	0.383
16.5	8.955E-07	0.551	0.376
17.0	8.454E-07	0.520	0.367
17.5	7.954E-07	0.489	0.358
18.0	7.453E-07	0.459	0.347
18.5	6.953E-07	0.428	0.335
19.0	6.452E-07	0.397	0.322
19.5	5.952E-07	0.366	0.308
20.0	5.451E-07	0.335	0.292
20.5	4.951E-07	0.305	0.274
21.0	4.450E-07	0.274	0.255
21.5	3.950E-07	0.243	0.235
22.0	3.449E-07	0.212	0.212

Potential Activity at EOB (nCi) 9.746

$$(9.746 \text{ nCi})(0.0236) = 0.230 \text{ nCi}$$

Table 6.3 – Table used to calculate the proton current required to produce an amount of ^{13}N equivalent to the quantity estimated at the end of bombardment (EOB) for the production run conducted February 19th. The proton current for times between 14 and 22 minutes is found from a fit of the detected proton rate in figure 6.5. Using the values for the time-dependent flux in the table above, the potential ^{13}N activity is calculated to be 9.746 nCi. This value is multiplied by the 0.0236 system efficiency to yield a calculated ^{13}N activity of 0.230 nCi, which is the same as the estimated activity at EOB from the measured results in figure 6.4. This proton current then is used to calculate the calibration factor (table 6.4).

Time	Measured protons/min	Predicted p/s*	Current (uA)
3	171171	8.00E+06	1.28E-06
5	182160	8.51E+06	1.36E-06
6	173589	8.11E+06	1.30E-06
8	166878	7.80E+06	1.25E-06
10	167860	7.84E+06	1.26E-06
11	0	0	0
12	0	0	0
13	0	0	0
14	159974	7.48E+06	1.20E-06
16	130195	6.08E+06	9.74E-07
17	98968	4.63E+06	7.40E-07
19	81082	3.79E+06	6.06E-07
21	68446	3.20E+06	5.12E-07
22	45940	2.15E+06	3.44E-07

***Calibration Factor = 2804**

Table 6.4 – Table used to calculate the calibration factor of the proton detector required in the IEC in order to produce the activity of ^{13}N that was measured from the February 19th, 2003 run. The calibration factor is adjusted until the current matches that required in table 6.3 to yield the measured ^{13}N activity of 0.230 nCi. Multiplying the measured proton counts per minute by the calibration factor and dividing by 60 seconds yields the total proton reaction rate per second in the IEC. The proton current is then obtained by multiplying the reaction rate per second by 1.6×10^{-13} .

**Total Proton Current Required Inside UW IEC to Produce the
Activity of ¹³N Measured from February 19th, 2003 Production
Run**

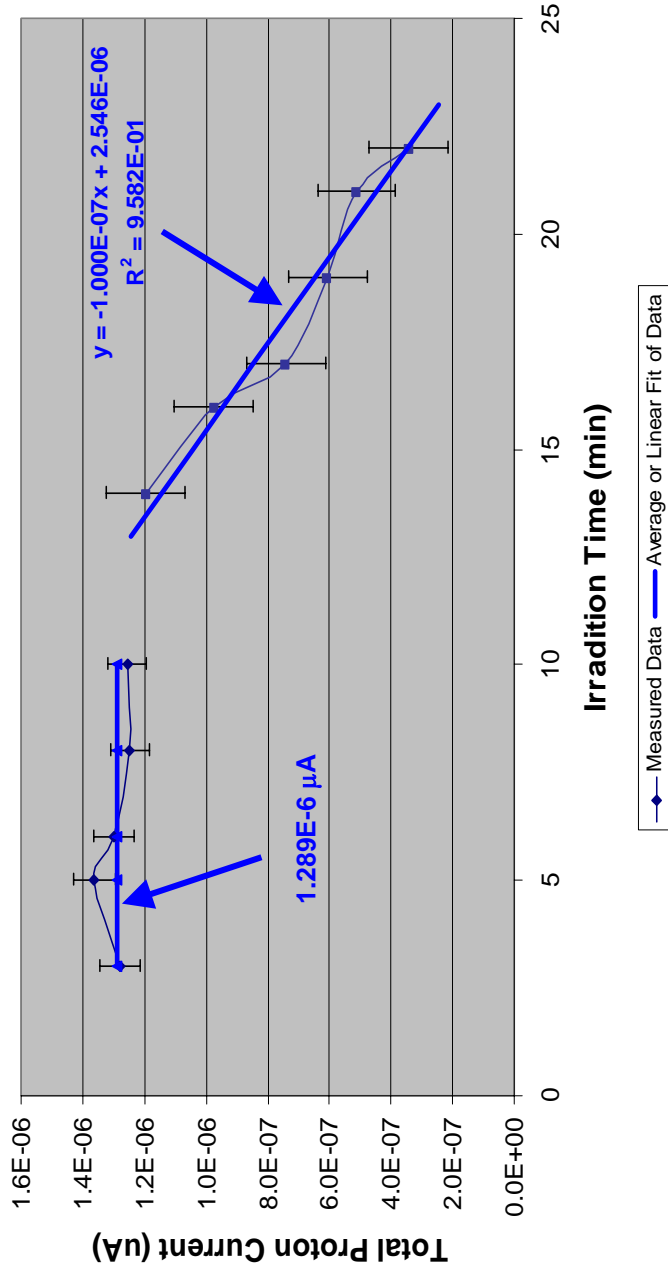


Figure 6.5 – Plot of total proton current necessary inside the IEC to produce the activity of ¹³N at the end of bombardment (EOB) as estimated from figure 6.4 using the calibration factor of 2,804 from table 6.5. The average proton current from 3 to 10 minutes into the run would need to be 1.289 E-6 μA . From 14 to 22 minutes, the proton current (in μA) is defined by the fit equation in the figure above.

Run Time (min)	Voltage (kV)	Current (mA)	Pressure (mtorr)	Measured D- ³ He Protons/min	Water Temp (°C)
0	40	30	1.49	0	23
1	120	30	1.57		25
2	140	30	1.54	121338	31
4	140	30	1.49	0	
5	140	30	1.45	141920	34
8	135	30	1.64	103132	36
9	140	30	1.68	121174	38
10	140	35	1.73	115589	39
12	140	35	1.75	89156	41
14	145	35	1.80	91994	43
15	150	35	1.96	74802	45

Table 6.5 - Operating conditions for February 21st, 2003 isotope production run. Empty positions indicated the data was not measured for that time period. The IEC shut down due to arcing approximately four minutes into the run. The stalk began glowing 10 minutes into the run, and the cathode heating became very asymmetric 12 minutes into the run. For calculation purposes, the activity of ¹³N created during the brief operational period two minutes into the run is neglected. Table 6.7 shows that the contribution from this brief period is only about 3% of the total ¹³N produced.

Count #	Count Time (s)	Count Start Time After EOB (sec)	Gross Cts in 180 s	σ (cts)	Bkgd Cts in 180 s	σ (cts)	Net Cts	σ (cts)	Net Activity (dps)	σ (dps)	True Activity (dps)	σ (dps)	True Activity (nCi)	σ (nCi)
1	180	225	200	14.1	94	9.7	106	17.1	0.589	0.095	3.926	0.635	0.106	0.017
2	180	415	172	13.1	94	9.7	78	16.3	0.433	0.091	2.889	0.604	0.078	0.016
3	180	615	166	12.9	94	9.7	72	16.1	0.400	0.090	2.667	0.597	0.072	0.016
4	180	805	146	12.1	94	9.7	52	15.5	0.289	0.086	1.926	0.574	0.052	0.016
5	180	995	137	11.7	94	9.7	43	15.2	0.239	0.084	1.593	0.563	0.043	0.015

Table 6.6 - Raw 511 keV gamma ray count data from February 21st production run. The time that elapsed between end of bombardment (EOB) and the start of the each count is listed in the third column from the left. The net activity is found by subtracting the background activity (obtained from a 10-minute count and interpolated to a 180-second interval) from the gross number of counts for that period. The true activity is then obtained by dividing the net activity by the detection efficiency.

Decay Curve for February 21st, 2003 Production Run

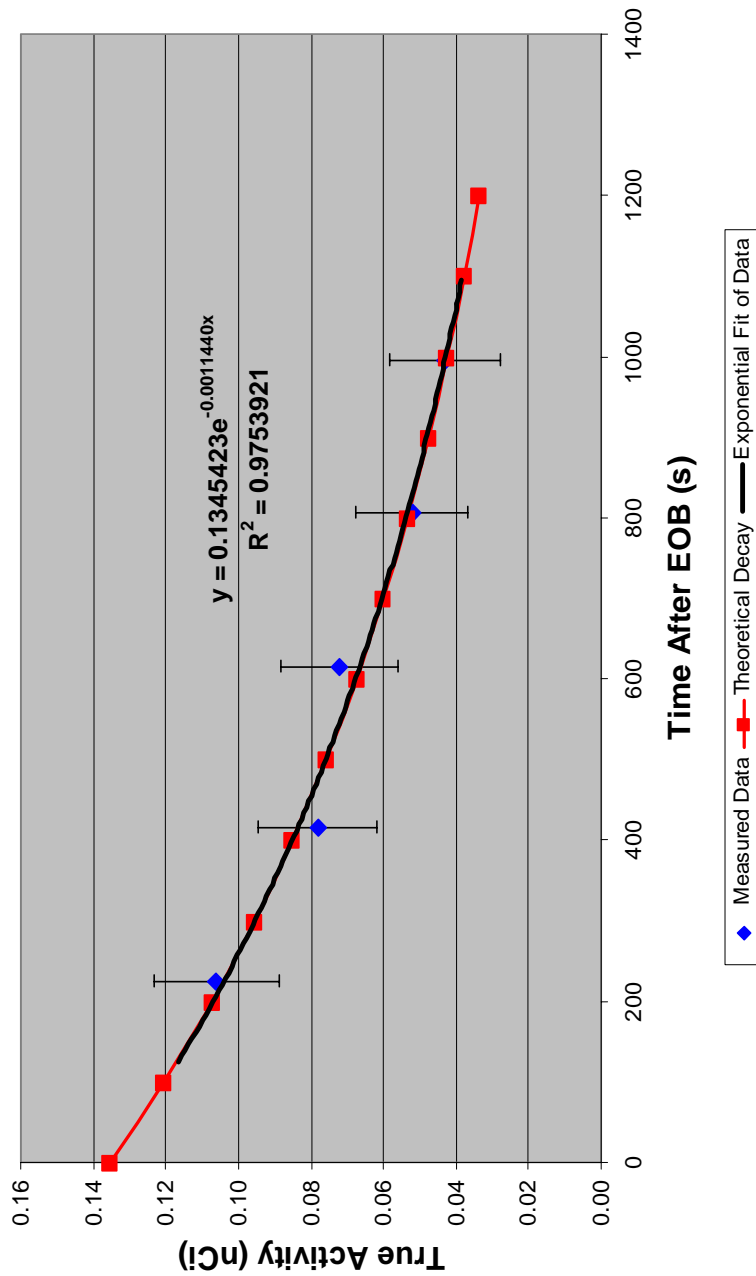


Figure 6.6 – Plot of 511 keV activity in resin column activity measured during five 180-second counting periods as a function of time after end of bombardment (EOB). The red line is the decay curve a theoretical sample of ^{13}N would follow if it possessed an initial activity of 0.135 nCi at EOB. The black line is a fit of the measured data, which yields a decay constant of $0.00011440 \text{ s}^{-1}$. This value differs from the actual ^{13}N decay constant by only 1.3%.

Relevant Proton Current Detected Inside IEC Chamber as a Function of Run Time During February 21st, 2003 Run

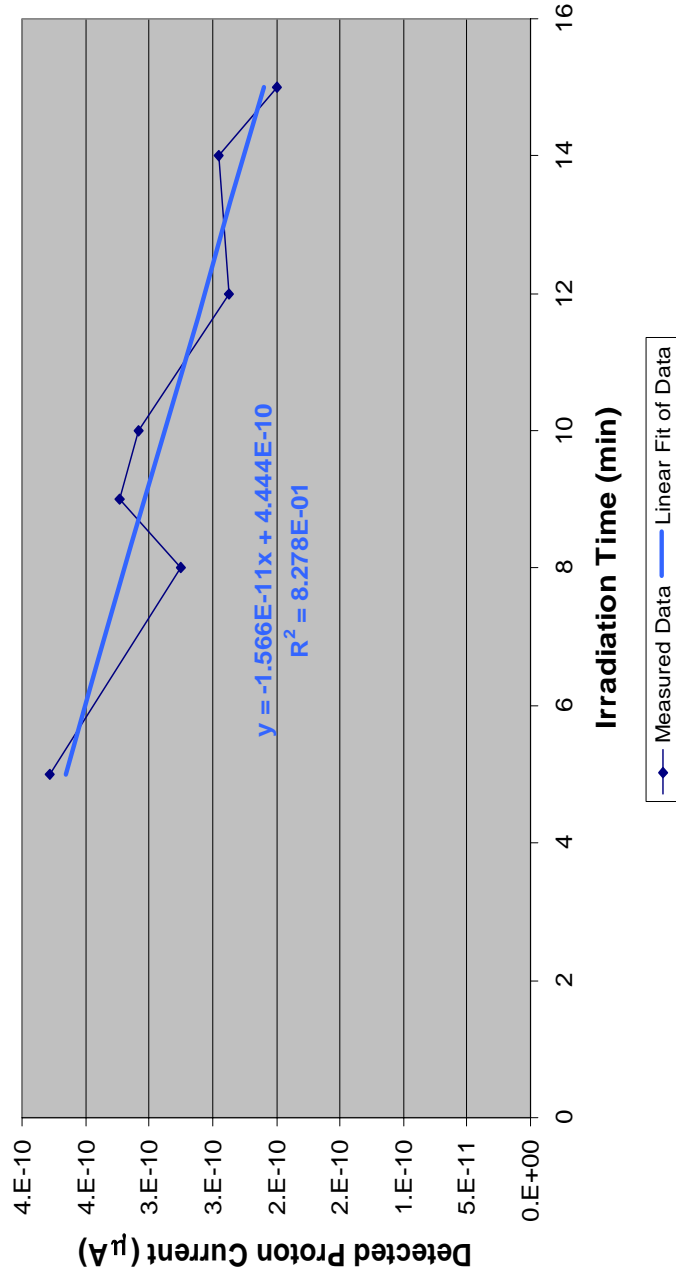


Figure 6.7 – Proton current during the relevant portion of the February 21st production run (IEC run 796). The IEC was operational from approximately 2 to 3 minutes into this run, but the quantity of ¹³N produced in that short period represents less than 3% of the total produced. Therefore, that current is neglected in the yield calculations.

T	I (uA)	P (nCi)	EOB A (nCi)
2.0	1.028E-06	0.632	0.157
5.0	1.497E-06	0.921	0.459
5.5	1.465E-06	0.901	0.286
6.0	1.433E-06	0.882	0.290
6.5	1.401E-06	0.862	0.293
7.0	1.369E-06	0.842	0.297
7.5	1.337E-06	0.823	0.300
8.0	1.305E-06	0.803	0.303
8.5	1.273E-06	0.783	0.306
9.0	1.241E-06	0.763	0.309
9.5	1.209E-06	0.744	0.312
10.0	1.177E-06	0.724	0.314
10.5	1.145E-06	0.704	0.317
11.0	1.113E-06	0.685	0.319
11.5	1.081E-06	0.665	0.320
12.0	1.049E-06	0.645	0.322
14.0	9.207E-07	0.566	0.325
14.5	8.887E-07	0.547	0.325
15.0	8.567E-07	0.527	0.324

Calculated Activity at EOB (nCi) 5.720

$$(5.720 \text{ nCi})(0.0236) = 0.135 \text{ nCi}$$

Table 6.7 - Table used to calculate the proton current required to produce an amount of ^{13}N equivalent to the quantity estimated at the end of bombardment (EOB) for the production run conducted February 21st. The proton current is defined using the fit equation in figure 6.8. Using the values for the time-dependent flux in the table above, the potential ^{13}N activity is calculated to be 5.720 nCi. This value is multiplied by the 0.0236 system efficiency to yield a calculated ^{13}N activity of 0.135 nCi, which is the same as the estimated activity at EOB from the measured results in figure 6.6. This proton current is then used to calculate the associated calibration factor (table 6.8). The first row of data is not used in this calculation.

Time	Measured protons/min	Predicted p/s*	Current (uA)
2	121338	8.27E+06	1.323E-06
5	141920	9.67E+06	1.547E-06
8	103132	7.03E+06	1.124E-06
9	121174	8.26E+06	1.321E-06
10	115589	7.88E+06	1.260E-06
12	89156	6.07E+06	9.719E-07
14	91994	6.27E+06	1.003E-06
15	74802	5.10E+06	8.154E-07

***Calibration Factor = 4088**

Table 6.8 – Table used to calculate the calibration factor required in order to relate the detected proton current to the total proton current inside the IEC chamber for the February 21st, 2003 run. This is done in the same manner as described in table 6.5. The first row of data is not used in this calculation.

Total Proton Current Required Inside the IEC to Produce the Activity of ¹³N Measured from February 21st Production Run

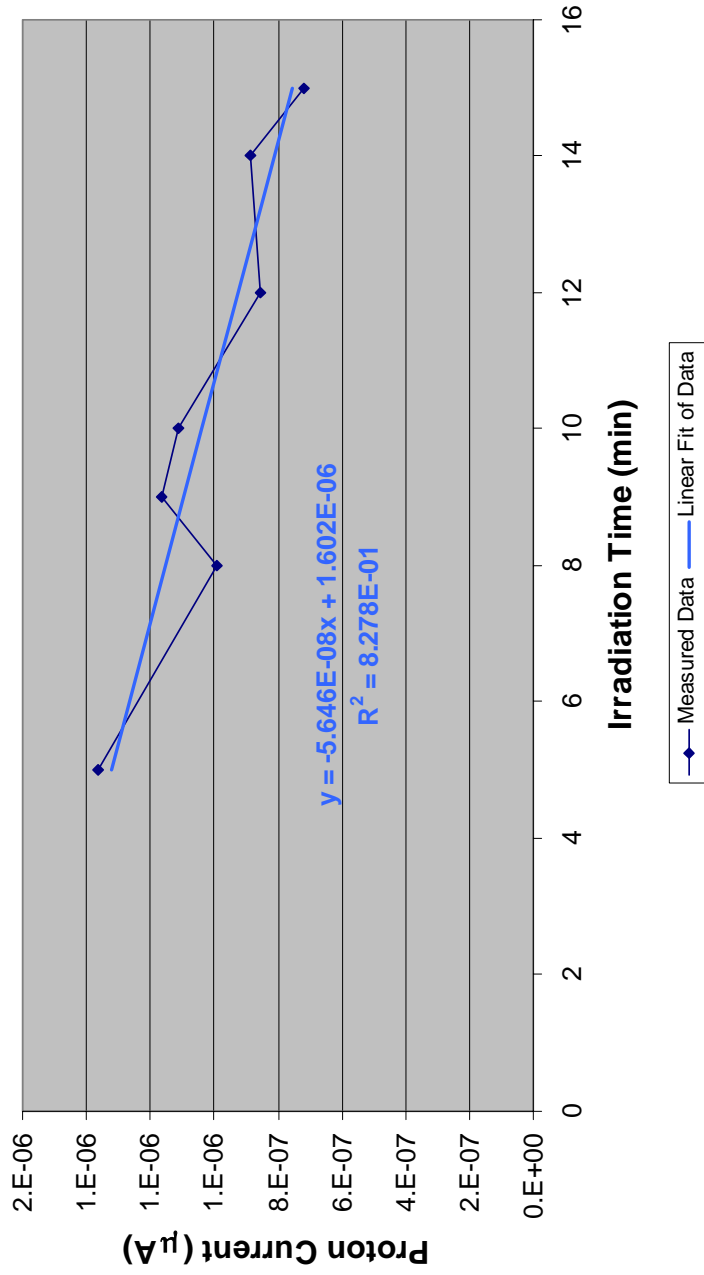


Figure 6.8 – Plot of total proton current necessary inside the IEC to produce the activity of ¹³N at the end of bombardment (EOB) as estimated from figure 6.6 using the calibration factor of 4,088 from table 6.8. The time-dependent proton current is given by the fit equation in the chart above.

Chapter 7 Discussion of Results

Section 7.1 Certainty of Experimental Results

The true importance of the experimental results is whether or not they demonstrate with reasonable statistical certainty that this experiment created ^{13}N . If so, then the experimental goal stated at the beginning of Chapter 1 was achieved. To determine this, the error associated with each data point in figures 6.4 and 6.6 is examined. The February 19th production run is investigated first.

As shown in table 7.1, the net number of counts detected during each of the five 180-second count intervals from the February 19th run varies from 179 counts in the first interval to 86 counts in the fifth interval. Since radioactive decay events follow a Poisson distribution, the measurement uncertainty in the total net counts is calculated by summing the uncertainty in the gross number of counts and the uncertainty in the background counts (from table 6.2) in quadrature [7]. The statistical certainty is one minus the ratio of the uncertainty in a count interval to the total net counts in that interval (see equation (5.1)). It is a measure of the probability that the actual total net activity of the sample lies within the range of the total net counts plus or minus the measurement uncertainty.

The statistical certainties from the February 19th production run range from 89.6% to 81.4%, with an average value of 86.0%. Hence, on average there is a 86% probability that the true activity of the radioisotope measured in the ion resin lies within the error bars of figure 6.4. Moreover, the theoretical decay curve shown in figure 6.4 passes through the error bars of each data point. Combining these two facts creates very compelling evidence that this experiment produced ^{13}N .

Count Interval	Total Net Counts	Measurement Uncertainty	Statistical Certainty (%)
1	179	18.68	89.6
2	149	17.86	88.0
3	131	17.35	86.8
4	105	16.58	84.2
5	86	16.00	81.4

Table 7.1 – Summary of net counting data from the February 19th production run. The average statistical certainty is 86.0% for all count intervals.

The statistical certainty of the February 21st production run is examined using the net counting data for this run (see table 7.2). Note that even though the total number of net counts in each count interval is roughly half that detected in the first production run, the statistical certainties differ by only 11%. This is because the statistical certainty is a function of the uncertainty, which is inversely proportional to the square root of the total net counts. Therefore, large differences in the total net counts create only small changes in the statistical certainty of the results. The average statistical certainty of the five counting results is 75.1%. Furthermore, a fit of the count data in figure 6.6 produced a decay constant only 1.3% different from the true ^{13}N decay constant. These facts clearly demonstrate that this experiment created ^{13}N .

Count Interval	Total Net Counts	Measurement Uncertainty	Statistical Certainty (%)
1	106	17.15	83.8
2	78	16.31	79.1
3	72	16.12	77.6
4	52	15.49	70.2
5	43	15.20	64.7

Table 7.2 – Summary of net counting data from the February 21st production run. The average statistical certainty is 75.1% for all count intervals.

Section 7.2 Calibration Factors

As discussed in Chapter 6, the activity of ^{13}N produced in these two experiments enabled the calculation of calibration factors that relate the detected D- ^3He proton current to the total D- ^3He proton current required inside the IEC to produce the two activities of ^{13}N measured. These values were calculated to be 2,804 and 4,088 for the February 19th and 21st production runs, respectively. The results of the two production experiments are deemed equally credible, so the overall calibration factor for ^{13}N production in the UW IEC is found from the average of these two values. Therefore, the total proton current inside the UW IEC is found to be a factor of 3,446 larger than the proton current measured by the proton detector.

It is instructive to put this calibration factor into perspective. Consider the 1,200 mm² (12cm²) surface area of the proton detector, which is located 81 cm from the center of the cathode. The surface area of a sphere with a radius of 81 cm has a surface area of 82,448 cm². These two surface areas differ by a factor of 6,871. If all D- ^3He protons were emitted from a perfect point source in the center of the cathode and could travel isotropically 81 cm unimpeded, the proton detector would only see $\frac{1}{6,871}$ of the number of protons crossing the surface area of the sphere. The 6,871 calibration factor for this ideal case is a factor of two larger than the 3,446 calibration factor determined above from the two ^{13}N production experiments. In reality, however, the D- ^3He protons are not emitted from an ideal point source in the center of the cathode. A majority of the reactions likely occur on the surface of the cathode wires [25]; some likely occur as a result of converged core reactions at the center of the cathode; and some reactions may even be the result of a volume source

stemming from charge-exchange reactions. Considering this variation in the source of protons, the 3,446 calibration factor is a reasonable value.

Section 7.3 Potential sources of Uncertainty

Throughout this experiment, several assumptions were made to simplify measurements and calculations. Although it's felt that these assumptions have only a very minor effect on the resulting calculations and measurements, it's important to note them here for completeness. The assumptions affect two general aspects of this experiment: the development of the theory predicting the activity of ^{13}N created (Chapter 4), and the measurement of the ^{13}N activity in the resin column.

The following assumptions were made in developing the theoretical yield equations and the system efficiencies discussed in Chapter 4. First, it was assumed that the $\text{D-}^3\text{He}$ protons emanate from an ideal point source located in the center of the cathode. Recent indications are that most of the $\text{D-}^3\text{He}$ protons originate from the surface of the cathode wires [25], which span a diameter of 10 cm. Additionally, the distribution of these embedded $\text{D-}^3\text{He}$ reactions across the length and circumference of the cathode wires is unknown, but it is unlikely that they are uniformly distributed.

Secondly, the thickness of the stainless steel tubing is assumed to be a constant 0.013 cm. Obviously, this thickness varies within a tube and from tube to tube. The manufacturer was unable to provide an accurate estimate of the deviation in wall thickness, but estimated it to be 10%. Third, to determine the saturated yield the average energy lost by a proton passing through the tube wall was calculated using an average wall thickness. A more precise method to determine the saturated yield would be to divide the range of wall

thicknesses into bins and perform a weighted, numeric calculation to determine the resulting spectrum of proton energies.

Fourth, no attempt was made to account for the effect of charge exchange reactions. Charge exchange reactions enable fast, neutral atoms to undergo fusion reactions at locations other than the cathode. Rather than having a proton current emanating from a point source as assumed, the fast neutrals can create fusion reactions (and therefore proton currents) in the volume of the chamber outside the cathode. It's not clear what fraction of the total D-³He fusion reactions are caused by these fast neutral atoms, but it's thought to be on the order of only a few percent.

Some assumptions were also made in the measurement techniques used to count the resin column. First, the very small quantity of ¹³N captured by the resin column is assumed to be located at roughly a point source near the upstream end of the column. This leads to the second assumption, which is the detector's efficiency in detecting the 511 keV gamma rays from the ¹³N in the resin column is assumed to be the same as its efficiency in detecting the 511 gamma rays from the small, thin, calibrated ²²Na source. Third, it's assumed that ¹³N is the only positron-emitting radionuclide produced in this experiment so that the decay curve should only reflect the decay of ¹³N.

In summary, the results of this experiment demonstrate with a high degree of statistical certainty that a proton current from the inertial electrostatic confinement fusion of D-³He can repeatedly produce ¹³N. Moreover, the activities of ¹³N produced in these experiments enabled the detected proton current to be related to the total proton current inside the UW IEC by a factor of 3,446.

Chapter 8 Conclusions

The results of this proof-of-principle experiment lead to the development of the following four major conclusions:

1) First and foremost, this experiment demonstrates that the 14.7 MeV protons from D-³He fusion reactions in an IEC device can successfully and reproducibly create ¹³N.

2) Second, D-³He fusion protons from IEC fusion could create a number of short-lived PET radioisotopes.

3) Thin-walled stainless steel tubes soldered to stainless steel manifolds can be used to create an effective and durable water containment apparatus. Aluminum tubes do not work well in the IEC plasma environment since electron jets easily damage them and the joints between the tubes and manifolds could not be soldered or sealed with epoxy.

4) This experiment demonstrated that the ion exchange resin column was a simple and efficient method to capture the ¹³N in a volume small enough for effective detection.

5) Although the quantity of ¹³N produced in these experiments was small, this work represents the first known demonstration of fusion technology for a commercial purpose.

Chapter 9 Suggestions for Future Work

Although the quantity of ^{13}N produced was not important for this proof-of-principle experiment, the goals of future work in this area will surely include producing larger activities of ^{13}N . Larger quantities will provide longer counting times, more accurate decay curves, and better counting statistics. Increased yields will also increase the relevance of this work. Several improvements can be made to increase the ^{13}N yield of this experiment.

First, the $\text{D-}^3\text{He}$ reaction rate should be increased. The ^{13}N yield is directly proportional to the proton current incident upon the target. Increasing the reaction rate by a factor of 1,000 should increase the ^{13}N yield by a factor of 1,000. Currently, the UW IEC experimental team is developing methods to improve the IEC reaction rate using ions guns. By using ion guns to inject a current of ^3He ions into the cathode, the amount of $^3\text{He}^+$ should be increased. In addition, most of the background gas can be eliminated because the source of $^3\text{He}^+$ is external to the chamber. This will increase the mean free path of the ions and enable them to attain higher energies within the cathode. Additionally, the research team is investigating methods to doubly ionize the ^3He , which will double its energy. The net result should be an increase in reaction rates by a factor of 100 or more.

Second, the ^{13}N yield can be increased by a factor of 15 or more by simply improving the design of the water containment apparatus. If a spherical apparatus were placed outside the cathode, the protons would strike the walls of the apparatus orthogonally (assuming a point source of protons located in the center of the chamber). This would eliminate the system efficiency caused by the round tube geometry. If this apparatus intercepted 90% of the $\text{D-}^3\text{He}$ protons produced, the efficiency of the isotope production

system defined in Chapter 4 would increase from 0.0236 to 0.3727 – nearly a factor of 16 greater.

Third, the proton current must remain constant throughout an isotope production run. During the two production runs conducted in this experiment, the D-³He reaction rate decrease in a linear fashion after only a few minutes IEC operation. The proton currents at the end of the production runs were less than half of their initial value. It's believed the stalk caused this phenomenon to occur. Therefore, improvements must be made to the stalk and, if necessary, the cathode to ensure the IEC can maintain a constant fusion reaction rate for 15 minutes or more.

Fourth, better detection systems should be used to count the 511 keV gamma ray activity of the resin column. Although much less efficient, a coincidence detection system can reduce the background activity by a factor of several hundred. This might allow small-activity samples to be counted for longer periods of time. Additionally, well counters should be used in order to vastly improve the detection efficiency.

Finally, a ¹³C target could be used to create ¹³N from (p,n) reactions. Although very expensive (currently ~\$250/g), the saturated yield from ¹³C is approximately seven times larger than the saturated yield of water. A ¹³C target also poses the additional problem of ¹³N extraction, but Dr. Andy Roberts of the University of Wisconsin Department of Medical Physics has developed techniques to sweep solid carbon targets with hydrogen gas in order to produce ¹³N-ammonia. The efficiency of this process is thought to be about 20% and new methods are being investigated that should further increase this.

References

- [1] IAEA, Charged-particle Cross Section Database for Medical Radioisotope Production [Electronic version]. IAEA-TECDOC-1211 (May 2001).
- [2] R.J. Nickles, "The Production of a Broader Palette of PET Tracers," *Journal of Labelled Compounds and Radiopharmaceuticals* **45**, 1 (2002).
- [3] Centers for Medicare and Medicaid Services, Department of Health and Human Services, (August 16th, 2003), Retrieved April 29, 2003 from Centers for Medicare and Medicaid Web site: <http://www.cms.hhs.gov/ncdr/memo.asp?id=66>
- [4] K. Becker, Photographic Film Dosimetry: Principles and Methods of Quantitative Measurement of Radiation by Photographic Means, pp. 13-15, *Focal P.*, London, (1966).
- [5] J.A. Sorenson and M.E. Phelps, Physics in Nuclear Medicine, 2nd ed., pp. 434-451, *W.B. Saunders Company*, Philadelphia, (1987).
- [6] R.D. Evans, The Atomic Nucleus, pp. 629-630, *McGraw-Hill*, New York, (1955).
- [7] C. Knoll, Radiation Detection and Measurement, 3rd ed., pp. 65-97, 335-341, 668-680, *John Wiley & Sons, Inc.*, New York, (2000).
- [8] N. Tamaki, et al., "Dynamic Positron Computed Tomography of the Heart with a High Sensitivity Positron Camera and Nitrogen-13 Ammonia," *Journal of Nuclear Medicine* **26**, 567 (1985).
- [9] P.V. Harper, et al., "Clinical Feasibility of Myocardial Imaging with ¹³NH₃," *Journal of Nuclear Medicine* **13**, 278 (1972).
- [10] W.G. Kuhle, et al., "Quantification of Regional Myocardial Blood Flow Using ¹³N Ammonia and Reoriented Dynamic Positron Emission Tomographic Imaging," *Circulation* **86**, 1004 (1992).
- [11] O. Muzik, et al., "Validation of Nitrogen-13-ammonia Tracer Kinetic Model for Quantification of Myocardial Blood Flow Using PET," *Journal of Nuclear Medicine*, **34**, 83 (1993).
- [12] G.H. Miley, et al., "Inertial –Electrostatic Confinement: An Approach to Burning Advanced Fuels," *Fusion Technology* **19**, 840 (1991)
- [13] P.T. Farnsworth, "Method and Apparatus for Producing Nuclear-Fusion Reactions," U.S. Patent #3,386,883 (1968)

- [14] R.L. Hirsch, "Inertial-Electrostatic Confinement of Ionized Fuions Gases," *Journal of Applied Physics* **38**, 4522 (1967).
- [15] R.W. Bussard, "Some Phycs Considerations of Magnetic Inertial-Electrostatic Confinement: A New Concept for Spherical Converging-Flow Fusion," *Fusion Technology* **19**, 273 (1991)
- [16] G.L. Kulcinski, "The United States IEC Program," *Fifth U.S.-Japan Workshop on Inertial Electrostatic Confinement Fusion*, University of Wisconsin – Madison, October 9-10, 2002.
- [17] L.J. Wittenberg, J.F. Santarius, and G.L. Kulcinski, "Lunar Sources of ^3He for Commercial Fusion Power," *Fusion Technology* **10** 2, 167 (1986).
- [18] K.R. Harris-Kuhlman, "Trapping and Diffusion of Helium in Lunar Materials," Ph.D. Thesis, University of Wisconsin – Madison, (1998).
- [19] G.L. Kulcinski, "Near Term Commercial Opportunities from Long Range Fusion Research," *Fusion Technology* **30**, 411 (1996).
- [20] G.L. Kulcinski, and H.H. Schmitt, "Fusion Power from Lunar Resources," *Fusion Technology* **21**, 2221 (1992).
- [21] G.L. Kulcinski and J.F. Santarius, "New Opportunities for Fusion in the 21st Century – Advanced Fuels," *Fusion Technology* **39**, 480 (2001).
- [22] G.L. Kulcinski, "Non-Electric Applications of Fusion Energy – An Important Precursor to Commercial Electric Power," *Fusion Technology* **34**, 477 (1998).
- [23] G.L. Kulcinski, I.N. Sviatoslavsky, G.A. Emmert, H.M. Attaya, J.F. Santarius, M.E. Sawan, and Z. Musicki, "The commercial Potential of D- He^3 Fusion Reactors," *12th Symposium on Fusion Engineering*, Monterey, CA, IEEE Cat. No. 87CH2507-2, **Vol. 1**, p. 772 (1987).
- [24] R.P. Ashley, G.L. Kulcinski, J.F. Santarius, S. Krupakar Murali, G. Piefer, and R. Radel, "Steady-State D- ^3He Proton Production in an IEC Fusion Device," *Fusion Technology* **39**, (2001).
- [25] B.B. Cipiti, and G.L. Kulcinski, "Embedded D- ^3He Fusion Reactions and Medical isotope production in an Intertial Electrostatic Confinement Device," *15th Topical Meeting of Fusion Energy*, American Nuclear Society, Washington, D.C., November 17-21, 2002.

- [26] K. Dorfner, Editor, Ion Exchangers, pp. 14-112, *Walter de Gruyter & Co.*, Berlin, (1990).
- [27] National Institute of Standards and Technologies PSTAR program, <http://physics.nist.gov/PhysRefData/Star/Text/PSTAR.html>, February, 2002.
- [28] H.Y. Khater, "Activation and Safety Analysis for Advanced Fuel Fusion Reactors," Ph.D. Thesis, *University of Wisconsin – Madison*, (1990).
- [29] N.N. Krasnov, "Thick Target Yield," *International Journal of Applied Radiation and Isotopes* **25**, 223 (1974).
- [30] K. Svoboda, "Terms Used in the Production of Radioisotopes by Charged-Particle Bombardment," *The Use of Cyclotrons in Chemistry, Metallurgy and Biology*, p. 383, Butterworths, London (1970).
- [31] J. Lange and H. Munzel, "Estimation of Unknown Excitation Functions for (xn), (pxn), (d,xn) and (p,xn) Reactions," *Kernforschungszentrum Karlsruhe*, **KFK-767** (May, 1968).
- [32] N.N. Krasnov, "Physical Principles of Activation Analysis with Charged Particles," *Atomnaya Energiya* **26**, 3 (1969).
- [33] K.A. Keller, J. Lange and H. Munzel, "Numerical Data and Functional Relationships in Science and Technology," *Landolt-Bornstein, New Series*, **Vol I/5C**, Springer (1974).
- [34] J. Stewart, Calculus: Early Transcendentals, 3rd ed., pp. 340-341, Brooks/Cole, Pacific Grove, CA., (1995).
- [35] F.H. Attix, Introduction to Radiological Physics and Radiation Dosimetry, pp. 560, John Wiley and Sons, New York, (1986).

Appendix A Raw Count Data from February 19th, 2003 Isotope Production Run

Raw 511 keV gamma ray measurements of resin column from first 180-second count. Although the MCA capable of detecting events up to energies of 5 MeV, no significant number of counts were detected above 1 MeV during these measurement.

Energy (keV)	Raw Counts in 180 s	Energy (keV)	Raw Counts in 180 s	Energy (keV)	Raw Counts in 180 s
0.0	46	327.3	11	663.8	7
0.9	40	337.5	12	674.0	4
11.1	40	347.7	16	684.2	3
21.3	46	357.9	8	694.4	7
31.5	60	368.1	14	704.6	5
41.7	60	378.3	18	714.8	6
51.9	60	388.5	15	725.0	8
62.1	45	398.7	8	735.2	2
72.3	29	408.9	8	745.4	7
82.5	23	419.1	11	755.6	5
92.7	19	429.3	12	765.8	1
102.9	25	439.5	12	776.0	7
113.1	12	449.7	13	786.2	6
123.3	23	459.9	20	796.4	7
133.5	31	470.1	23	806.6	2
143.7	27	480.2	22	816.8	6
153.9	27	490.4	36	827.0	7
164.1	29	500.6	38	837.2	7
174.3	22	510.8	40	847.4	6
184.5	26	521.0	26	857.6	4
194.7	24	531.2	21	867.8	3
204.9	23	541.4	18	878.0	3
215.1	24	551.6	12	888.2	5
225.3	16	561.8	8	898.4	6
235.5	23	572.0	5	908.6	0
245.7	12	582.2	12	918.8	5
255.9	13	592.4	5	929.0	8
266.1	15	602.6	15	939.2	1
276.3	11	612.8	7	949.4	4
286.5	23	623.0	2	959.6	4
296.7	16	633.2	4	969.8	4
306.9	10	643.4	5	980.0	5
317.1	11	653.6	8	990.2	4

Raw count data from second 180-second count.

Energy (keV)	Raw Counts in 180 s	Energy (keV)	Raw Counts in 180 s	Energy (keV)	Raw Counts in 180 s
0.0	46	327.3	14	663.8	7
0.9	36	337.5	13	674.0	7
11.1	42	347.7	11	684.2	12
21.3	45	357.9	12	694.4	6
31.5	52	368.1	9	704.6	6
41.7	57	378.3	19	714.8	9
51.9	51	388.5	12	725.0	5
62.1	46	398.7	12	735.2	7
72.3	32	408.9	10	745.4	2
82.5	19	419.1	15	755.6	12
92.7	15	429.3	8	765.8	8
102.9	13	439.5	14	776.0	6
113.1	12	449.7	14	786.2	4
123.3	20	459.9	19	796.4	3
133.5	22	470.1	22	806.6	5
143.7	27	480.2	21	816.8	4
153.9	21	490.4	33	827.0	4
164.1	18	500.6	35	837.2	5
174.3	20	510.8	33	847.4	3
184.5	18	521.0	26	857.6	6
194.7	20	531.2	21	867.8	3
204.9	20	541.4	12	878.0	3
215.1	28	551.6	6	888.2	5
225.3	18	561.8	6	898.4	5
235.5	22	572.0	13	908.6	6
245.7	18	582.2	10	918.8	7
255.9	15	592.4	4	929.0	2
266.1	23	602.6	10	939.2	4
276.3	25	612.8	9	949.4	2
286.5	10	623.0	11	959.6	5
296.7	14	633.2	10	969.8	6
306.9	12	643.4	9	980.0	5
317.1	13	653.6	3	990.2	3

Raw count data from third 180-second count.

Energy (keV)	Raw Counts in 180 s	Energy (keV)	Raw Counts in 180 s	Energy (keV)	Raw Counts in 180 s
0.0	45	327.3	11	663.8	3
0.9	48	337.5	11	674.0	1
11.1	58	347.7	22	684.2	7
21.3	44	357.9	16	694.4	4
31.5	51	368.1	12	704.6	6
41.7	49	378.3	11	714.8	2
51.9	52	388.5	13	725.0	5
62.1	41	398.7	18	735.2	1
72.3	33	408.9	17	745.4	6
82.5	21	419.1	11	755.6	2
92.7	22	429.3	9	765.8	5
102.9	20	439.5	9	776.0	1
113.1	17	449.7	10	786.2	6
123.3	17	459.9	23	796.4	6
133.5	24	470.1	18	806.6	7
143.7	23	480.2	15	816.8	8
153.9	22	490.4	31	827.0	3
164.1	12	500.6	23	837.2	4
174.3	21	510.8	26	847.4	3
184.5	19	521.0	29	857.6	6
194.7	17	531.2	12	867.8	4
204.9	21	541.4	15	878.0	4
215.1	17	551.6	11	888.2	1
225.3	17	561.8	13	898.4	4
235.5	20	572.0	8	908.6	8
245.7	13	582.2	11	918.8	5
255.9	23	592.4	5	929.0	10
266.1	25	602.6	3	939.2	5
276.3	15	612.8	9	949.4	4
286.5	15	623.0	9	959.6	6
296.7	16	633.2	3	969.8	4
306.9	10	643.4	13	980.0	5
317.1	16	653.6	7	990.2	4

Raw count data from fourth 180-second count.

Energy (keV)	Raw Counts in 180 s	Energy (keV)	Raw Counts in 180 s	Energy (keV)	Raw Counts in 180 s
0.0	45	327.3	13	663.8	6
0.9	36	337.5	17	674.0	7
11.1	45	347.7	14	684.2	7
21.3	55	357.9	11	694.4	4
31.5	59	368.1	10	704.6	4
41.7	45	378.3	12	714.8	4
51.9	56	388.5	14	725.0	5
62.1	30	398.7	11	735.2	6
72.3	23	408.9	13	745.4	3
82.5	23	419.1	15	755.6	3
92.7	18	429.3	14	765.8	5
102.9	17	439.5	7	776.0	3
113.1	16	449.7	10	786.2	5
123.3	20	459.9	14	796.4	5
133.5	22	470.1	17	806.6	4
143.7	24	480.2	19	816.8	5
153.9	29	490.4	24	827.0	10
164.1	25	500.6	24	837.2	2
174.3	23	510.8	30	847.4	5
184.5	25	521.0	17	857.6	5
194.7	21	531.2	18	867.8	3
204.9	16	541.4	10	878.0	8
215.1	19	551.6	9	888.2	4
225.3	15	561.8	8	898.4	5
235.5	19	572.0	5	908.6	4
245.7	18	582.2	8	918.8	4
255.9	14	592.4	9	929.0	6
266.1	20	602.6	9	939.2	7
276.3	18	612.8	9	949.4	1
286.5	16	623.0	8	959.6	2
296.7	9	633.2	5	969.8	4
306.9	20	643.4	5	980.0	1
317.1	11	653.6	7	990.2	3

Raw count data from fifth 180-second count.

Energy (keV)	Raw Counts in 180 s	Energy (keV)	Raw Counts in 180 s	Energy (keV)	Raw Counts in 180 s
0.0	30	327.3	18	663.8	4
0.9	46	337.5	10	674.0	3
11.1	45	347.7	19	684.2	7
21.3	48	357.9	16	694.4	2
31.5	52	368.1	11	704.6	5
41.7	48	378.3	11	714.8	6
51.9	52	388.5	13	725.0	3
62.1	38	398.7	9	735.2	6
72.3	20	408.9	9	745.4	5
82.5	21	419.1	19	755.6	4
92.7	18	429.3	7	765.8	8
102.9	20	439.5	12	776.0	4
113.1	19	449.7	18	786.2	3
123.3	21	459.9	17	796.4	6
133.5	19	470.1	16	806.6	4
143.7	20	480.2	13	816.8	4
153.9	27	490.4	13	827.0	5
164.1	29	500.6	30	837.2	4
174.3	24	510.8	20	847.4	2
184.5	19	521.0	15	857.6	4
194.7	22	531.2	17	867.8	3
204.9	12	541.4	5	878.0	3
215.1	19	551.6	16	888.2	6
225.3	24	561.8	9	898.4	4
235.5	14	572.0	13	908.6	4
245.7	21	582.2	3	918.8	2
255.9	11	592.4	8	929.0	5
266.1	11	602.6	11	939.2	2
276.3	11	612.8	9	949.4	5
286.5	11	623.0	8	959.6	7
296.7	13	633.2	4	969.8	3
306.9	8	643.4	8	980.0	5
317.1	15	653.6	8	990.2	9

Appendix B Raw Count Data from February 21st, 2003 Isotope Production Run

Raw 511 keV gamma ray measurements of resin column from first 180-second count. Although the MCA capable of detecting events up to energies of 5 MeV, no significant number of counts were detected above 1 MeV during these measurement.

Energy (keV)	Raw Counts in 180 s	Energy (keV)	Raw Counts in 180 s	Energy (keV)	Raw Counts in 180 s
0.0	44	327.3	6	663.8	3
0.9	42	337.5	14	674.0	3
11.1	44	347.7	6	684.2	3
21.3	60	357.9	14	694.4	7
31.5	61	368.1	14	704.6	7
41.7	40	378.3	9	714.8	3
51.9	53	388.5	9	725.0	4
62.1	34	398.7	9	735.2	3
72.3	27	408.9	9	745.4	3
82.5	20	419.1	8	755.6	8
92.7	19	429.3	14	765.8	4
102.9	21	439.5	10	776.0	5
113.1	17	449.7	12	786.2	3
123.3	25	459.9	10	796.4	6
133.5	18	470.1	18	806.6	4
143.7	18	480.2	20	816.8	3
153.9	29	490.4	28	827.0	6
164.1	22	500.6	22	837.2	6
174.3	32	510.8	28	847.4	6
184.5	20	521.0	29	857.6	5
194.7	17	531.2	16	867.8	4
204.9	15	541.4	12	878.0	5
215.1	22	551.6	10	888.2	5
225.3	16	561.8	7	898.4	3
235.5	20	572.0	11	908.6	2
245.7	15	582.2	5	918.8	5
255.9	23	592.4	8	929.0	4
266.1	14	602.6	8	939.2	3
276.3	19	612.8	5	949.4	3
286.5	20	623.0	11	959.6	2
296.7	17	633.2	3	969.8	7
306.9	15	643.4	4	980.0	4
317.1	18	653.6	9	990.2	5

Raw count data from second 180-second count

Energy (keV)	Raw Counts in 180 s	Energy (keV)	Raw Counts in 180 s	Energy (keV)	Raw Counts in 180 s
0.0	40	327.3	15	663.8	10
0.9	35	337.5	15	674.0	7
11.1	39	347.7	14	684.2	7
21.3	38	357.9	12	694.4	4
31.5	48	368.1	12	704.6	7
41.7	54	378.3	8	714.8	5
51.9	37	388.5	8	725.0	6
62.1	38	398.7	11	735.2	5
72.3	21	408.9	12	745.4	2
82.5	16	419.1	11	755.6	10
92.7	14	429.3	14	765.8	5
102.9	21	439.5	8	776.0	8
113.1	18	449.7	6	786.2	3
123.3	18	459.9	14	796.4	5
133.5	14	470.1	17	806.6	6
143.7	14	480.2	24	816.8	5
153.9	19	490.4	26	827.0	4
164.1	14	500.6	17	837.2	7
174.3	14	510.8	20	847.4	6
184.5	16	521.0	23	857.6	4
194.7	18	531.2	13	867.8	2
204.9	22	541.4	7	878.0	3
215.1	24	551.6	6	888.2	8
225.3	14	561.8	5	898.4	5
235.5	18	572.0	9	908.6	7
245.7	7	582.2	4	918.8	6
255.9	11	592.4	11	929.0	6
266.1	13	602.6	9	939.2	7
276.3	16	612.8	7	949.4	5
286.5	18	623.0	12	959.6	1
296.7	10	633.2	6	969.8	3
306.9	12	643.4	7	980.0	2
317.1	14	653.6	12	990.2	0

Raw count data from third 180-second count

Energy (keV)	Raw Counts in 180 s	Energy (keV)	Raw Counts in 180 s	Energy (keV)	Raw Counts in 180 s
0.0	36	327.3	8	663.8	4
0.9	33	337.5	13	674.0	4
11.1	49	347.7	11	684.2	9
21.3	52	357.9	16	694.4	4
31.5	44	368.1	11	704.6	6
41.7	35	378.3	9	714.8	6
51.9	32	388.5	12	725.0	8
62.1	29	398.7	7	735.2	3
72.3	31	408.9	12	745.4	13
82.5	24	419.1	2	755.6	6
92.7	14	429.3	7	765.8	5
102.9	20	439.5	6	776.0	9
113.1	13	449.7	13	786.2	7
123.3	15	459.9	15	796.4	7
133.5	19	470.1	8	806.6	6
143.7	27	480.2	14	816.8	3
153.9	17	490.4	29	827.0	3
164.1	29	500.6	22	837.2	6
174.3	20	510.8	21	847.4	7
184.5	20	521.0	14	857.6	3
194.7	24	531.2	12	867.8	6
204.9	17	541.4	18	878.0	2
215.1	17	551.6	9	888.2	6
225.3	19	561.8	4	898.4	7
235.5	17	572.0	7	908.6	4
245.7	19	582.2	9	918.8	4
255.9	12	592.4	8	929.0	4
266.1	8	602.6	7	939.2	9
276.3	17	612.8	7	949.4	4
286.5	13	623.0	8	959.6	7
296.7	14	633.2	7	969.8	5
306.9	21	643.4	8	980.0	3
317.1	6	653.6	6	990.2	2

Raw count data from fourth 180-second count

Energy (keV)	Raw Counts in 180 s	Energy (keV)	Raw Counts in 180 s	Energy (keV)	Raw Counts in 180 s
0.0	41	327.3	13	663.8	4
0.9	45	337.5	11	674.0	5
11.1	44	347.7	11	684.2	9
21.3	53	357.9	10	694.4	6
31.5	49	368.1	18	704.6	4
41.7	54	378.3	10	714.8	4
51.9	29	388.5	7	725.0	7
62.1	28	398.7	14	735.2	10
72.3	15	408.9	9	745.4	2
82.5	20	419.1	12	755.6	9
92.7	19	429.3	13	765.8	5
102.9	19	439.5	10	776.0	4
113.1	19	449.7	12	786.2	4
123.3	5	459.9	16	796.4	3
133.5	21	470.1	7	806.6	2
143.7	21	480.2	14	816.8	3
153.9	18	490.4	14	827.0	2
164.1	24	500.6	16	837.2	0
174.3	22	510.8	25	847.4	7
184.5	19	521.0	13	857.6	5
194.7	14	531.2	13	867.8	7
204.9	16	541.4	10	878.0	3
215.1	12	551.6	8	888.2	5
225.3	20	561.8	10	898.4	3
235.5	15	572.0	9	908.6	7
245.7	16	582.2	7	918.8	1
255.9	15	592.4	4	929.0	6
266.1	14	602.6	9	939.2	3
276.3	13	612.8	8	949.4	4
286.5	14	623.0	8	959.6	3
296.7	14	633.2	5	969.8	4
306.9	20	643.4	3	980.0	8
317.1	12	653.6	6	990.2	3

Raw count data from fifth 180-second count

Energy (keV)	Raw Counts in 180 s	Energy (keV)	Raw Counts in 180 s	Energy (keV)	Raw Counts in 180 s
0.0	34	327.3	19	663.8	4
0.9	44	337.5	12	674.0	2
11.1	40	347.7	10	684.2	3
21.3	42	357.9	10	694.4	5
31.5	42	368.1	10	704.6	8
41.7	35	378.3	5	714.8	4
51.9	22	388.5	10	725.0	6
62.1	27	398.7	16	735.2	6
72.3	19	408.9	13	745.4	10
82.5	18	419.1	18	755.6	10
92.7	17	429.3	10	765.8	9
102.9	19	439.5	3	776.0	5
113.1	17	449.7	13	786.2	6
123.3	17	459.9	12	796.4	3
133.5	17	470.1	8	806.6	6
143.7	17	480.2	9	816.8	4
153.9	22	490.4	14	827.0	2
164.1	18	500.6	11	837.2	6
174.3	19	510.8	24	847.4	4
184.5	10	521.0	17	857.6	7
194.7	23	531.2	16	867.8	3
204.9	25	541.4	7	878.0	3
215.1	11	551.6	8	888.2	3
225.3	28	561.8	11	898.4	5
235.5	16	572.0	14	908.6	0
245.7	15	582.2	7	918.8	6
255.9	16	592.4	8	929.0	3
266.1	10	602.6	4	939.2	1
276.3	18	612.8	3	949.4	7
286.5	18	623.0	3	959.6	5
296.7	12	633.2	3	969.8	4
306.9	12	643.4	8	980.0	3
317.1	16	653.6	3	990.2	5